Lehrstuhl für Werkstoffkunde und Werkstoffmechanik mit
Materialprüfamt für den Maschinenbau
Technische Universität München

Numerical implementation of continuum dislocation-based plasticity

Cornelia Schwarz

Vollständiger Abdruck der von der Fakultät für Maschinenwesen
der Technischen Universität München
zur Erlangung des akademischen Grades eines

Doktor-Ingenieurs (Dr.-Ing.)

genehmigten Dissertation.

Vorsitzender:	Univ.-Prof. Dr.-Ing. Bernd-Robert Höhn
Prüfer der Dissertation:	
	1. Univ.-Prof. Dr. mont. habil. Ewald Werner
	2. Univ.-Prof. Dr.-Ing. Wolfgang A. Wall

Die Dissertation wurde am 24. April 2007 bei der Technischen Universität München
eingereicht und durch die Fakultät für Maschinenwesen
am 16. Juli 2007 angenommen.

Acknowledgements

The studies being basis for this thesis have been conducted in the years 2003-2007 at the Lehrstuhl für Werkstoffkunde und Werkstoffmechanik, TU München, in the context of the research projects We2351/8-1 and We2351/8-3, funded by the DFG (Deutsche Forschungsgemeinschaft).

I would like to express my gratitude to my advisor PD Dr.-Ing. habil. R. Sedláček who was a patient teacher and discussion partner, and who never lost trust in my work, even in times where no idea seemed to bring us forward. Thank you also to our cooperation partners: Prof. J. Kratochvíl for his inspiring discussions, Prof. B. Devincre and Dr. Arjen Roos for their commitment concerning the coupling of our model with ZeBuLoN and their helpful comments to the relevant parts of this thesis. My special thank is due to Prof. Dr. mont. E.A. Werner for his continuous support, fruitful discussions and his contractible enthusiasm. Thanks also to my colleagues for the pleasant atmosphere at the institute.

My last and very special thankyou applies to my beloved companion Matthias, who endowed me immeasurable energy and support during the last years.

Garching, April 2007 Cornelia Schwarz

Kurzfassung

Die fortwährende Tendenz hin zu immer kleiner werdenden Strukturen, beispielsweise in der Mikroelektronik oder in der Entwicklung miniaturisierter Bauteile, stellt neue Herausforderungen an die Modellbildung zur Beschreibung der Plastizität. In unterschiedlichsten Versuchen wurde gezeigt, dass Strukturen auf der μm-Skala ein Verformungsverhalten aufweisen, das sich grundlegend von dem massiver Strukturen unterscheidet.

Eine Erklärung für dieses Phänomen findet man wahrscheinlich in der Natur des wichtigsten der plastischen Verformung zugrunde liegenden Mechanismus, dem Gleiten von Versetzungen. Die Modellierung dieser längenskalen abhängigen Verformung kann allerdings auf ganz unterschiedlichen Skalen erfolgen, welche von der Beschreibung der ungeordneten Atomstruktur bis hin zu den Ansätzen basierend auf Gradienten der plastischen Dehnung reichen.

Das versetzungsbasierte Kontinuumsmodell, welches Thema dieser Arbeit ist, strebt eine deterministische, kontinuierliche Beschreibung der längenskalen abhängigen plastischen Verformung auf der Mesoskala an. Dabei sollen die physikalischen Vorgänge, welche die längenskalen Effekte hervorrufen, berücksichtigt werden. Dies wird in erster Linie durch die Einbeziehung der Eigenenergie der Versetzungen gewährleistet: Versetzungen, die in beschränkten, sich plastisch verformenden Kanälen gleiten, sind gezwungen sich auszubauchen, und tragen so aufgrund ihrer Linienspannung weniger stark zur plastischen Verformung bei. Das Modell beschreibt nicht das Gleiten einzelner Versetzungen, sondern einfachwertiger Versetzungsfelder. Lediglich eine geringe Anzahl von Feldvariablen, wie etwa die skalare Versetzungsdichte oder die Orientierung der Versetzungen, bilden die Basis des Modells. Über die Theorie der Kristallplastizität kann es die Rolle eines Konstitutivgesetzes in der Kontinuumsmechanik (kleiner Verformungen) einnehmen.

In den letzten Jahren wurde das versetzungsbasierte Kontinuumsmodell erfolgreich auf eine Reihe typischer Beispielprobleme längenskalen abhängiger plastischer Verformung angewandt, etwa die Biegung eines freien oder die einfache Scherung eines bzgl. der Versetzungsbewegung beschränkten dünnen kristallinen Streifens. Doch bis heute konnten nur solche Probleme behandelt werden, welche sich eindimensional formulieren lassen.

Diese Arbeit hat zwei Schwerpunkte: zum Einen, eine robuste Implementierung dieses Modells für zweidimensionale Probleme, welche sich im Rahmen des ebenen Verzerrungszustandes

beschreiben lassen, zu entwickeln, und zum Anderen eine weitere Quelle für Längenskaleneffekte in das Modell zu integrieren, die Rückspannung, welche die kurzreichweitigen Wechselwirkungen zwischen Versetzungen beschreibt.
Die Modellgleichungen bilden ein System partieller Differentialgleichungen vom Typ „konvektionsdominiertes Konvektions-Diffusions Problem“. Die numerische Umsetzung des gegenwärtigen Modells stellt daher eine große Herausforderung dar. Versucht man die numerische Lösung des Systems auf die herkömmliche Weise, das heißt basierend auf der Eulerschen Beschreibung und symmetrischen Diskretisierungsverfahren, so treten Stabilitätsprobleme auf, welche sich in stark oszillierenden Lösungskurven äußern. Daher wird eine spezielle Implementierung gewählt, welche auf einem einfachen, homogenen Finite Elemente Netz für den Teil der Kontinuumsmechanik sowie auf einem zweiten Gitter, das an die Lage diskreter Gleitebenen gebunden ist, basiert. Die Knoten des zweiten Gitters repräsentieren die Segmente einer stellvertretenden Versetzung der jeweiligen Gleitebene. Ihre zeitliche Entwicklung ist durch die Lagrangeschen Modellgleichungen bestimmt, was eine kontinuierliche Umverteilung der Segmente entsprechend ihrer natürlichen Gleitrichtung mit sich bringt.
Was den zweiten Schwerpunkt angeht, so schlagen wir einen funktionalen Ausdruck für die Rückspannung vor, welche sowohl zwischen Versetzungen ein und der selben wie auch zwischen Versetzungen auf benachbarten Gleitebenen wirkt. Sie stellt eine Verallgemeinerung der pile-up Spannung, welche oft mit dem Hall-Petch Effekt in Verbindung gebracht wird, dar. Im Gegensatz zu früheren Vorschlägen für ein solches Modell für die Rückspannung unterscheiden wir zwischen der Rückspannung, welche zwischen den parallelen Versetzungen eines einfachwertigen Feld wirkt, und der zwischen im Allgemeinen nicht parallelen Versetzungen aus verschiedenen Feldern. Dies wird realisiert indem die Größe der Rückspannung in Abhängigkeit von der relativen Orientierung der wechselwirkenden Versetzungen definiert wird.

Die Arbeit gliedert sich wie folgt. Im Anschluß an ein einleitendes Kapitel, welches einen Überblick über die Modellierung von Plastizität gibt, speziell der Plastizität auf der μm-Skala und damit der längenskalen äbhängigen Verformung, wird in Kapitel 2 das klassische versetzungsbasierte Kontinuumsmodell vorgestellt. Die numerische Umsetzung des Modells wird in Kapitel 3 behandelt. Die grundlegenden Betrachtungen zur Einführung der Rückspannung in Kapitel 4 werden in Kapitel 5 durch ein Anwendungsbeispiel des erweiterten Modells ergänzt. Der Anhang enthält eine Sammlung benutzter Symbole, eine Einführung in die gewählte mathematische Notation, eine Zusammenstellung benutzter mathematischer Zusammenhänge, sowie eine kurze Vorstellung der benutzen Software.

Abstract

The ongoing trend to smaller and smaller structures, for example in micro-electronics or in the engineering of miniaturised components, has posed new challenges to the field of plasticity modelling. In various experiments it has been shown, that structures on the μm-scale exhibit a deformation behaviour that is essentially different from that of bulk structures.

An explanation for this phenomenon probably has to be sought in the fundamentals of plastic deformation, that is the motion of dislocations. However, modelling of the size-dependent deformation can take place on very different length scales, ranging from the individual disordered atoms to the gradient of plastic strain approaches. The continuum dislocation-based model, which is the topic of this thesis, aims at a deterministic continuum description of the size-dependent plastic deformation at the mesoscale, considering the physical principles that give rise to size-effects. This is primarily realised by taking into account the dislocation self-force: dislocations that glide in confined plastic channels have to bow out and thus, due to their line tension, do less effectively transport the plastic deformation. The model does not describe the glide of individual dislocations, but the evolution of fields of dislocations. Only a small number of field variables, like the scalar dislocation density or the dislocation orientation, appear in the model. Via the principles of crystal plasticity the formulation takes over the role of a constitutive law in the framework of (small-strain) continuum mechanics.

In the last years, the continuum dislocation-based model has been successfully applied to a number of typical problems that exhibit size-dependent plastic deformation, like bending or constrained simple shear of a thin film. Up to now, only such problems that could be formulated in a one-dimensional framework could be treated.

The focus of this thesis is twofold. First, the development of a robust implementation of the model for two-dimensional plane strain problems is described. Then, the extension of the model by a second source of size-effects, namely the back stress, which describes the short-range interaction of dislocations, is introduced.

The numerical implementation of the present model poses a big challenge as it results in a system of partial differential equations of convection-diffusion type with dominant convection. Addressing the numerical solution of the problem in the common way, that is using the Eulerian description and symmetric discretisation schemes, yields severe stability problems, resulting in

oscillatory solution curves. Therefore a very special implementation was chosen, which is based on a simple homogeneous Finite Element discretisation for the small-strain continuum mechanics part and a second, slip plane based mesh. The nodes of the latter correspond to segments of representative dislocations residing in the respective slip planes. Their temporal development is defined by the Lagrangian model equations, yielding a continuous redistribution of the segments according to the direction of their 'flow'.

Concerning the second objective of the thesis, a continuum expression for the back stress that acts both between the dislocations on one slip plane and on neighboured slip planes is proposed. It is a generalisation of the pile-up stress which is often associated with the Hall-Petch effect. In contrast to earlier propositions for such a back stress model, we distinguish the back stress acting between the parallel dislocations of one and the same single-valued field and between dislocations belonging to different fields, being in general non-parallel. This is realised by defining the strength of the back stress dependent on the intersection angle of the interacting dislocations.

The thesis is organised as follows. After an introductory chapter, which gives a survey of the modelling of plasticity, especially plasticity on the microscale including size-dependent deformation, chapter 2 resumes the classical continuum dislocation-based model. The numerical implementation of the model is investigated in chapter 3. The theoretical considerations on the introduction of the back stress in chapter 4 are supplemented by an application of the enhanced model in chapter 5. In addition to a collection of the symbols used, the appendix contains the mathematical notation, and some useful mathematical relations. It also gives a short introduction to the used software.

Contents

Part I

The classical model

CHAPTER 1

Introduction

Understanding and describing the strength of crystalline solids has been a strong concern in the scientific community for about 80 years. In the beginning of this period, the large discrepancy between the measured strength of a crystalline material and the theoretically predicted strength posed a challenge to this field.
As a possible explanation, in 1934 for the first time the concept of a dislocation, that is a line defect within the crystal, was predicted based on theoretical considerations. The existence of dislocations was verified by Transmission Electron Microscope images around 1950. Nowadays it is beyond all question that dislocations carry the plastic deformation in crystalline solids[1]. Like pushing a pleat along a carpet alleviates its displacement, dislocations allow for easy slipping of crystal planes against each other.

1.1 The concept of dislocations

It is essential to understand how an arbitrary curve $\boldsymbol{\varphi}$ in the crystal becomes a dislocation, and how it is related to the plastic deformation of the solid. For simplicity, assume a closed loop described as a planar curve $\boldsymbol{\varphi}$, for technical details see section 2.1. Let the curve be part of a crystal, which is considered as elastic continuum. Let A be a surface in the crystal which is bordered by $\boldsymbol{\varphi}$. This may be the planar area enclosed by the loop, A_{L}, or any other surface. Let $\mathrm{d}\boldsymbol{a}$ be the normal to this surface, defined such that $\boldsymbol{\varphi}$ encircles it in the right-handed sense, figure 1.1. The curve $\boldsymbol{\varphi}$ becomes a dislocation line by the following procedure: suppose the material to be cut along A, and the face of the cut surface on the side of the negative normal $\mathrm{d}\boldsymbol{a}$ be displaced by $\boldsymbol{b}$ with respect to the face of the positive normal. To preserve the continuity of the crystal, material of volume $\boldsymbol{b} \cdot \mathrm{d}\boldsymbol{a} > 0$ must be removed above the cut surface, and material volume $\boldsymbol{b} \cdot \mathrm{d}\boldsymbol{a} < 0$ must be added below it. The cut can now be rejoined everywhere but along the

[1] Of course there are some more mechanisms allowing for the plastic deformation of crystalline solids, for example twinning or grain boundary sliding. But within this thesis, only plasticity induced by dislocation glide, which is still the most important mechanism, will be considered.

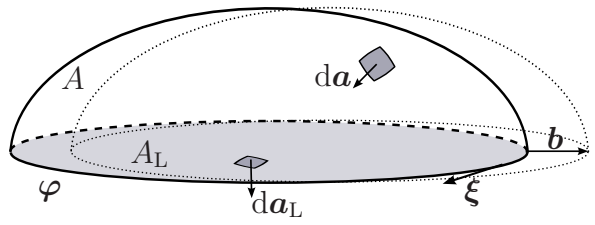

Figure 1.1: Creation of a dislocation loop φ enclosing the area A_{L}. The bordered surface A is displaced by the Burgers vector $\boldsymbol{b}$.

line φ. A dislocation with the Burgers vector $\boldsymbol{b}$ has been created. The small tube around it is called the dislocation core. At locations where the tangent to the dislocation line $\boldsymbol{\xi}$ is parallel to $\boldsymbol{b}$, the dislocation is of pure screw type, where both directions are perpendicular it is pure edge. In general, dislocations have a mixed edge-screw character, which goes along with their innately curved shape, see also the illustration in figure 1.2.

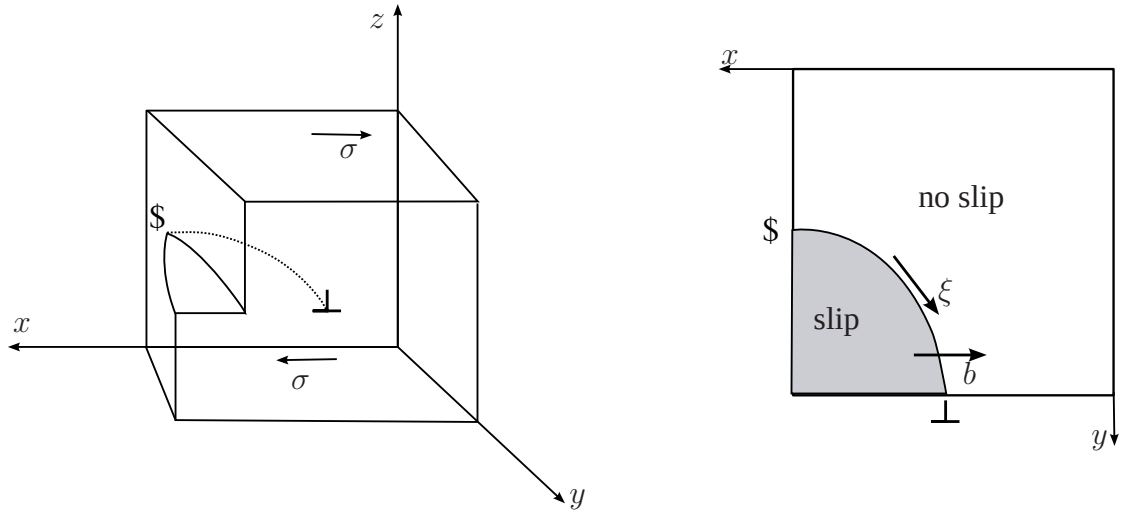

Figure 1.2: Shear of a perfect crystal to form a mixed dislocation (left); projection normal to the glide plane (right). The symbol $\perp$ indicates (the position of) an edge dislocation, \$ (the position of) a screw dislocation, respectively.

1.2 The classical modelling of plasticity

Even though the real (microscopic) mechanisms of (macroscopic) plastic deformation are rather clear, the transition from the microscopic mechanisms to a macroscopic material model for plastic behaviour generally poses a problem. The mesoscopic model discussed in this thesis shows one possibility how this transition can be performed. However, most models that are currently used to describe the plastic behaviour are phenomenologically based and macroscopic by nature, see for instance Lippmann [1].

Remark 1.1: There is no real consent on the actual magnitudes standing behind the terms *microscopic*, *mesoscopic* and *macroscopic* scale. In this thesis, that is essentially residing on the mesoscopic scale, we stick to the specification as follows:

microscopic corresponds to the crystal lattice scale, where the consideration of single dislocations is reasonable ($\sim$ 1 nm),

mesoscopic denotes a scale where the continuous description of dislocations and their densities makes sense ($\sim$ 1 μm),

macroscopic represents the mm-level, but will also be used in the context of a continuum mechanics description of samples which are even smaller ($\sim$ mm).

For most plasticity applications to bulk materials, for instance metal forming processes, the phenomenological continuum constitutive models have been successful for many years. Adapted yield criteria and a refined choice of internal variables, which roughly describe the microstructural or thermodynamic internal state of the material, enabled the modelling even of complicated material behaviours like creep [2] or shape memory effects [3]. Elaborate techniques for the numerical implementation have been developed to facilitate robust and accurate simulations, see for instance Simo & Hughes [4]. Typically, these models describe the material behaviour found from averaging over many grains, so that for example anisotropy, which is related to the orientation of the crystal lattice, cannot be simulated.
However, this is possible in the framework of the models based on the theory of crystal plasticity, which reproduce the behaviour of polycrystalline material by resolving the individual grains [5].

The theory of crystal plasticity

Crystal plasticity provides an anisotropic continuum model for the behaviour of single crystals. The plastic deformation is traced back to the slip systems on which the glide of dislocations accounts for plastic slip, figure 1.3. The respective glide planes are embedded in an elastic continuum. Each slip system is characterised by the unit normal $\boldsymbol{n}$ to its glide plane and the unit slip direction $\boldsymbol{s}$. Assuming the small-strain framework, both quantities are constant in space and time.

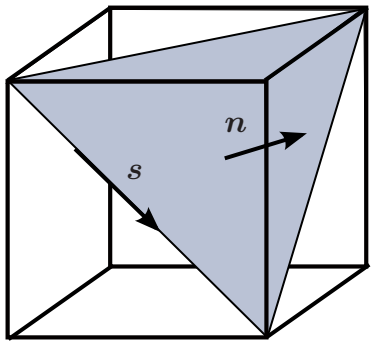

Figure 1.3: A typical slip system in a cubic crystal lattice. The normal to the slip plane $\boldsymbol{n}$ and the unit slip direction $\boldsymbol{s}$ are indicated.

The rate of the plastic distortion $\boldsymbol{\beta}^{\mathrm{p}}$, cf. section 2.3, is defined as:

$$\frac{\partial \boldsymbol{\beta}^{\mathrm{p}}}{\partial t} = \dot{\gamma}^{\mathrm{p}} \boldsymbol{s} \otimes \boldsymbol{n} \,, \tag{1.1}$$

where $\dot{\gamma}^{\mathrm{p}} = \partial\gamma/\partial t$ is the rate of plastic slip. Considering several slip systems, the total plastic flow $\boldsymbol{L}^{\mathrm{p}}$ is the sum of the plastic distortion rates on the respective slip systems, labeled i:

$$\boldsymbol{L}^{\mathrm{p}} = \sum_i \dot{\gamma}^{\mathrm{p}\,(i)} \boldsymbol{s}^{(i)} \otimes \boldsymbol{n}^{(i)} \,. \tag{1.2}$$

Remark 1.2: In the original works on crystal plasticity by Asaro [6, 7], eq. (1.2) was introduced phenomenologically from considerations of the plastic slip on slip planes. Based on the principles of the continuum theory of moving dislocations, section 2.3.2, Sedláček [8] established a relation to the continuum theory of dislocations, which substantiates the phenomenological approach.

The dislocation motion on the glide planes is driven by the respective resolved shear stress, given as

$$\tau^{(i)} = \boldsymbol{s}^{(i)} \cdot \boldsymbol{\sigma} \boldsymbol{n}^{(i)} \,, \tag{1.3}$$

where $\boldsymbol{\sigma}$ is the macroscopic stress tensor. In standard crystal plasticity models the amount of plastic slip, respectively its rate, is determined by phenomenological constitutive relations, including yield criteria, hardening laws etc. The continuum dislocation-based model treated in this thesis, presented in detail in chapter 2, relates the plastic slip rate to the density and velocity of continuously distributed curved dislocations by means of the Orowan equation (1.4), cf. section 2.4.4:

$$\dot{\gamma}^{\mathrm{p}} = b \varrho v \,. \tag{1.4}$$

Today's challenges

Today, a number of technical components are becoming smaller and smaller, see for example the wide spectrum of developments in the field of MEMS[2]. This is continuously reviving the research on the strength of materials at a small scale and on associated models. The description of very small components is closely related to the description of materials with microstructure, see also remark 1.3. In both cases the material behaviour can be crucially different from that of bulk, respectively homogeneous, material samples. To say it shortly: the smaller the structure, the stronger it becomes in the sense that it becomes more difficult to cause plastic deformation. One observes this special behaviour for example in the deformation of composites, where distances between reinforcement particles are on the μm-scale, in loading of thin films on substrates, torsion of thin wires, nanoindentation, or also when measuring the frictional resistance between crystalline solids. 'Thin' here always means of the order of magnitude of μm. Arzt [9] gives an excellent overview of the various size effects.

[2] Micro-Electro-Mechanical Systems, that is the integration of mechanical elements, sensors, actuators, and electronics on a common silicon substrate through microfabrication technology.

Remark 1.3: Actually, of course, every material has a microstructure. Relevant in the present context is however only a microstructure that constricts the motion of dislocations, which again results in a mesoscopically inhomogeneous distribution of the plastic deformation. Such a microstructure may result from the grain distribution in the crystal, dislocation patterning or it may be related to the phase morphology of the material. An example for a phase related microstructure are the lamellar areas in pearlitic steels, made of hard and soft lamellae of several μm thickness.
It is important to note that the 'smaller is harder' relation is valid only down to a length scale of approximately 50 nm. This affects for example the class of ultra-fine grained materials[3]. Below a critical grain size, grain boundary phenomena gain in importance, which may even soften the material response.
Another likewise exception from the standard behaviour was observed in nanoindentation experiments. A saturation of the dislocation density under extremely small indenters prevents the measured strength from becoming arbitrarily high for decreasing indenter size [10].
Therefore the relation 'smaller is harder - even smaller may be softer' might be more appropriate.

In the next section, a rough classification of the size effects is given. While the modelling can be done phenomenologically, explanations for these effects have to be sought on the dislocation level, if not even below, on the atomistic scale. This fact gives rise to numerous physically-based models. Sections 1.3.1 and 1.3.2 give a general survey of the most common modelling approaches.

1.3 Plasticity on the μm-scale

The properties of samples of μm-extent or of materials with a microstructure are determined by the interaction of two different length scales. The first one, the so called *characteristic length*, is the dimension correlated to the physical phenomenon involved (for instance the dislocation spacing or density). The second one is some microstructural dimension (for instance the thickness of a thin film or the grain size), denoted as the *size parameter* [9].
One can distinguish three main types of size effects[4].

1. Size effects due to inherent gradients of plastic strain. Size effects in μm-scaled samples can be observed when the deformation itself is inhomogeneous, thus involving gradients of the plastic strain. Examples of such deformations are the bending of free-standing crystalline strips, torsion of wires or nanoindentation, figure 1.4. The incompatible deformation requires the generation of dislocations, the so called **G**eometrically **N**ecessary **D**islocations. It is generally accepted that the GNDs can give rise to size effects [11]. For a further discussion on GNDs see remark 2.2 and the review article of Gao & Huang [12].

[3] that is materials with a uniform grain size of about 200-300 nm and below
[4] Distinction freely after a talk by E. van der Giessen at the IUTAM Symposium on Plasticity at the micron scale, Copenhagen 2006.

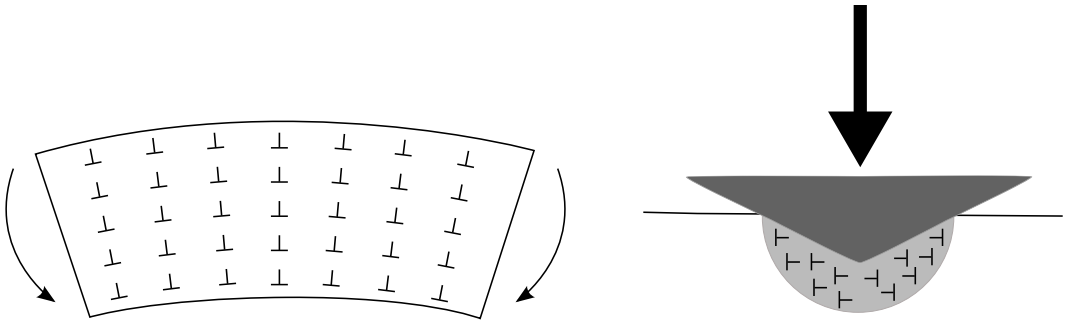

Figure 1.4: Geometrically necessary dislocations in bending of a beam (left) and nanoindentation (right). Bending: in the lower part, that is below the neutral line, there is too much material, whereas in the upper part there is a lack of material. Dislocations form to compensate this incompatibility. Nanoindentation: the simple theory of Nix & Gao [13] assumes, that dislocation loops are injected only in the hemispherical volume under the indenter to redistribute the squeezed material.

2. Size effects due to induced gradients of plastic strain. Even a homogeneous deformation can induce gradients of the plastic strain, provided the dislocation motion inside the material is constrained by some mechanism. The constraint can be due to obstacles, interfaces which are impenetrable for dislocations (like passivation layers or the matrix/particle interfaces in some composite structures) or grain boundaries. The dislocation structures that develop are also referred to as GNDs [11].

The Orowan mechanism is the best known example for a size effect based on confinement and line tension properties. Its original appearance is sketched in figure 1.5(a): a dislocation meeting a couple of obstacles bows out between the obstacles up to half of a circular loop, which requires a bowing stress $\tau_{\mathrm{Or}} \propto \mu b/d$, the Orowan stress, where μ is the shear modulus and b the magnitude of the Burgers vector. Hence the material's strength is inversely proportional to the size parameter, here the obstacle spacing d. But the Orowan mechanism can also be generalised to any necessary bow out of dislocations, for example between the impenetrable surfaces of a passivated film or between reinforcement fibres in a composite material. The size effect that is predicted by the model presented and implemented in the first part of this thesis is based on this mechanism.

A second common source of induced gradients is due to the formation of dislocation pile-ups, for example against grain boundaries. This effect is well known as the basis of the Hall-Petch relation for polycrystals, figure 1.5(b), which predicts that the strength of a material is inversely proportional to the square root of the grain size.

In the second part of this thesis, a corresponding mechanism will be introduced as an additional source for size-dependence in the present continuum dislocation-based model by the concept of the back stress.

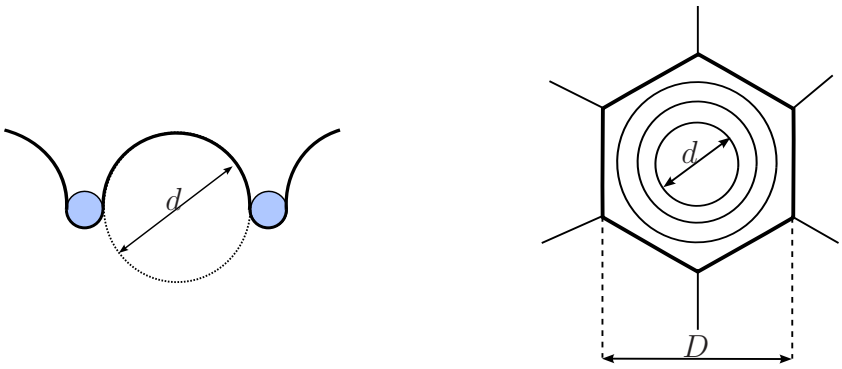

(a) Orowan mechanism (b) Hall-Petch mechanism

Figure 1.5: (a) Orowan mechanism: $\tau_{\mathrm{Or}} \propto \mu b/d$. (b) Hall-Petch mechanism: $\tau_{\mathrm{HP}} \sim \frac{\mu b}{\sqrt{D}} \ln \frac{D}{r_0}$, r_0 lower cut off radius $\sim b$. Compare [9].

3. Size effects in absence of gradients of the plastic strain. There are experiments, where size effects can be observed even though no gradients of plastic strain exist, see for example the compression experiments on single crystalline, (sub-)μm-sized pillars, figure 1.6. The size effects in these cases are ascribed to starvation effects [14]: free surfaces of the sample act as an effective sink for dislocations during plastic deformation. The dislocations are likely to leave the small samples before multiplication mechanisms can occur. The loss of dislocations entails a higher flow stress.
Continuum theories, see below, cannot be used to describe correctly this kind of size effect. However, only recently discrete dislocation dynamics simulations could successfully reproduce the observed size effect [15].

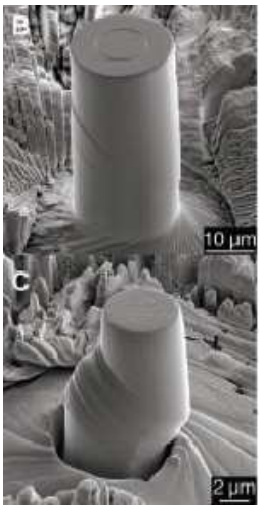

Figure 1.6: A microscopic pillar under pressure - Uchic and co-workers observed a size effect in the response of pillars of different diameter, even though no strain-gradients can be present in this type of deformation [16].

The remainder of this chapter gives a survey of the most popular, currently followed modelling approaches that account for size effects in the plasticity on the μm-scale. The first group of

discrete theories are able to reproduce the mechanisms introduced above. In contrast, for the second group, the continuum approaches, these mechanisms form the basis of the modelling.

1.3.1 Discrete theories

The term 'discrete theories' is used here as a generic term for all the models describing *individual* dislocations or even atoms and their mutual interactions. All these models are mostly of academic interest rather than in reach of a wide technical application. This is due to the high computational effort and the severe size and time restrictions on the simulated processes.

Discrete dislocation dynamics...

...with edge dislocations represented as points. A very fertile approach was proposed by van der Giessen and Needleman in 1995 [17]. It accounts for the glide of straight edge dislocations piercing perpendicularly through the simulation plane and thus being represented as point-like objects. The driving force for the glide of these objects is the Peach-Koehler force, which is supposed to be in equilibrium with a drag force and the Peierls stress (lattice friction), thus providing an equation of motion for the dislocations. The Peach-Koehler force itself is determined based on the solution of a boundary value problem, that provides the strain and stress fields of the considered individual dislocations. Note that the continuum part of the modelling is based on the linear elasticity theory[5] which enables the usage of a superposition principle for the solution of the boundary value problem. The idea is to make use of the known solutions in infinite space and to superpose an 'image' solution to correct for the boundary conditions. The model accounts also for annihilation and dislocation sources. The notion of a constitutive law is not used.
Various applications of the approach have been presented in the last decade. Some of the latest are the plastic flow in a composite [18, 19], crack modelling [20], size effects in thin films [21, 22], constrained shearing [23], bending [24] and nanoindentation [25]. Within these works, the model has been compared with continuum theories regularly, see below. The size effect predicted by this model is due to the formation of dislocation pile-ups against impenetrable interfaces or in an inhomogeneous stress field. Current efforts in the field concern the introduction of line tension effects.

...with dislocations represented as piecewise linear curves. In contrast to the model class described in the previous paragraph, which is essentially two-dimensional, discrete dislocation dynamics based on actual line defects, that is with individual dislocations represented as piecewise linear curves, is three-dimensional. The study of strain hardening and pattern formation in this framework was pioneered by Kubin et al. [26]. Typical simulations as presented in [27–30] are based on roughly 10^4 dislocation segments. The most restrictive part of the model is the computation of pair interactions: the involved computational costs pass those for the consideration of the

[5] which is a reasonable assumption provided the dislocation core is not considered

applied stress or the line tension by far. In the last years, the group around Kubin/Devincre has made an effort on the coupling of the three-dimensional dislocation simulations with a macroscopic continuum model. While the former is based on a lattice of element sizes of order several times the magnitude of the Burgers vector, the discretisation of the latter is much coarser - at least by two orders of magnitude. Therefore, and in order to get an output of the dislocation simulation in terms of continuum variables such as the plastic strain, a sophisticated homogenisation technique has been developed [31]. The resulting discrete continuum method (DCM) handles the dislocation dynamics part as a constitutive model for the continuum mechanics framework, cf. section 3.5.

In contrast to that, during the last five years scientists of various disciplines at the Lawrence Livermore National Laboratory (California) made an effort to the development of a massively parallel dislocation dynamics simulation code, named ParaDiS [32]. Their intention is to allow for the simulation of large dislocation populations (10^6 to 10^8 segments) over quite large time intervals (several seconds) and strain ranges (up to 3%), which is necessary to be representative of bulk material. Today, the code runs on a supercomputer with approximately 130,000 processors. A major cognition based on the ParaDiS simulations is the importance of multijunctions, which establish obstacles of very high strength, and contribute to the total strength in the simulation. Probably here no coupling with continuum mechanics will be established, as the solution of the boundary value problem can hardly be accomplished.

Atomistic simulations

Atomistic simulations, also known as molecular dynamics, can provide an understanding of the mechanisms on the atomic scale, that is how does a crack or a dislocation nucleate, how are twins built, what happens at grain boundaries, etc. Today, atomistic simulations are restricted to about 10^6 atoms, depending on the numerical approximation chosen for the atomic interactions, which follow Newton's equation of motion. The interaction forces are basically determined by the Lennard-Jones pair potential. The largest problem is probably the constraint, that the time step for the numerical procedure must be a factor 10-100 smaller than the inverse Debye frequency, that results in $\Delta t \sim 10^{-15}$s, thus requiring 10^6 time steps for the simulation of 1 ns. Therefore, thermally activated processes, which are slow in nature, cannot be a subject of atomistic simulations. Note that in contrast to the Monte Carlo method, which stochastically finds the thermodynamically relaxed state of a system of molecules, the molecular dynamics approach is deterministic and restricted to short time scales and dynamic situations, such as can be found in fracture and plasticity.

The latest development deals with the coupling of atomistic simulations with larger scale models [33, 34]. These multi-scale approaches are supposed to enable simulations on a feasible scale including mechanical boundary value problems, where the atomistic part is restricted only to a small process zone, for example the zone around a crack tip.

1.3.2 Continuum theories

Generalised continua

Generalised continua [35, 36], also called continua with microstructure, are characterised by having more degrees of freedom than the classical continuum. These additional degrees of freedom can be employed to describe the microstructure of a material.
The most familiar among the generalised continua are probably the micromorphic medium due to Mindlin and Eringen [37, 38] and the Cosserat medium. The latter expands the classical continuum by additional rotational degrees of freedom. It was developed by the brothers Cosserat almost 100 years ago [39]. Recently it has been revisited by several authors to model special material classes like for example liquid crystals, granular media, cellular solids or dislocated crystals [40]. Actually, Cosserat media account for the influence of GNDs on the hardening behaviour of metals. Therefore they provide another efficient way to model size effects in crystals, see for instance the articles by Forest & Sedláček [41, 42] as well as [43, 44].
Unfortunately, a connection between the values of the characteristic lengths in generalised continua models and the actual material state is difficult to establish [41].
An excellent review of generalised continuum crystal plasticity models can be found in [45].

Strain-gradient models

The geometrically necessary dislocations introduced in the beginning of section 1.3 are the result of gradients of the plastic shear [46]. One possible way to bring in size effects into the constitutive laws of plasticity is therefore to postulate, that the hardening depends on both plastic strain and plastic strain-gradient. This is the foundation of the so called strain-gradient or second gradient models, which are designed to account for the size effects based on gradients of the plastic strain. A phenomenological material length scale that enters these models determines the impact the GNDs make: the smaller the length scale, the more important the strain-gradient effects become.
A strain gradient theory with symmetric stress and based on the classical plasticity theories was formulated by Aifantis [47]. The derivation of this model is not directly related to the dislocation density tensor or to the concept of GNDs, but is rather based on a model of reaction-diffusion type for the dislocation evolution. In its simplest form this strain gradient plasticity theory involves only one extra coefficient incorporating the effect of the Laplacian of the effective shear strain into the constitutive expression for the flow stress. Aifantis further generalised the concept to the gradient of internal variable approach [48], see the review article by Forest [45]. Aifantis' model is very well suited for addressing stability and deformation patterning problems [49].
However, most of the current theories rely on the fundamental work of Fleck et al. [50] who developed a strain-gradient-based constitutive law including asymmetric stress formulation. This approach can also be categorised in the group of generalised continua, see below, as it corre-

sponds to the couple stress theory which goes back to Koiter [51].
Strain-gradient models are able to successfully describe size effects, the finite width of shear bands and also crack-tip plasticity. An open problem to these models is the choice of internal length scales and of higher order boundary conditions, which cannot be made based on a physical background. Rather, they are used as fitting parameters to achieve a good representation of experimental results.
Currently there is a lot of research activity in the field of strain-gradient theories. There are for instance attempts to introduce anisotropic considerations in the theory [52], to take into account contributions of grain boundaries [53], or to enable the treatment of evolving interfaces between plastic and elastic zones, which requires a special consideration of the inner boundary conditions, for example by second order strain-gradients [54].

A field-model of crystal plasticity based on continuum dislocation mechanics

Acharya [55] proposed a phenomenological field model for the elastic-plastic response of mesoscopic single crystals based on the continuum mechanics of continuously distributed dislocations. The model, which has been further developed and generalised for finite deformations [56, 57], incorporates the elastic theory of dislocation distributions and internal stress exactly. Dislocations are not described as lines or inherently considered by some evolution law for the plastic slip, but based on the dislocation density as field variable. A system of partial differential equations is established that characterises the evolution of an equilibrium between the elastic stress field related to the presence of dislocations and the stress field due to the boundary conditions imposed on the considered body. The clear mathematical structure allows for a Finite Element implementation of the model, which has been realised recently [58].
As the model goes down to the very basics that make up a dislocation, namely the stress field along the line of a defect in the lattice structure, section 1.1, it can be considered to be the model for plasticity on the microscale which resides on the lowest possible scale. But this high resolution also entails the problem that a transition of the model to the macroscale is very difficult. At the moment it is restricted to applications to individual dislocations.

Statistical theories

Inspired by the statistical approach to dislocation dynamics originally suggested by Kröner [59], a number of statistically based descriptions of dislocation fields have been considered recently.
Using averaging procedures adopted from the statistical mechanics of interacting many-particle systems, Groma and co-workers developed a statistical continuum description of the collective behaviour of discrete straight parallel edge dislocations [60–63]. The dislocations are restricted to their slip planes, and pierce perpendicularly to the simulation plane. Since their trace is only a point, it is reasonable to treat them as point-like particles and to apply the concepts of statistical mechanics. Starting from the equation of motion for single dislocations, the continuum model is

derived by means of demanding statistical averaging, and is finally given in terms of dislocation correlation functions. This approach represents a continuous counterpart to the two-dimensional discrete dislocation dynamics of van der Giessen and Needleman, section 1.3.1. Absolute values of the model parameters result from an averaging of hundreds of discrete dislocations simulations. In one of the latest works [62], Groma et al. proposed to separate the statistical parts of their model and make them collapse to a constant factor entering the continuum part, which can be determined once and for all by a large number of stochastic simulations. A future task is to generalise the model to multiple slip arrangements. First steps in this direction were already presented by Kratochvíl et al. [64].

However, applying statistical methods turns out to be by far more challenging for systems of curved dislocations. In this case, Hochrainer [65] defines a 'statistical measure' for e.g. the dislocation density by its disability to give a complete picture of the described dislocation state in the sense that some averaging entails a loss of information necessary to reconstruct the actually connected dislocation lines.

El-Azab [66] presented one of the first concepts for the description of general curved dislocations based on the methods of statistical mechanics. Enhancing Kosevich's idea published in the 70s [67], he introduced for each slip system a statistical measure, namely a distribution function ϕ in the phase space consisting of the actual location of the considered dislocation segment $\boldsymbol{x}$, its velocity $\boldsymbol{v}$, and its orientation $\boldsymbol{\theta}$. With this approach El-Azab did pioneer work that inspires researchers until today. But up to now, the problems that go along with the fact, that one has to consider connected dislocation lines rather than a system of unconnected dislocation segments have not been addressed, such that his approach did not yield results of practical interest so far.

Based on an elaborate and rigorous mathematical framework[6], Hochrainer and co-workers [65, 68, 69] very recently generalised Groma's approach and proposed a statistical field theory for curved dislocations. It is constructed by statistical means, too, but yields a higher-order deterministic density measure that allows for a reconstruction of the connected dislocation lines and the definition of a meaningful velocity field. For details and a discussion on this approach the reader is referred to section 2.5.

Continuum dislocation-based model

The continuum dislocation-based model was first introduced by Sedláček in [70]. Introducing the line tension of dislocations, which makes a non-negligible contribution to various size effects, and describing the behaviour of continuously distributed dislocations by a small number of field variables, the model aims at being both closer to physics than the phenomenological ones and computationally more efficient than the discrete approaches. A coupling of the dislocation-based material model to the framework of continuum mechanics is accomplished by means of

[6] Concepts from differential geometry and differential calculus are extensively used, e.g. calculus on differentiable manifolds, lifts (of curves), differential forms, currents, etc.

the theory of crystal plasticity, section 1.2. This model is actually the first valuable approach that rigorously considers the curved character of dislocations in a continuum way. Even though many processes like nucleation, annihilation or climb are not contained in the model yet, it is able to explain various types of size effects by the mere consideration of the line tension, and thus based on the Orowan mechanism, figure 1.5(a). Up to now, the model has been mostly applied to problems that can be formulated in one dimension (1D).

Figure 1.7 shows typical results based on the continuum dislocation-based model. A constant resolved shear stress is presumed to act on a continuous distribution of dislocations in their slip plane. The individual dislocations are pinned at the boundary of the considered interval[7] along the slip direction x. Such a situation is representative for example of the constrained glide of dislocations in a thin strip with impenetrable interfaces or in a composite structure, where the point where a dislocation meets a matrix/particle interface acts as such a boundary. The shape of a representative dislocation line $\varphi_y(x)$ of the considered field is shown in the left part of figure 1.7. The model correctly predicts that the dislocation bows out under the effect of the shear stress and takes a curved shape. This shape corresponds to the distribution of plastic slip. The right part of the figure shows the orientation ϑ of the dislocation line, that is in this depiction the angle enclosed by the x-axis and the tangent to the curve φ_y. The solid line corresponds to a three times higher load compared to that applied for the dashed solution. The situation changes qualitatively when the load is further increased as then the bowing dislocation reaches the impenetrable boundaries. In the limit case one speaks of the 'critical' bow-out or configuration. It corresponds to a surface orientation of $|\vartheta| = \pi/2 \sim 1.57$. Henceforth the dislocation cannot bow out any stronger, but it will glide along the channel, depositing misfit dislocations at the interfaces.

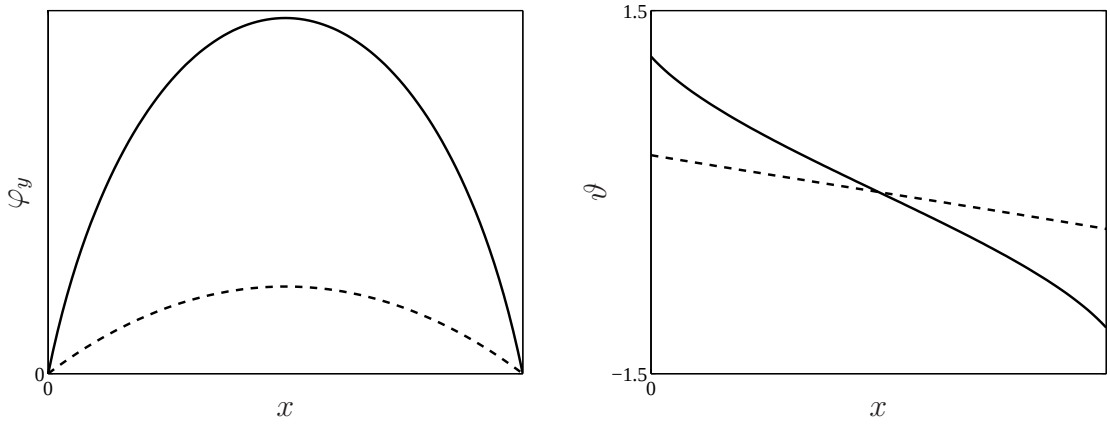

Figure 1.7: Typical qualitative results of the continuum dislocation-based model for a constrained geometry and constant applied load. The left sketch shows the shape of a representative dislocation of the considered field of dislocations. On the right side the corresponding orientation of the dislocation is depicted. The solid line corresponds to a three times higher load compared to that applied for the dashed solution.

[7] The length of the interval corresponds to the size parameter, see the introduction to this section.

1.4 Outline of the thesis

The two major purposes of this thesis are:

- the development of a robust numerical implementation of the continuum dislocation-based model, including the coupling with the Finite Element implementation for two-dimensional mechanical problems that can be treated in the plane-strain framework,
- the enhancement of the model by an additional short-range stress field, the back stress.

The work is organised as follows: In chapter 2, the classical continuum dislocation-based model is introduced. Staying close to the original publications of Sedláček [8, 70], we first introduce the description of single dislocations as parametric curves. An equation of motion for single dislocations based upon the effects of Peach-Koehler force, line tension and viscous dissipation is derived. As a motivation for the actual modelling based on single-valued dislocation fields, the classical continuum theory of dislocations is discussed. Then the Eulerian and Lagrangian model equations for single-valued dislocation fields are derived, and the coupling to continuum mechanics is demonstrated. The chapter closes with a short discussion on the possible treatment of multiple-valued dislocation fields by the present model, which is compared to the potentials of the very recent approach of Hochrainer.
Chapter 3 deals with the numerical implementation of the continuum dislocation-based model for two-dimensional problems. The problems that were present from the very beginning of a numerical realisation of the model are reconsidered. It turns out that a convection-dominated convection diffusion problem is faced which has to be treated with special numerical techniques. The chapter closes with a detailed presentation of the implementation of the coupling of the model to continuum mechanics in form of a Finite Element code for plane strain problems, and an outlook to the intended coupling with a standard FE software.
The second part of the thesis addresses the enhancement of the model by an additional short-range stress field, the back stress. This contribution accounts for the mutual interactions of dislocations in more detail than the simple Taylor relation.
Chapter 4 gives a short theoretical introduction to the concept of the back stress, which can be interpreted as a generalised pile-up stress. After reconsidering two earlier approaches to the integration of this stress field into continuum models, we define the back stress as it will be used in the continuum dislocation-based model and derive the augmented equation of motion. In advance of earlier approaches, here a distinction for the back stress acting between parallel and non-parallel dislocations is made. The chapter is closed by a fundamental investigation of the enhanced model on the basis of a simple model problem.
The effect of the additional short-range stress field on the results of a previous application of the classical model is studied in chapter 5. For the reader's convenience, the problem setting for the standard application 'shearing of a thin crystalline strip' and the interpretation of the source-shortening by the classical model are recapitulated. Finally the influence of the new stress field

on these results is investigated.
The thesis closes with a short resume and an outlook to future tasks. The appendix contains a list of the frequently used symbols in this thesis, a summary of important mathematical relations, some useful relations between the field variables and technical notes on some of the used software, namely ZeBuLoN, PVM and Fortran.

CHAPTER 2

Continuum dislocation-based plasticity

> According to our present experience we may trust in the fact, that nature is the realisation of what is mathematically the most simply imaginable.
>
> *Albert Einstein (1879-1955)*

This chapter resumes the set up of the continuum dislocation-based model introduced by Sedláček et al. in [70]. It is the result of the coupling of a mesoscopic description of continuously distributed dislocations with the small strain continuum mechanics framework, which is established by the principles of crystal plasticity.

The dislocation-related part of the model is, like every modelling approach, due to some assumptions. Dislocations are supposed to be planar and bound to their glide planes. The interaction of dislocations on intersecting glide planes is accounted for by means of the Taylor relation for the yield stress, section 2.4.5. Dislocation generation and annihilation are not explicitly modelled, yet. Long range interactions are considered only indirectly by the coupling to continuum-mechanics.

The short-range elastic fields, that are absent in the classical continuum theory of dislocations, are decisive for the dislocation interactions that determine the size-dependent plastic response. One of the most important interactions, especially when plasticity of small confined volumes is considered, is the self force of curved dislocations. It is explicitly reintroduced in the model by means of the line-tension concept. This approach was pioneered by Kratochvíl and Saxlová [71] and has been further developed by Sedláček in the last years. The mutual interactions between dislocations are not explicitly considered by the classical model. These short-range interactions come only with the standard Taylor relation for the yield stress.

This chapter is organised as follows. In the first section, the description of individual dislocations as parametric curves is set up. In section 2.2 an equation of motion for individual dislocations

is derived. Starting with a short introduction to the elastic properties of a dislocation, the forces considered for a static equilibrium are introduced. That is the Peach-Koehler force, related to the energy of a dislocation in an applied stress field, W_{F}, and the dislocation self force, related to the self energy of a dislocation, W_{S}, which is a consequence of its elastic energy. Assuming a viscous dissipation energy related to the glide of dislocations, W_{G}, finally the equation of motion for individual dislocations can be established.

To motivate the modelling approach based on single-valued dislocation fields, section 2.3 provides a short review of the classical continuum theory of dislocations. Kröner's dislocation density tensor, the notion of (in-)compatible distortion and the fundamental field equation for moving dislocations are presented. As the classical concept provides only information on the average dislocation density, a different density measure is required to set up a meaningful model. Therefore, in section 2.4 the notion of single-valued dislocation fields is introduced. All characteristic quantities describing the dislocations belonging to the considered field are unique functions of position and time. This concept potentiates the present model for the description of continuously distributed dislocations. The section is closed with a resume of its coupling to the small-strain framework of continuum mechanics.

The last part of the chapter is devoted to the modelling of multiple-valued dislocation fields. Their possible treatment by the present model is compared to the potentials of the model recently proposed by Zaiser and Hochrainer [65, 68, 69, 72–74].

2.1 Description of a single curved dislocation

Staying close to the presentation in [8], we introduce the description of individual dislocation lines as parametric curves. This will be the basis for the specification of fields of continuously distributed dislocations in section 2.4. For an introduction to the differential geometry of curves the reader is referred to the textbook of do Carmo [75].

Assume a planar dislocation line with Burgers vector $\boldsymbol{b} = b\boldsymbol{s}$ and unit tangent $\boldsymbol{\xi}$, where $\boldsymbol{s}$ is the unit vector of the slip direction. Assuming the dislocation is not purely screw, we define the unit normal to the slip plane $\boldsymbol{n}$ and the unit normal to the dislocation line $\boldsymbol{\nu}$ [1] as

$$\boldsymbol{n} = \frac{\boldsymbol{s} \times \boldsymbol{\xi}}{|\boldsymbol{s} \times \boldsymbol{\xi}|}, \qquad \boldsymbol{\nu} = \boldsymbol{n} \times \boldsymbol{\xi} \;\leftrightarrow\; \boldsymbol{n} = \boldsymbol{\xi} \times \boldsymbol{\nu}\,. \tag{2.1}$$

Only small deformations are considered, so $\boldsymbol{b}, \boldsymbol{s}, \boldsymbol{n}$ can be assumed constant in space and time. A planar coordinate system in the glide plane is defined by the unit vectors

$$\boldsymbol{e}_x = \boldsymbol{s}\,,\; \boldsymbol{e}_y = \boldsymbol{n} \times \boldsymbol{s}\,. \tag{2.2}$$

It can be completed to a three dimensional coordinate system by a third unit vector $\boldsymbol{e}_z = \boldsymbol{n}$.

[1] Note that the bold symbol for the unit normal to the dislcoation line $\boldsymbol{\nu}$ is not related to the symbol ν for the Poisson number.

Let a dislocation line in the considered glide plane be defined as a parametric curve, that is for every value of a parameter $r \in [r_i, r_e]$ a point of the curve in the slip plane coordinate system is defined by the mapping

$$\boldsymbol{\varphi}(r) = \begin{pmatrix} \varphi_x(r) \\ \varphi_y(r) \end{pmatrix} , \tag{2.3}$$

see figure 2.1. From the mapping $\boldsymbol{\varphi}$, the unit tangent and normal to the dislocation line are

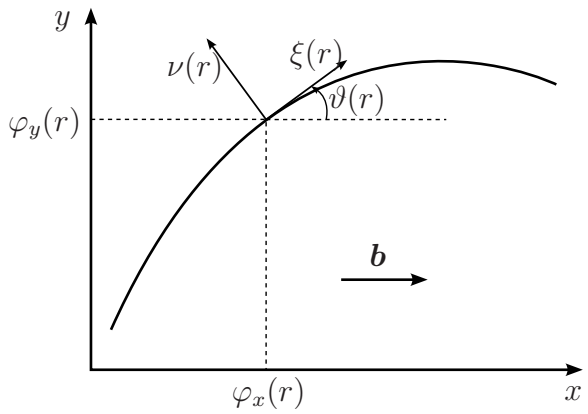

Figure 2.1: A planar dislocation described as parametric curve in the slip plane coordinate system.

derived as

$$\boldsymbol{\xi}(r) = \frac{1}{|\boldsymbol{\varphi}'|} \begin{pmatrix} \varphi_x'(r) \\ \varphi_y'(r) \end{pmatrix} , \; \boldsymbol{\nu}(r) = \frac{1}{|\boldsymbol{\varphi}'|} \begin{pmatrix} -\varphi_y'(r) \\ \varphi_x'(r) \end{pmatrix} , \tag{2.4}$$

where the prime denotes the derivative with respect to the parameter, here r, and the absolute value $|\boldsymbol{\varphi}'|$ represents the Euclidean norm:

$$|\boldsymbol{\varphi}'| = \sqrt{{\varphi_x'}^2 + {\varphi_y'}^2} . \tag{2.5}$$

The angle ϑ between Burgers vector resp. slip direction and the tangent to the dislocation line, also denoted the orientation of the dislocation line, meets

$$\sin\vartheta = \frac{\varphi_y'}{|\boldsymbol{\varphi}'|} , \quad \text{and} \quad \cos\vartheta = \frac{\varphi_x'}{|\boldsymbol{\varphi}'|} . \tag{2.6}$$

Combining eqs. (2.4) and (2.6) alternative expressions for the unit tangent and normal are found:

$$\boldsymbol{\xi} = \begin{pmatrix} \cos\vartheta \\ \sin\vartheta \end{pmatrix} , \qquad \boldsymbol{\nu} = \begin{pmatrix} -\sin\vartheta \\ \cos\vartheta \end{pmatrix} . \tag{2.7}$$

The curvature of the planar curve (2.3) for an arbitrary parametrisation is defined as

$$\kappa = \frac{\varphi_x'\varphi_y'' - \varphi_y'\varphi_x''}{({\varphi_x'}^2 + {\varphi_y'}^2)^{3/2}} . \tag{2.8}$$

Natural parametrisation

A special choice for the parameter is the arc length of the considered curve, $\mathfrak{s} \in [0, \mathfrak{S}]$, which is related to an arbitrary parameter r by

$$\mathfrak{s}(r) = \int_{r_i}^{r} |\boldsymbol{\varphi}'(\varsigma)| \, \mathrm{d}\varsigma \,, \tag{2.9}$$

where $\mathfrak{S} = \mathfrak{s}(r_e)$ is the total length of the curve. As $\mathfrak{s}(r)$ is continuous and strictly monotonic increasing, there exists an inverse function $r(\mathfrak{s})$. Consequently the respective differentials are related according to

$$\mathrm{d}\mathfrak{s} = |\boldsymbol{\varphi}'(r)| \, \mathrm{d}r \,. \tag{2.10}$$

The derivative of a curve given in arc length parametrisation, $\mathrm{d}\boldsymbol{\varphi}(\mathfrak{s})/\mathrm{d}\mathfrak{s}$, has magnitude 1, so

$$\frac{\mathrm{d}\boldsymbol{\varphi}(\mathfrak{s})}{\mathrm{d}\mathfrak{s}} = \boldsymbol{\xi} \,. \tag{2.11}$$

The local curvature is then given as

$$\kappa(\mathfrak{s}) = \left| \frac{\mathrm{d}^2\boldsymbol{\varphi}(\mathfrak{s})}{\mathrm{d}\mathfrak{s}^2} \right| \quad \leftrightarrow \quad \frac{\mathrm{d}\boldsymbol{\xi}(\mathfrak{s})}{\mathrm{d}\mathfrak{s}} = \kappa(\mathfrak{s})\boldsymbol{\nu}(\mathfrak{s}) \qquad (1^{\mathrm{st}} \text{ Frenet formula, [75]}) \,. \tag{2.12}$$

2.2 The motion of dislocations

The motion of dislocations is the predominant source of the plastic deformation of crystalline materials. It is due to a disequilibrium of the forces that act on or between the dislocations. In this section, only the forces as presented by Sedláček [8, 70, 76] are considered, that is the Peach-Koehler force in the glide plane and the dislocation self force. Possibly, one may consider the yield resistance in the sense of a third force, but as it differs from the previous ones by its passive character we concern it separately in section 2.4.5. The resulting equation of motion for individual dislocations is based on the assumption of a viscous dissipation accounting for the dynamic equilibrium.

2.2.1 Static equilibrium of forces

Based on variational considerations on energies, we want to give a short derivation of Peach-Koehler and dislocation self forces. Both can be traced back to the elastic strain energy related to a dislocation.

Elastic properties of a dislocation

Around a dislocation line, the crystal has undergone a certain amount of distortion, which entails the presence of an extra strain energy in the dislocated body. This strain energy is composed of an elastic part and of a part related to the dislocation core. The latter is not treated here, as it

is not of importance in the mesoscale approach. The elastic field of a mixed dislocation is the superposition of the fields of its edge and screw parts. For an elastically isotropic crystal the elastic energy of a mixed dislocation results as,

$$\begin{aligned} W_{\mathrm{el}} &= \frac{\mu}{4\pi}\left[(\boldsymbol{b}\cdot\boldsymbol{\xi})^2 + \frac{1}{1-\nu}|\boldsymbol{b}\times\boldsymbol{\xi}|^2\right]\ln\left(\frac{R}{r_0}\right) = \\ &= \left[\frac{\mu b^2\sin^2\vartheta}{4\pi(1-\nu)} + \frac{\mu b^2\cos^2\vartheta}{4\pi}\right]\ln\left(\frac{R}{r_0}\right) = \frac{\mu b^2(1-\nu\cos^2\vartheta)}{4\pi(1-\nu)}\ln\left(\frac{R}{r_0}\right), \end{aligned} \tag{2.13}$$

see for instance the textbook of Hull & Bacon [77, chap. 4]. Here R is an outer cut off radius ($\sim$ crystal size or dislocation spacing) and r_0 is the core radius ($\sim b$). Choosing realistic values for the radii and introducing a constant $\alpha = 0.4\ldots1.0$, an approximation of the elastic energy results as

$$W_{\mathrm{el}} = \alpha\mu b^2\,. \tag{2.14}$$

Dislocation in a stress field – the Peach-Koehler force

The Peach-Koehler force is the force acting on a dislocation due to an applied stress field $\boldsymbol{\sigma}$, which actually interacts with its elastic strain field.
Consider a closed planar dislocation loop which borders the area A_{L}, compare figure 1.1. The work spent by the applied stress when the dislocation is created is

$$W_{\mathrm{F}} = \int_{A_{\mathrm{L}}} \boldsymbol{b}\cdot\boldsymbol{\sigma}\,\mathrm{d}\boldsymbol{a}_{\mathrm{L}}\,. \tag{2.15}$$

The argument can be understood as a force $\boldsymbol{\sigma}\,\mathrm{d}\boldsymbol{a}_{\mathrm{L}}$ brought onto an infinitesimal area element times the amount $\boldsymbol{b}$ by which it is displaced.

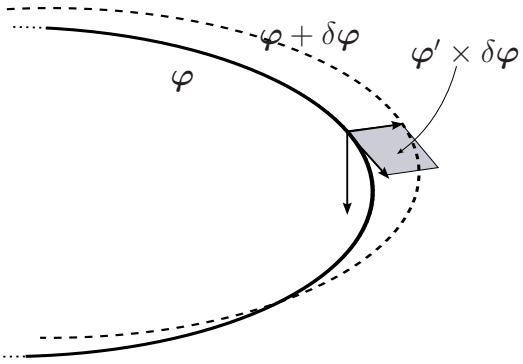

Figure 2.2: Cut-out of a closed dislocation loop before (solid line) and after (dashed) the displacement by $\delta\varphi$. The area increment $\varphi' \times \delta\varphi$ is indicated.

Consider now the virtual work δW_{F} done by the stress field when the dislocation is displaced in its glide plane by an arbitrary, without loss of generality, perpendicular translation $\delta\varphi$, see figure 2.2. If every line element $\mathrm{d}r$ of the loop is displaced, the area A_{L} changes by increments $\varphi'\times\delta\varphi$ and the stress does the additional work

$$\delta W_{\mathrm{F}} = \int_{r_i}^{r_e} \boldsymbol{b}\cdot[\boldsymbol{\sigma}(\varphi'\times\delta\varphi)]\,\mathrm{d}r = \int_0^{\mathfrak{S}} [(\boldsymbol{b}\cdot\boldsymbol{\sigma})\times\boldsymbol{\xi}]\cdot\delta\varphi\,\mathrm{d}\mathfrak{s}\,. \tag{2.16}$$

The expression $(\boldsymbol{b}\cdot\boldsymbol{\sigma})\times\boldsymbol{\xi}$ is the Peach-Koehler force [78] per unit length.
In the case of a planar dislocation and planar displacement $\delta\boldsymbol{\varphi}$, the expression can be further simplified yielding

$$\delta W_{\mathrm{F}} = \int_{r_i}^{r_e} \boldsymbol{b}\cdot\boldsymbol{\sigma}\boldsymbol{n}\,(-\varphi_y'\delta\varphi_x + \varphi_x'\delta\varphi_y)\,\mathrm{d}r = \int_0^{\mathfrak{S}} (\boldsymbol{b}\cdot\boldsymbol{\sigma}\boldsymbol{n})\,\boldsymbol{\nu}\cdot\delta\boldsymbol{\varphi}\,\mathrm{d}\mathfrak{s}\,, \tag{2.17}$$

where we used eq. (2.4) for $\boldsymbol{\nu}$ and $\boldsymbol{e}_z = \boldsymbol{n}$. This expresses, that the Peach-Koehler force of magnitude $\boldsymbol{b}\cdot\boldsymbol{\sigma}\boldsymbol{n} = b\tau$ per unit length acts in the glide plane perpendicular to the dislocation line, that is in direction $\boldsymbol{\nu}$. Here it was used that $\tau = \boldsymbol{s}\cdot\boldsymbol{\sigma}\boldsymbol{n}$ is the resolved shear stress in the considered slip system, eq. (1.3), and $\boldsymbol{b} = b\boldsymbol{s}$.

Dislocation self force – the line tension

The elastic strain energy (2.13) results in a self energy W_{S} carried by every dislocation. The variation of self energy is defined as

$$\delta W_{\mathrm{S}} = \delta\left(\int_0^{\mathfrak{S}} W_{\mathrm{el}}(\boldsymbol{\varphi}')\,\mathrm{d}\mathfrak{s}\right)\,. \tag{2.18}$$

Applying the variational principle and assuming either closed dislocation loops or dislocations which are pinned at $\mathfrak{s}=0$ and $\mathfrak{s}=\mathfrak{S}$, yields

$$\delta W_{\mathrm{S}} = \int_0^{\mathfrak{S}} \left[\left(W_{\mathrm{el}} + \frac{\mathrm{d}^2 W_{\mathrm{el}}}{\mathrm{d}\vartheta^2}\right)\frac{\mathrm{d}\cos\vartheta}{\mathrm{d}\mathfrak{s}}\,\delta\varphi_x + \left(W_{\mathrm{el}} + \frac{\mathrm{d}^2 W_{\mathrm{el}}}{\mathrm{d}\vartheta^2}\right)\frac{\mathrm{d}\sin\vartheta}{\mathrm{d}\mathfrak{s}}\,\delta\varphi_y\right]\mathrm{d}\mathfrak{s}\,. \tag{2.19}$$

For a detailed derivation see Sedláček [8, app. B]. The term in round brackets is usually abbreviated by $T(\vartheta)$ and is called line tension.

Static equilibrium of forces

For a dislocation in equilibrium, the virtual work δW_{F} done by the stress field (2.17) is compensated by a variation in the self energy δW_{S} (2.19) caused by the virtual translation $\delta\boldsymbol{\varphi}$:

$$\delta W_{\mathrm{F}} + \delta W_{\mathrm{S}} = 0 \tag{2.20}$$

A combination of eqs. (2.17) and (2.19) yields the Euler-Lagrange equations of the variational problem:

$$0 = \left(W_{\mathrm{el}} + \frac{\mathrm{d}^2 W_{\mathrm{el}}}{\mathrm{d}\vartheta^2}\right)\frac{\mathrm{d}\cos\vartheta}{\mathrm{d}\mathfrak{s}} - b\tau\sin\vartheta\,, \tag{2.21$_1$}$$

$$0 = \left(W_{\mathrm{el}} + \frac{\mathrm{d}^2 W_{\mathrm{el}}}{\mathrm{d}\vartheta^2}\right)\frac{\mathrm{d}\sin\vartheta}{\mathrm{d}\mathfrak{s}} + b\tau\cos\vartheta\,. \tag{2.21$_2$}$$

Using eq. (2.7) and the line tension, the system simplifies to

$$T(\vartheta)\frac{\mathrm{d}\boldsymbol{\xi}}{\mathrm{d}\mathfrak{s}} + b\tau\boldsymbol{\nu} = \boldsymbol{0}\,. \tag{2.22}$$

In view of the Frenet formula (2.12) this expression represents the equilibrium of Peach-Koehler and dislocation self force $T(\vartheta)\kappa$ in perpendicular direction to the dislocation line:

$$(T(\vartheta)\kappa + b\tau)\,\boldsymbol{\nu} = \mathbf{0}\,. \tag{2.23}$$

The dislocation self force is proportional to the curvature of the dislocation line. This is intuitively clear, as a straight dislocation, $\kappa = 0$, minimises its elastic self energy. From (2.13) we derive the orientation dependent expression,

$$T(\vartheta) = \frac{\mu b^2}{4\pi(1-\nu)}(1 - 2\nu + 3\nu\cos^2\vartheta)\ln\left(\frac{R}{r_0}\right)\,, \tag{2.24}$$

which is frequently, also in this thesis, approximated by the orientation independent expression

$$T = \mu b^2\,. \tag{2.25}$$

The static equilibrium of forces in normal direction to the dislocation line,

$$T\kappa + b\tau = 0\,, \tag{2.26}$$

can be used as a basis for a numerical scheme, that approximates the quasistationary or relaxed state of a system, see section 3.2.1.

2.2.2 Equation of motion

A dislocation that is not in a relaxed state, that is for which the equilibrium (2.23) does not hold, tends to approach the equilibrium by glide. As the dislocation moves, its parametrisation becomes time dependent:

$$\boldsymbol{\varphi} = \boldsymbol{\varphi}(r,t) = \begin{pmatrix}\varphi_x(r,t)\\ \varphi_y(r,t)\end{pmatrix}\,. \tag{2.27}$$

The planar movement can, without loss of generality, be assumed to occur in normal direction to the dislocation line. A movement in tangential direction would not change the shape of $\boldsymbol{\varphi}$ and thus the character of the deformation. Therefore the vectorial dislocation velocity $\boldsymbol{v}$ meets

$$\frac{\mathrm{d}\boldsymbol{\varphi}}{\mathrm{d}t} = \boldsymbol{v} = v\boldsymbol{\nu}\,,\ \text{where}\ v = |\boldsymbol{v}|\,. \tag{2.28}$$

Glide sets in as soon as the effective force exceeds the resistance based on the yield stress[2] $\hat{\tau} > 0$, which is assumed to be positive, for details see section 2.4.5:

$$|T\kappa + b\tau| > b\hat{\tau}\,. \tag{2.29}$$

Equation (2.29) corresponds to the yield condition in constitutive models for continuum plasticity, see for example [4]. Where ever the yield condition does not hold the dislocation does not

[2] also denoted critical resolved shear stress, friction stress, slip system hardness or mechanical threshold

move, that is $v = 0$. For an advanced discussion on the physical meaning of the above yield condition see remark 2.1.

The motion induced by the resolved force acting on a dislocation can be described on arbitrary levels of abstraction. Quite a general dynamic theory of dislocations treats them as damped vibrating strings, endowed with an effective mass [79]. This leads to a non-linear correlation between the dislocation velocity and the effective stress, which however only needs to be considered for velocities close to the Rayleigh wave speed.

For the present considerations, a linearised relation is sufficient. Therefore, we abide by Ghoniem [80] who describes dislocation motion based on an associated viscous dissipation. For an isothermal process, the variation of the Gibbs free energy due to the viscous dissipation is

$$\delta W_{\mathrm{G}} = -\int_0^{\mathfrak{S}} B\boldsymbol{v} \cdot \delta\boldsymbol{\varphi} \,\mathrm{d}\mathfrak{s} \,. \tag{2.30}$$

This is reasonable if one assumes an fcc crystal and neglects interactions of the dislocations with localised obstacles. Then, the drag coefficient accounts for electron and phonon drag. In general, the drag coefficient B depends on ϑ, which accounts for the anisotropy of the glide mobility: screw segments are usually less mobile than edge segments. Within this thesis, B is presumed constant.

The principle of virtual work then provides the dynamic equilibrium of the energy variations:

$$\delta W_{\mathrm{F}} + \delta W_{\mathrm{S}} + \delta W_{\mathrm{G}} = 0 \,. \tag{2.31}$$

As the virtual displacement $\delta\boldsymbol{\varphi}$ was allowed to be arbitrary, the local form of the equilibrium of forces in normal direction to the dislocation line results as

$$Bv = \begin{cases} b(\tau - \hat{\tau}) + T\kappa & \text{if} \quad b\tau + T\kappa > b\hat{\tau} \\ 0 & \text{if} \quad |b\tau + T\kappa| \leq b\hat{\tau} \\ b(\tau + \hat{\tau}) + T\kappa & \text{if} \quad b\tau + T\kappa < -b\hat{\tau} \end{cases} , \tag{2.32}$$

where the yield condition (2.29) was considered. Note that the yield stress always counteracts the resolved shear stress.

The three cases of eq. (2.32) can also be written in the combined form

$$Bv = b\,\mathrm{sgn}(\tau)(|\tau| - \hat{\tau}) + T\kappa \quad \text{if} \quad |b\tau + T\kappa| > b\hat{\tau} \,. \tag{2.33}$$

For $B = 0$, that is in the case where no viscous drag force exists, the last equation corresponds to the equilibrium of forces for the rate-independent limit (2.23), enhanced only by the yield stress.

Remark 2.1: At first glance, the yield condition (2.29) is absolutely perspicuous: a single dislocation moves and deforms as well under an applied load τ as under its own line tension. In this sense, both forces are equal. But as the yield condition is used to describe the behaviour of a continuous distribution of dislocations, see the following section, the equality of both forces may loose validity. Imagine for example a straight dislocation in a thin crystalline strip, with its slip direction parallel to

the strip normal. In bending, the resolved shear stress acting on the dislocation in the centre of the strip is smaller than in the vicinity of its surface. So there might be a neutral zone around the neutral plane of the strip, where the yield stress $\hat{\tau}$ cannot be overcome by the effective shear stress alone ($|\tau| < \hat{\tau}$). In figure 2.3 two alternative conceptions of the response of dislocations to this loading case are depicted.

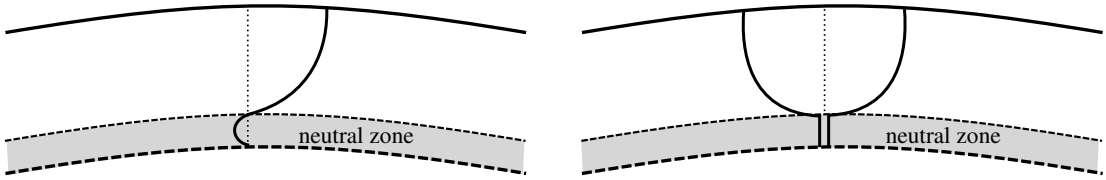

Figure 2.3: Illustration of the possibly different behaviour of a single dislocation (left) and two dislocations (representative of a continuum of dislocations, right) in the neutral zone in a bent thin crystalline strip. Note that only the upper half of the bent strip is shown.

An isolated dislocation is not able to have a non-vanishing curvature at the surface of the strip and to remain entirely straight in this neutral zone - it will bow out there under the effect of its line tension. This argument has been applied to a continuum description of dislocations by Zaiser [73], too. But one can also encounter, that in a group of dislocations, some of them positive, some of them negative, dipoles may form and equilibrate the transition from the neutral zone to the region where the yield condition is fulfilled ($|\tau| > \hat{\tau}$). In this way, the dislocations might arrive at remaining straight in the neutral zone. This agrees with the notion of continuum models that would not allow for plastic strain there, Sedláček [81, 82]. The force required to sustain the sharp curvature at the transition point between both zones would be raised by the high short-range stress in the dipole which is different from the mean field stress resulting from the continuum description of dislocations, and thus not a contradiction. Thus, in order to model such a situation, an alternative yield condition should be used:

$$|\tau| > \hat{\tau}\,. \tag{2.34}$$

2.3 Classical continuum theory of dislocations

The description of the motion of single dislocations has a large share in the set up of the continuum dislocation-based model. However, the transition to a continuum description of several dislocations is still lacking.

For almost 50 years, fields of dislocations have been described by continuum theories. One of the earliest approaches is due to Kröner [83], after whom is named the classical measure for a continuous distribution of dislocations, Kröner's dislocation density tensor $\boldsymbol{\alpha}$. We want to provide a better understanding for the issues that have motivated the actual method of single-valued

dislocation fields that is used in the present continuum model, section 2.4. This section therefore provides a short excursion to the basic principles and drawbacks of the classical continuum theory of static and moving dislocations.

2.3.1 Kröner's dislocation density tensor

Based on the description of single dislocations, that has been thoroughly discussed in the preceding sections, a first definition of Kröner's dislocation density tensor can be given.
Provided a distribution of individual dislocations, each described by its Burgers vector $\boldsymbol{b}^{(i)}$ and line direction $\boldsymbol{\xi}^{(i)}$, the dislocation density tensor is defined as:

$$\boldsymbol{\alpha} = \frac{1}{\Delta V} \sum_i \boldsymbol{b}^{(i)} \otimes \boldsymbol{\xi}^{(i)} \, \mathrm{d}\mathfrak{s}^{(i)} \,, \tag{2.35}$$

where $\mathrm{d}\mathfrak{s}^{(i)}(\boldsymbol{x})$ are the lengths of the individual dislocation segments that are present in a certain volume element ΔV positioned at $\boldsymbol{x}$, for details see section 2.1. As usual for second order tensors, the matrix representation of $\boldsymbol{\alpha}$ depends on the chosen coordinate system.
The dislocation density tensor $\boldsymbol{\alpha}$ and the scalar dislocation density ϱ commonly used in the materials science,

$$\varrho = \frac{1}{\Delta V} \sum_i \mathrm{d}\mathfrak{s}^{(i)} \,, \quad \text{total length of dislocation lines per volume,} \tag{2.36}$$

are correlated if and only if there are dislocations of only one orientation $\boldsymbol{\xi}$ and one Burgers vector $\boldsymbol{b}$ in the considered volume, see also remark 2.2. Then it is valid:

$$\boldsymbol{\alpha} = \boldsymbol{b} \otimes \varrho \boldsymbol{\xi} \,. \tag{2.37}$$

A second definition of $\boldsymbol{\alpha}$ is based upon the notion of *(in-)compatibility*.

(In-)compatibility of elasto-plastic deformation

To give this definition, we need to introduce some elements of the small-strain continuum mechanics, which will be required later in this thesis, too.
Consider a small volume $\Delta V := \Delta x_1 \Delta x_2 \Delta x_3$ of a crystal. Let $\boldsymbol{u}(\boldsymbol{x})$ denote the displacement field. The geometric situation of the deformed volume element is described by the distortion tensor $\boldsymbol{\beta} = \beta_{ij}$ $(i, j = 1, 2, 3)$. The distortion can be introduced both as

$$\boldsymbol{\beta} \, \mathrm{d}\boldsymbol{x} = \mathrm{d}\boldsymbol{u} \,, \tag{2.38}$$

which is generally valid, or as

$$\boldsymbol{\beta} = \nabla \boldsymbol{u} \,, \tag{2.39}$$

which is true only in case of a compatible elasto-plastic distortion. A compatible distortion is the result of a deformation which transforms a compact body into another compact, that is connected,

body. An incompatible distortion is the result of a deformation which transforms a compact body into a non-fitting collection of small elements (or just the other way around). For a more detailed explanation of (in-)compatibility the reader is referred to Kröner [84].
From the mathematical point of view, the distortion is compatible if it has a primitive, that is if a continuous function $\boldsymbol{u}$ exists such that $\nabla \boldsymbol{u} = \boldsymbol{\beta}$. This is true if the integrability condition, see for example [85], holds: a primitive for $\boldsymbol{\beta}$ exists if $\operatorname{curl} \boldsymbol{\beta} = 0$.

The distortion $\boldsymbol{\beta}$ is an asymmetric tensor, which, in the linear theory[3], can be additively decomposed into a symmetric part $\boldsymbol{\epsilon}$ and an antisymmetric part $\boldsymbol{\omega}$:

$$\boldsymbol{\beta} = \boldsymbol{\epsilon} + \boldsymbol{\omega}\,, \qquad \text{where } \boldsymbol{\epsilon} = \frac{1}{2}(\boldsymbol{\beta} + \boldsymbol{\beta}^{\mathrm{T}}) = \boldsymbol{\epsilon}^{\mathrm{T}}\,,\ \boldsymbol{\omega} = \frac{1}{2}(\boldsymbol{\beta} - \boldsymbol{\beta}^{\mathrm{T}}) = -\boldsymbol{\omega}^{\mathrm{T}}\,. \tag{2.40}$$

$\boldsymbol{\epsilon}$ is the tensor of material strain, $\boldsymbol{\omega}$ is the material rotation. For a general elasto-plastic deformation within the small-strain framework, the distortion tensor can be linearly decomposed into an elastic and a plastic part,

$$\boldsymbol{\beta} = \boldsymbol{\beta}^{\mathrm{e}} + \boldsymbol{\beta}^{\mathrm{p}}\,. \tag{2.41}$$

Each of the parts can again be decomposed into a strain and a rotation tensor,

$$\boldsymbol{\beta}^{\mathrm{e}} = \boldsymbol{\epsilon}^{\mathrm{e}} + \boldsymbol{\omega}^{\mathrm{e}}\,, \qquad \boldsymbol{\beta}^{\mathrm{p}} = \boldsymbol{\epsilon}^{\mathrm{p}} + \boldsymbol{\omega}^{\mathrm{p}}\,. \tag{2.42}$$

The elastic strain tensor $\boldsymbol{\epsilon}^{\mathrm{e}}$ describes a change of the shape of ΔV and the corresponding strain of the lattice. The elastic rotation tensor $\boldsymbol{\omega}^{\mathrm{e}}$ describes a rigid rotation of the element whereby the lattice structure, too, is rigidly rotated through the same angle. The plastic counterparts only describe a straining/rotation of the material, while the lattice structure and orientation are not affected by a purely plastic deformation, see again [84].
In the continuum theory of dislocations, one assumes the distortion to be compatible, i.e. $\operatorname{curl} \boldsymbol{\beta} = 0$, but this needs not hold for its elastic and plastic part when considered separately, i.e. in general $\operatorname{curl} \boldsymbol{\beta}^{\mathrm{e/p}} \neq 0$. So $\operatorname{curl} \boldsymbol{\beta}^{\mathrm{e/p}}$ can be interpreted as a measure for the incompatibility of a deformation.
From the physical viewpoint, an incompatible deformation is counteracted by the formation of (geometrically necessary) dislocations. It is up to these line defects to compensate the misfit between incompatibly deformed small volume elements: the bigger the incompatibility of a deformation, the larger is the required number of dislocations in the material.
These two statements motivate the second definition for the dislocation density tensor $\boldsymbol{\alpha}$ which we would like to specify[4],

$$\boldsymbol{\alpha} = \operatorname{curl} \boldsymbol{\beta}^{\mathrm{e}}\,. \tag{2.43}$$

[3] that is equivalent to the theory of small strains
[4] One can also find the opposite sign convention, that is $\boldsymbol{\alpha} = -\operatorname{curl} \boldsymbol{\beta}^{\mathrm{e}} = \operatorname{curl} \boldsymbol{\beta}^{\mathrm{p}}$, e.g. in [84].

As the total distortion $\boldsymbol{\beta}$, also denoted material distortion, is supposed to be compatible, we find from the identity (B.3) and the linear decomposition (2.41):

$$\boldsymbol{\alpha} = -\operatorname{curl} \boldsymbol{\beta}^{\mathrm{p}} \,. \tag{2.44}$$

Equation (2.43), also known as the *first order (in-)compatibility law*, is a fundamental field equation of the linear continuum theory of dislocations. It expresses, that a continuum can be in a state of incompatible elastic distortion provided there exists a tensor field $\boldsymbol{\alpha}$ which guarantees the compatibility of the material distortion. In this sense, it becomes clear, that $\boldsymbol{\alpha}$ defined like that is a tensor describing in some sense the dislocation density in the material.

For the sake of completeness, let us finally discuss the continuum relation between the dislocation density tensor $\boldsymbol{\alpha}$ and Burgers vector $\boldsymbol{b}$. In the standard theory of dislocations, see for example Hirth & Lothe [86], the Burgers vector for a single dislocation is defined as

$$\boldsymbol{b} = \oint_C \boldsymbol{\beta}^{\mathrm{e}} \, \mathrm{d}\boldsymbol{l} \,, \tag{2.45}$$

where the line integral is to be taken in the right handed sense with respect to the tangent vector $\boldsymbol{\xi}$ to the dislocation line. $\mathrm{d}\boldsymbol{l}$ is an oriented element of the closed boundary C of an area A

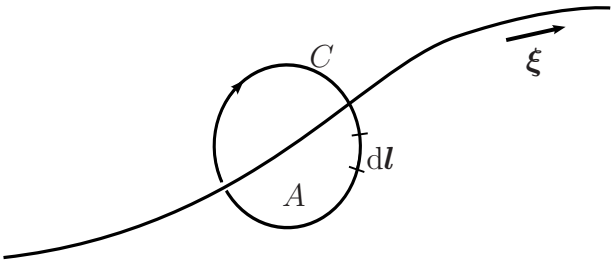

Figure 2.4: Considered scenario for the continuum definition of Burgers vector.

through which the dislocation is piercing, figure 2.4, and $\boldsymbol{\beta}^{\mathrm{e}}$ is the elastic distortion caused by the dislocation.
In the case of continuously distributed dislocations and by applying eqs. (2.43) and (B.10$_2$), eq. (2.45) transforms to

$$\boldsymbol{b} = \int_A \boldsymbol{\alpha} \, \mathrm{d}\boldsymbol{a} \,. \tag{2.46}$$

Here $\boldsymbol{b}$ is the resulting Burgers vector of all the (continuously distributed) dislocations piercing through A. The differential representation of eq. (2.46) is

$$\mathrm{d}\boldsymbol{b} = \boldsymbol{\alpha} \, \mathrm{d}\boldsymbol{a} \,, \tag{2.47}$$

where $\mathrm{d}\boldsymbol{b}$ is the resulting Burgers vector of all the continuously distributed dislocations piercing through the infinitesimal area $\mathrm{d}\boldsymbol{a}$.

From the definition of $\boldsymbol{\alpha}$ in eq. (2.43) and the identity (B.4) we find the fundamental equation

$$\operatorname{div} \boldsymbol{\alpha} = 0 \,, \tag{2.48}$$

which expresses the fact, that dislocations cannot end within the crystal.

Remark 2.2: The average over the actually present dislocations in a crystal, that is the content of the dislocation density tensor $\boldsymbol{\alpha}$, is actually a measure for the *geometrically necessary dislocations* (GNDs). This term was primarily used by Cottrell [87] to describe the dislocations which have to exist due to mesoscopic gradients of the plastic deformation, section 1.3. The further development of the concept of GNDs is often ascribed to Ashby, see [88]. It is generally accepted that the GNDs can give rise to size effects [11]. The other population of dislocations in a crystal besides the GNDs are the *statistically stored dislocations* (SSD): they are independent of the deformation state, that is the microstructure, but are randomly introduced and distributed in the material. GNDs constitute additional obstacles hampering the glide of the dislocations, thus yielding additional hardening. The total scalar dislocation density is, in good approximation [88], the sum of both. In general, one cannot decide whether an individual dislocation belongs to either the first or the second kind of dislocations. Moreover, the definition of GNDs depends on the considered scale: in a sufficiently small-scaled continuum theory of dislocations, that would even be able to resolve the inter-dislocation spacing, all dislocations would be classified as geometrically necessary, and thus be represented by the dislocation density tensor $\boldsymbol{\alpha}$.

2.3.2 Moving dislocations

Considering moving dislocations, we have to treat all the defined fields as functions of position and time. As we are working in the framework of the geometrically linear theory, an exchange of the differentiation order ($\partial/\partial\boldsymbol{x} \leftrightarrow \partial/\partial t$) is no problem. The material distortion rate is defined as gradient of the material velocity:

$$\boldsymbol{L} = \operatorname{grad}\left(\frac{\partial u(\boldsymbol{x},t)}{\partial t}\right) = \frac{\partial \boldsymbol{\beta}}{\partial t}\,. \tag{2.49}$$

Continuity of the material deformation entails the correlation

$$\operatorname{curl}\boldsymbol{L} = 0\,. \tag{2.50}$$

The linear decomposition into plastic and elastic parts is not influenced by the time derivative, thus

$$\boldsymbol{L} = \boldsymbol{L}^{\mathrm{p}} + \boldsymbol{L}^{\mathrm{e}} := \frac{\partial \boldsymbol{\beta}^{\mathrm{p}}}{\partial t} + \frac{\partial \boldsymbol{\beta}^{\mathrm{e}}}{\partial t}\,. \tag{2.51}$$

A density consideration of continuously distributed dislocations as in eq. (2.43) is also possible for moving dislocations. But for the dynamic case, it is not trivial to define the material distortion rate, as it should essentially depend on the dislocation motion. Mura [89–92] for example starts his derivation with the time derivative of the definition equation for the Burgers vector (2.46),

$$\frac{\partial \boldsymbol{b}}{\partial t} = \int_A \frac{\partial \boldsymbol{\alpha}}{\partial t}\,\mathrm{d}\boldsymbol{a}\,, \tag{2.52}$$

which determines the rate of change of the Burgers vector resulting from the continuously distributed dislocations piercing through A, compare figure 2.4. This change is supposed to be due to the dislocations flowing across the boundary C of the considered area, figure 2.5.

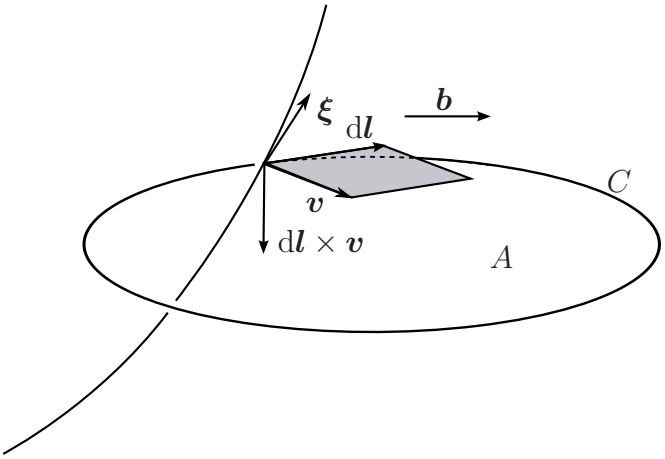

Figure 2.5: A dislocation flowing with velocity $\boldsymbol{v}$ across the boundary C into the area A. It makes a contribution to the total Burgers vector for the area A.

Considering a uniform dislocation population, that means all associated dislocations share a common Burgers vector and line direction, Mura defines the rate of plastic distortion as

$$\frac{\partial \boldsymbol{\beta}^{\mathrm{p}}}{\partial t} = \boldsymbol{b} \otimes \varrho \boldsymbol{\xi} \times \boldsymbol{v} \,. \tag{2.53}$$

A number of elementary considerations and transformations yield

$$\frac{\partial \boldsymbol{b}}{\partial t} = -\int_A \operatorname{curl} (\boldsymbol{b} \otimes \varrho \boldsymbol{\xi} \times \boldsymbol{v}) \, \mathrm{d}\boldsymbol{a} \,, \tag{2.54}$$

for details see Sedláček [8]. So the fundamental field equation of the linear continuum theory of moving dislocations results as

$$\frac{\partial \boldsymbol{\alpha}}{\partial t} = -\operatorname{curl} \frac{\partial \boldsymbol{\beta}^{\mathrm{p}}}{\partial t} \,. \tag{2.55}$$

2.3.3 The problem of averaging

As was demonstrated, the classical continuum theory of dislocations is significantly based on Kröners dislocation density tensor. But for the development of a model that describes the plastic deformation at the μm-scale it is not a proper measure. Assume a volume ΔV that contains two populations of dislocations of opposite sign, but equal scalar density. Then, the total scalar density ϱ will be just the sum of the densities of both groups, while the dislocation density tensor $\boldsymbol{\alpha}$ will vanish, eq. (2.35). It is therefore important to be clear in one's mind that in general $\boldsymbol{\alpha}$ does not describe the line directions and Burgers vectors of the real crystal dislocations, but only of their average. Figure 2.6 gives another exemplification of this fact.

For a continuum description of moving dislocations, a dislocation velocity tensor of the form $\boldsymbol{\alpha} \otimes \boldsymbol{v}$ can be formally derived from Kröner's dislocation density tensor. However such a tensor would not be able to correctly provide the plastic slip rate: the average character of $\boldsymbol{\alpha}$ propagates into the dislocation velocity tensor. Imagine a volume element containing the same number of dislocations of Burgers vector $\boldsymbol{b}$ oriented along $\boldsymbol{\xi}$ and $-\boldsymbol{\xi}$. For the considered volume element, the dislocation velocity tensor vanishes, leading to a vanishing plastic slip rate. In reality, the

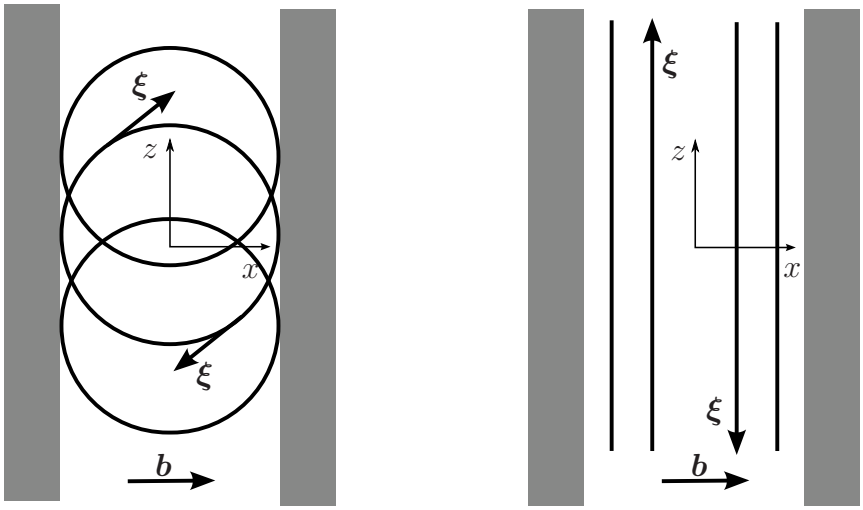

Figure 2.6: Consider a confined channel, infinitely extended in z direction, on the mesoscale, see also [70]. Left: circular dislocation loops, representative of the continuous distribution of loops that cause the deformation. The calculated dislocation density tensor is the same as for the dislocation distribution on the right: representative straight edge dislocations aligned with the z-axis in pile-up configurations. They constitute the 'share' of geometrically necessary dislocations of the dislocation ensemble on the left, see remark 2.2.

Peach-Koehler forces acting on the two antiparallel dislocation populations in a given stress field point in opposite directions, such that a non-vanishing slip rate results.
In the following section the concept of single-valued dislocation fields is introduced, which provides a basis for the continuum-dislocation based model that is not afflicted with these averaging problems.

2.4 Single-valued dislocation fields

In contrast to a multiple-valued field, in a single-valued field of dislocations all field variables, like for example the line direction $\boldsymbol{\xi}$ or the orientation ϑ, have a unique value at a position $\boldsymbol{x}$ at time t. Such a population can for example be the result of the operation of a single Frank-Read source. It is assumed that in many cases of practical interest a real dislocation configuration can be approximated by a superposition of smooth[5] single-valued dislocation fields. As an example consider again the field of dislocation loops expanding in a channel, figure 2.6. It cannot be described as a single-valued field: at positions where two loops intersect, there exist two different orientations / line directions. However, this situation can be split into two single-valued fields, namely that of the lower half-loops, and that of the upper half-loops. Such a separation will be used in the applications presented later on, too.

In the following, all considerations are made in the extended slip plane coordinate system intro-

[5] With respect to the curve representation, section 2.1, at least $\mathcal{C}^2$ continuity of the mapping $\boldsymbol{\varphi}$ is required.

duced in eq. (2.2):

$$\boldsymbol{e}_x = \boldsymbol{s}\,,\ \boldsymbol{e}_y = \boldsymbol{n}\times\boldsymbol{s}\,,\ \boldsymbol{e}_z = \boldsymbol{n}\,. \tag{2.56}$$

Thus unit tangent and unit normal to the dislocation line are expressed as

$$\boldsymbol{\xi} = \begin{pmatrix}\cos\vartheta\\ \sin\vartheta\\ 0\end{pmatrix}\,,\ \boldsymbol{\nu} = \begin{pmatrix}-\sin\vartheta\\ \cos\vartheta\\ 0\end{pmatrix}\,. \tag{2.57}$$

Applying some standard mathematical conversions, a number of very useful relations between $\boldsymbol{\xi}, \boldsymbol{\nu}$ and ϑ can be found. They are collected in appendix C.

Equation (2.12) is an expression for the curvature of a single dislocation which is given in natural parametrisation:

$$\kappa\boldsymbol{\nu} = \frac{\mathrm{d}\boldsymbol{\xi}}{\mathrm{d}\mathfrak{s}}\,. \tag{2.58}$$

This is still valid for every dislocation in the considered single-valued dislocation field. In [8], the fact that the line element $\mathrm{d}\mathfrak{s}$ is an element in direction $\boldsymbol{\xi}$ was interpreted in the sense that in the present context $\mathrm{d}/\mathrm{d}\mathfrak{s}\hat{=}\nabla_{\boldsymbol{\xi}}$. Using eqs. (C.5$_1$), (B.9) and (C.4$_2$), equation (2.58) can then be transformed as follows:

$$\kappa\boldsymbol{\nu} = \nabla_{\boldsymbol{\xi}}\boldsymbol{\xi} = (\operatorname{grad}\boldsymbol{\xi})\cdot\boldsymbol{\xi} = (\boldsymbol{\nu}\otimes\operatorname{grad}\vartheta)\boldsymbol{\xi} = \boldsymbol{\nu}(\operatorname{grad}\vartheta\cdot\boldsymbol{\xi}) = -\boldsymbol{\nu}\operatorname{div}\boldsymbol{\nu}\,, \tag{2.59}$$

thus providing a direct equation for the curvature of the field of dislocations:

$$\kappa = -\operatorname{div}\boldsymbol{\nu}\,. \tag{2.60}$$

The relation $\mathrm{d}/\mathrm{d}\mathfrak{s}\hat{=}\nabla_{\boldsymbol{\xi}}$ is however not readily obvious, so we dedicate a few lines to its elucidation. For the gradient / divergence operations in the above equations to make sense, the variables to which they are applied have to be defined as functions of (x, y). As the considered variables are defined along the dislocation curve only, x and y are not independent. Actually they must be understood in the sense $(x, y)\hat{=}(\varphi_x(\mathfrak{s}), \varphi_y(\mathfrak{s}))$. For an accordingly defined variable, say for example $\vartheta\big(\varphi_x(\mathfrak{s}), \varphi_y(\mathfrak{s})\big)$, we find in compliance with the concept of the total differential

$$\frac{\mathrm{d}\vartheta}{\mathrm{d}\mathfrak{s}} = \frac{\partial\vartheta}{\partial\varphi_x}\frac{\mathrm{d}\varphi_x}{\mathrm{d}\mathfrak{s}} + \frac{\partial\vartheta}{\partial\varphi_y}\frac{\mathrm{d}\varphi_y}{\mathrm{d}\mathfrak{s}} = \nabla\vartheta\cdot\boldsymbol{\xi} = \nabla_{\boldsymbol{\xi}}\vartheta\,. \tag{2.61}$$

Considering fields of curves / dislocations, the relation $\kappa := \nabla_{\boldsymbol{\xi}}\vartheta$ will be used.

Some of the presentations in this section are only true for the one-dimensional case, that is where for example the shape of a representative dislocation can be described as a function $\varphi_y(x)$ depending on the slip direction coordinate only. The mapping $\boldsymbol{\varphi}$ can then be defined as $\boldsymbol{\varphi} = (x, \varphi_y(x))$.

2.4.1 An annotation to the physical meaning of Eulerian and Lagrangian description

In the following subsections, the evolution equations for dislocation density and orientation of the considered single-valued field will be derived. Two representations will be given, the Eulerian and the Lagrangian description. In order to get a feeling on the essential difference between both approaches, a brief excursion on the physical meaning of the Eulerian and Lagrangian view is prepended. It is important to note, that this distinction only refers to the dislocation continuum. In fact we are facing two continua: that of the material, which is always described in the Eulerian way, and that of the continuously distributed dislocations. To emphasise this, sometimes the term 'dislocation-Lagrangian' is used, but it is to be understood as equivalent to 'Lagrangian'.
If one wants to describe the temporal evolution of a representative dislocation line there are two possible approaches, see also figure 2.7.

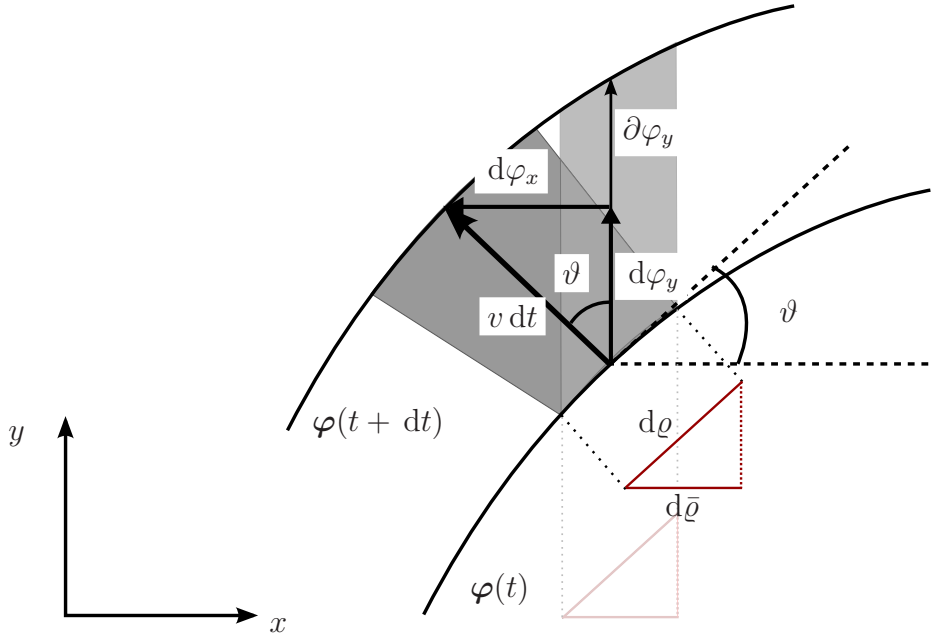

Figure 2.7: Eulerian and Lagrangian description of the evolution of a dislocation line. The light gray area is passed by the dislocation segment of initial dislocation density $\mathrm{d}\bar{\varrho}$ in the time interval $\mathrm{d}t$, if considered from the Eulerian point of view. The same segment considered the Lagrangian way due to the bowing out corresponds to a dislocation density $\mathrm{d}\varrho$, and passes the dark gray area in the time interval $\mathrm{d}t$. Note that the vector related to the Eulerian increment $\partial\varphi_y$ spans the entire offset of the two curves.

Eulerian description 'Sit down' on a fixed position x, and watch in direction y, how the part of the dislocation line, which is in front of you, moves away (i.e. how φ_y grows). Note that due to the way dislocations move, namely always perpendicular to the dislocation line, we still observe changing segments. In terms of the mapping $\boldsymbol{\varphi}$, we find

$$\boldsymbol{\varphi} = (x, \varphi_y(x,t), 0)^{\mathrm{T}} \ , \tag{2.62}$$

and describe its evolution in terms of the Eulerian derivative $\partial/\partial t$:

$$\frac{\partial \boldsymbol{\varphi}}{\partial t} = \left(0, \frac{\partial \varphi_y}{\partial t}, 0\right)^{\mathrm{T}} . \tag{2.63}$$

Lagrangian description 'Sit down' on a segment X of the dislocation line[6], imagine it as a virtual particle, and watch where it goes. The direction of motion is always perpendicular to the dislocation line, and thus the x-position of the segment in the coordinate system of the slip system permanently changes and has to be tracked, too. Note that due to the bowing out of the dislocation the considered segment also changes its length. In the Lagrangian description the position of a particle X at time t is again given by the mapping $\boldsymbol{\varphi}$, which here results as:

$$\boldsymbol{\varphi}(X,t) = (\boldsymbol{\varphi}_x(X,t), \boldsymbol{\varphi}_y(X,t), 0)^{\mathrm{T}} . \tag{2.64}$$

The evolution of the dislocation segment is due to the velocity of the dislocation field at its current position $\boldsymbol{x} \mathrel{\hat{=}} \boldsymbol{\varphi}$, which corresponds to the Lagrangian derivative $\mathrm{d}/\,\mathrm{d}t$ of the mapping $\boldsymbol{\varphi}$, respectively:

$$\frac{\mathrm{d}\boldsymbol{\varphi}(X,t)}{\mathrm{d}t} = \boldsymbol{v}(\boldsymbol{x},t) = v(\boldsymbol{x},t)\boldsymbol{\nu}(\boldsymbol{x},t) . \tag{2.65}$$

A relation between both descriptions (Eulerian and Lagrangian) can be established analytically on the basis of differential calculus:

$$\begin{aligned} \frac{\mathrm{d}\varphi_y}{\mathrm{d}t} &= \frac{\partial \varphi_y}{\partial t} + \frac{\partial \varphi_y}{\partial X}\frac{\mathrm{d}X}{\mathrm{d}t} \mathrel{\hat{=}} \frac{\partial \varphi_y}{\partial t} + \frac{\partial \varphi_y}{\partial x}\frac{\mathrm{d}\varphi_x}{\mathrm{d}t} \\ \rightarrow \quad \frac{\partial \varphi_y}{\partial t} &= v\ \cos\vartheta - \underbrace{\tan\vartheta}_{\substack{\text{gradient to} \\ \varphi_y(x)}}(-v\ \sin\vartheta) = \frac{v}{\cos\vartheta} . \end{aligned} \tag{2.66}$$

We can find the same relation graphically in view of figure 2.7, where we interpret the vectors representing the increments $\partial\varphi_y$ etc. as vectors indicating the respective time derivative, $\partial\varphi_y/\partial t$ etc.:

$$\frac{\partial \varphi_y}{\partial t} = \frac{\mathrm{d}\varphi_y}{\mathrm{d}t} + \tan\vartheta\frac{\mathrm{d}\varphi_x}{\mathrm{d}t} = v\ \cos\vartheta + \tan\vartheta\,(v\ \sin\vartheta) = \frac{v}{\cos\vartheta}. \tag{2.67}$$

2.4.2 Evolution of dislocation density and orientation - Eulerian description

Consider now a single-valued dislocation field, defined by a density field $\varrho(\boldsymbol{x},t)$ and the orientation $\vartheta(\boldsymbol{x},t)$ of a representative dislocation line. Combining eqs. (2.37) and (2.48) and using the

[6] X can be interpreted as the initial/reference x-position of the considered particle.

conservation of Burgers vector along dislocation lines, we end up with the solenoidality condition

$$\operatorname{div} \boldsymbol{\varrho} := \operatorname{div} \varrho\boldsymbol{\xi} = 0\,. \tag{2.68}$$

It expresses that dislocations cannot begin or end within the crystal, which is a necessary compatibility condition for all dislocation fields. Resolved in component notation, this corresponds to

$$\frac{\partial(\varrho\cos\vartheta)}{\partial x} + \frac{\partial(\varrho\sin\vartheta)}{\partial y} = 0\,. \tag{2.69}$$

Thus a coupling between the scalar dislocation density ϱ and the dislocation orientation ϑ exists. To find an evolution equation for the scalar density ϱ and the orientation ϑ, we use the fundamental field equation for moving dislocations (2.55). Combining it with eq. (2.37), Orowan's equation (1.4) and the fundamental equation of crystal plasticity (1.1), and using the constancy of Burgers vector, it can be simplified to

$$\frac{\partial\boldsymbol{\varrho}}{\partial t} + \operatorname{curl}(\varrho v\boldsymbol{n}) = 0\,. \tag{2.70}$$

This is an evolution equation for the 'vectorial' dislocation density $\boldsymbol{\varrho} = \varrho\boldsymbol{\xi}$. In view of identity (B.5) and noting that $\boldsymbol{n}$ is constant, i.e. $\operatorname{curl}\boldsymbol{n} = 0$, it can be further simplified to

$$\frac{\partial\boldsymbol{\varrho}}{\partial t} + \operatorname{grad}(\varrho v)\times\boldsymbol{n} = 0\,. \tag{2.71}$$

On the component level this is a system of two equations for the evolution of the scalar dislocation density $\varrho(\boldsymbol{x},t)$ and the orientation $\vartheta(\boldsymbol{x},t)$:

$$\frac{\partial(\varrho\cos\vartheta)}{\partial t} = -\frac{\partial(\varrho v)}{\partial y}\,, \tag{2.72$_1$}$$

$$\frac{\partial(\varrho\sin\vartheta)}{\partial t} = \frac{\partial(\varrho v)}{\partial x}\,, \tag{2.72$_2$}$$

which yields the evolution equations

$$\frac{\partial\varrho}{\partial t} = \frac{\partial(\varrho v)}{\partial x}\sin\vartheta - \frac{\partial(\varrho v)}{\partial y}\cos\vartheta = -\nabla_{\boldsymbol{\nu}}(\varrho v) = -\frac{1}{b}\nabla_{\boldsymbol{\nu}}\dot{\gamma}^{\mathrm{p}}\,, \tag{2.73$_1$}$$

$$\varrho\frac{\partial\vartheta}{\partial t} = \frac{\partial(\varrho v)}{\partial x}\cos\vartheta + \frac{\partial(\varrho v)}{\partial y}\sin\vartheta = \nabla_{\boldsymbol{\xi}}(\varrho v) = \frac{1}{b}\nabla_{\boldsymbol{\xi}}\dot{\gamma}^{\mathrm{p}}\,, \tag{2.73$_2$}$$

where the last conversion is due to Orowan's equation (1.4). This shows, that the evolution of the scalar dislocation density is determined by the derivative of the plastic slip rate in the direction perpendicular to the dislocation lines, while the evolution of the orientation depends on the derivative of the plastic slip rate in tangential direction to them. Identity (B.6) provides the relation

$$\operatorname{div}(\varrho\boldsymbol{v}) = \varrho v\operatorname{div}\boldsymbol{\nu} + \operatorname{grad}(\varrho v)\cdot\boldsymbol{\nu}\,, \tag{2.74}$$

which together with eq. (2.60) enables one to recast the evolution equation (2.73_1) in the form of an Eulerian continuity equation

$$\frac{\partial \varrho}{\partial t} + \operatorname{div}(\varrho \boldsymbol{v}) = -\varrho v \kappa \,. \tag{2.75}$$

The right hand side of this equation can be interpreted as a source term for the dislocation density. It is equal to zero for straight dislocations ($\kappa = 0$). However, curved dislocations do not just translate by moving, but they expand (or shrink) changing their length so that the continuity of the curved dislocation is guaranteed, i.e. the compatibility condition (2.68) is fulfilled. Together with an initial value $\bar{\varrho}(\boldsymbol{x}) = \varrho(\boldsymbol{x}, t = 0)$, the dislocation density is defined for all times t.
An explicit evolution equation for the orientation ϑ can be derived by eliminating the dependence on ϱ in eq. (2.73_2). Identity (B.6) applied to the continuity equation (2.68) provides

$$\varrho \operatorname{div} \boldsymbol{\xi} + \operatorname{grad} \varrho \cdot \boldsymbol{\xi} = 0 \quad \overset{\cdot v}{\Longrightarrow} \quad v\varrho \operatorname{div} \boldsymbol{\xi} + (\operatorname{grad}(\varrho v) - \varrho \operatorname{grad} v) \cdot \boldsymbol{\xi} = 0 \,, \tag{2.76}$$

where the product rule eq. (B.7) was used. Thus we end up with the evolution equation for the orientation in the form

$$\frac{\partial \vartheta}{\partial t} = \operatorname{grad} v \cdot \boldsymbol{\xi} - v \operatorname{div} \boldsymbol{\xi} \,. \tag{2.77}$$

2.4.3 Evolution of dislocation density and orientation - Lagrangian description

In general, for a scalar field $a(\boldsymbol{x}, t)$ the Lagrangian (total) time derivative $\mathrm{d}/\mathrm{d}t$ is related to the Eulerian (partial) time derivative $\partial/\partial t$ through a (particle-) velocity $\boldsymbol{v}$.

$$\frac{\mathrm{d}a}{\mathrm{d}t} = \frac{\partial a}{\partial t} + \operatorname{grad} a \cdot \boldsymbol{v} \,. \tag{2.78}$$

For a vector field $\boldsymbol{u}(\boldsymbol{x}, t)$ the corresponding relation is

$$\frac{\mathrm{d}\boldsymbol{u}}{\mathrm{d}t} = \frac{\partial \boldsymbol{u}}{\partial t} + (\operatorname{grad} \boldsymbol{u})\boldsymbol{v} \,. \tag{2.79}$$

The Eulerian evolution equations for the scalar dislocation density (2.73_1) and orientation (2.77) thus find their Lagrangian counterpart in

$$\frac{\mathrm{d}\varrho}{\mathrm{d}t} = -\varrho \operatorname{grad} v \cdot \boldsymbol{\nu} = -\varrho \nabla_{\boldsymbol{\nu}} v \,, \tag{2.80_1}$$

$$\frac{\mathrm{d}\vartheta}{\mathrm{d}t} = \operatorname{grad} v \cdot \boldsymbol{\xi} = \nabla_{\boldsymbol{\xi}} v \,. \tag{2.80_2}$$

The Lagrangian form of the continuity equation (2.75) reads

$$\frac{\mathrm{d}\varrho}{\mathrm{d}t} + \varrho \operatorname{div} \boldsymbol{v} = -\varrho v \kappa \,. \tag{2.81}$$

Equation (2.80_1) represents the net rate of change of the scalar density due to the difference in the velocity of dislocation segments flowing across the boundaries of the considered volume element. Since the velocity of a dislocation segment is perpendicular to the dislocation line direction, only

the boundaries parallel to dislocation lines make a contribution, i.e. the derivative results in the direction $\boldsymbol{\nu}$.
Equation (2.80_2) shows that the net rate of change of the local orientation of dislocations gliding with the velocity of magnitude v depends on the gradient of the velocity magnitude along the dislocation lines. It is the rate of rotation of an infinitesimal dislocation segment of orientation $\vartheta(\boldsymbol{x}, t)$ caused by the difference of the velocities of its end points.

2.4.4 Formal determination of the plastic slip

One direction of the coupling of the description of single-valued dislocation fields to continuum mechanics is accomplished via the plastic slip γ^{p}, figure 2.8. In this paragraph the concept of plastic slip is formally introduced.
Consider a dislocation segment of length $V\,\mathrm{d}\bar{\varrho}$ contained in the volume V. In the time interval $\mathrm{d}t$, the segment shears off the area $\partial\varphi_y(V\,\mathrm{d}\bar{\varrho})$, see also figure 2.7. This causes a shear strain per volume equal to the magnitude of Burgers vector times the sheared area per volume, that is $b\,\partial\varphi_y\,\mathrm{d}\bar{\varrho}$. The differential shear of first order, corresponding to the plastic slip rate that is caused by the dislocations of a single valued dislocation field, is obtained from the integration over all associated dislocation segments,

$$\partial\gamma^{\mathrm{p}} = b\,\partial\varphi_y \int \mathrm{d}\bar{\varrho} = b\bar{\varrho}\partial\varphi_y\,. \tag{2.82}$$

In the presented framework, the plastic slip can thus be expressed in terms of the set-off of a representative dislocation from its initial configuration[7]. This is given by the y-component of the position vector, $\varphi_y(\boldsymbol{x}, t)$. The plastic slip then results as

$$\gamma^{\mathrm{p}} = b\bar{\varrho}\varphi_y\,. \tag{2.83}$$

As a consequence, the evolution equations for the plastic slip in the Eulerian and the Lagrangian case result as

$$\frac{\partial\gamma^{\mathrm{p}}}{\partial t} = b\bar{\varrho}\frac{\partial\varphi_y}{\partial t} = b\bar{\varrho}\frac{v}{\cos\vartheta}\,, \tag{2.84_1}$$

$$\frac{\mathrm{d}\gamma^{\mathrm{p}}}{\mathrm{d}t} = b\bar{\varrho}\,\frac{\mathrm{d}\varphi_y}{\mathrm{d}t} = b\bar{\varrho}v\cos\vartheta\,. \tag{2.84_2}$$

Remark 2.3: For the simplifying assumptions which will be introduced in chapter 3, the Eulerian evolution equation directly yields Orowan's equation (1.4)

$$\frac{\partial\gamma^{\mathrm{p}}}{\partial t} = b\frac{\bar{\varrho}}{\cos\vartheta}v = b\varrho v\,. \tag{2.85}$$

Here $\varrho = \bar{\varrho}/\cos\vartheta$ was used, which is true especially for initially straight dislocations, eq. (3.6).

[7] In the presented applications the straight line at position $y = 0$ is used as initial dislocation configuration.

2.4.5 Closure of the system of equations and coupling to mechanics

The theory that has been presented in this section applies to a single-valued dislocation field and one slip system. The treatment of multiple-valued fields requires some extra effort and will be addressed in section 2.5. However, the consideration of several slip systems, each populated by a single-valued field, can be accomplished in a straightforward way, cf. eq. (1.2). The evolution of the scalar fields $\vartheta^{(i)}$ and $\varrho^{(i)}$ on each slip system, labeled by i, is determined by the respective dislocation velocity field. Provided a current state of a representative dislocation, from which the curvature $\kappa^{(i)}$ can be found according to eq. (2.60), the velocity is determined by the equation of motion (2.32). Remember that the resolved shear stress is given as a projection of the macroscopic stress field according to eq. (1.3), which results in general in a different value $\tau^{(i)}$ for each of the considered slip systems. So the evolution of the individual fields has to be calculated separately for each slip system.

In the calculation of the yield stress $\hat{\tau}$ and the coupling to the continuum mechanics framework is where the variables related to different slip systems 'meet'.

The yield stress

According to the relation of Taylor-Hirsch-Bailey (in the following denoted Taylor relation), the yield stress $\hat{\tau}(\boldsymbol{x}, t)$ can in a first approximation be considered as being proportional to the square root of the local dislocation density accumulated from all slip systems:

$$\hat{\tau} = \alpha \mu b \sqrt{\sum_i \varrho^{(i)}}\,, \tag{2.86}$$

where $\alpha = 0.3 \pm 0.1$ is a constant factor. Note that together with ϱ also $\hat{\tau}$ is a nonhomogeneous magnitude, i.e. a function of position and time, though in some applications of the present model a constant reference yield stress $\hat{\tau}_{\mathrm{ref}} = \alpha \mu b \sqrt{\overline{\varrho}}$ has been used in order to allow for an analytic solution of the respective problems, cf. chapter 5.

The Taylor relation is well established especially in the case of forest hardening in fcc metals, but also supposed to be valid for dipolar hardening (interaction between dislocations of the same slip system) in fcc crystals. It may lose validity for the materials where the lattice friction is dominant, that is for instance in bcc metals or transition hcp metals [93]. In the classical model the Taylor relation is the only source of short-range dislocation interactions. However we will abate this simplification in the second part of this thesis, chapters 4 and 5.

Note that long-range dislocation interactions are incorporated through the coupling to continuum mechanics, that is actually by the resolved shear stress τ. It accounts both for the applied stress and the stresses due to inhomogeneous plastic deformation.

Coupling to mechanics in the small strain framework

In the small strain framework of elasto-plastic continuum mechanics, the deformation tensor $\boldsymbol{\epsilon}$ is supposed to decompose into an elastic and a plastic part:

$$\boldsymbol{\epsilon} = \boldsymbol{\epsilon}^{\mathrm{e}} + \boldsymbol{\epsilon}^{\mathrm{p}} \,. \tag{2.87}$$

The elastic part is related to the macroscopic stress tensor $\boldsymbol{\sigma}$ via Hooke's law,

$$\boldsymbol{\sigma} = \boldsymbol{C}\boldsymbol{\epsilon}^{\mathrm{e}} \,, \tag{2.88}$$

where $\boldsymbol{C}$ is the symmetric elastic stiffness tensor, in general a fourth order tensor. A combination of both relations and of the definition of the deformation in section 2.3.1 results in

$$\boldsymbol{\sigma} = \boldsymbol{C}((\nabla u) - \boldsymbol{\epsilon}^{\mathrm{p}}) \,. \tag{2.89}$$

This is a standard eigenstrain problem, where in the present case the eigenstrain $\boldsymbol{\epsilon}^{\mathrm{p}}$ is due to the plastic strain of the material. Classical plasticity models provide the evolution of $\boldsymbol{\epsilon}^{\mathrm{p}}$ based on a constitutive law [2]. In the present model the constitutive law is replaced by the evolution equations for the dislocation fields derived above. They provide the evolution of the plastic slip γ^{p} on a number of distinct slip systems, which yields according to eq. (1.2):

$$\dot{\boldsymbol{\epsilon}}^{\mathrm{p}} = \boldsymbol{L}^{\mathrm{p}}_{\mathrm{symm}} = \left(\sum_i \dot{\gamma}^{\mathrm{p}(i)} \boldsymbol{s}^{(i)} \otimes \boldsymbol{n}^{(i)} \right)_{\mathrm{symm}} \,, \tag{2.90}$$

where $(\dots)_{\mathrm{symm}}$ denotes the symmetric part of a tensor, compare eq. (2.40). The only input required from the continuum mechanics part is the macroscopic stress $\boldsymbol{\sigma}$. It is determined from the solution of the boundary value problem (2.91_1)-(2.91_3) for $\boldsymbol{u}$ which is by means of Hooke's law (2.89), that applies to eq. (2.91_1), frequently phrased as

$$\begin{aligned}
\operatorname{div} \boldsymbol{\sigma}(\boldsymbol{x},t) &= \boldsymbol{f}(\boldsymbol{x},t) && \text{on} \quad \Omega \,, && (2.91_1)\\
\boldsymbol{u}(\boldsymbol{x},t) &= \boldsymbol{g}(\boldsymbol{x},t) && \text{on the Dirichlet boundary} \quad \partial\Omega_{\mathrm{D}} \,, && (2.91_2)\\
\nabla^{\perp}\boldsymbol{u}(\boldsymbol{x},t) &= \boldsymbol{h}(\boldsymbol{x},t) && \text{on the Neumann boundary} \quad \partial\Omega_{\mathrm{N}} \,. && (2.91_3)
\end{aligned}$$

$\nabla^{\perp}$ denotes the gradient in normal direction to $\partial\Omega_{\mathrm{N}}$, $\boldsymbol{f}$ is a given volume force, and $\boldsymbol{g}$ and $\boldsymbol{h}$ are functions defining the prescribed boundary values of displacement and distortion.
The complete model, that is the continuum theory of single-valued dislocation fields coupled to continuum mechanics, is in the following denoted as *continuum dislocation-based model* for plasticity on the μm-scale. An organisation chart visualising the interdependencies and the points of coupling is shown in figure 2.8.

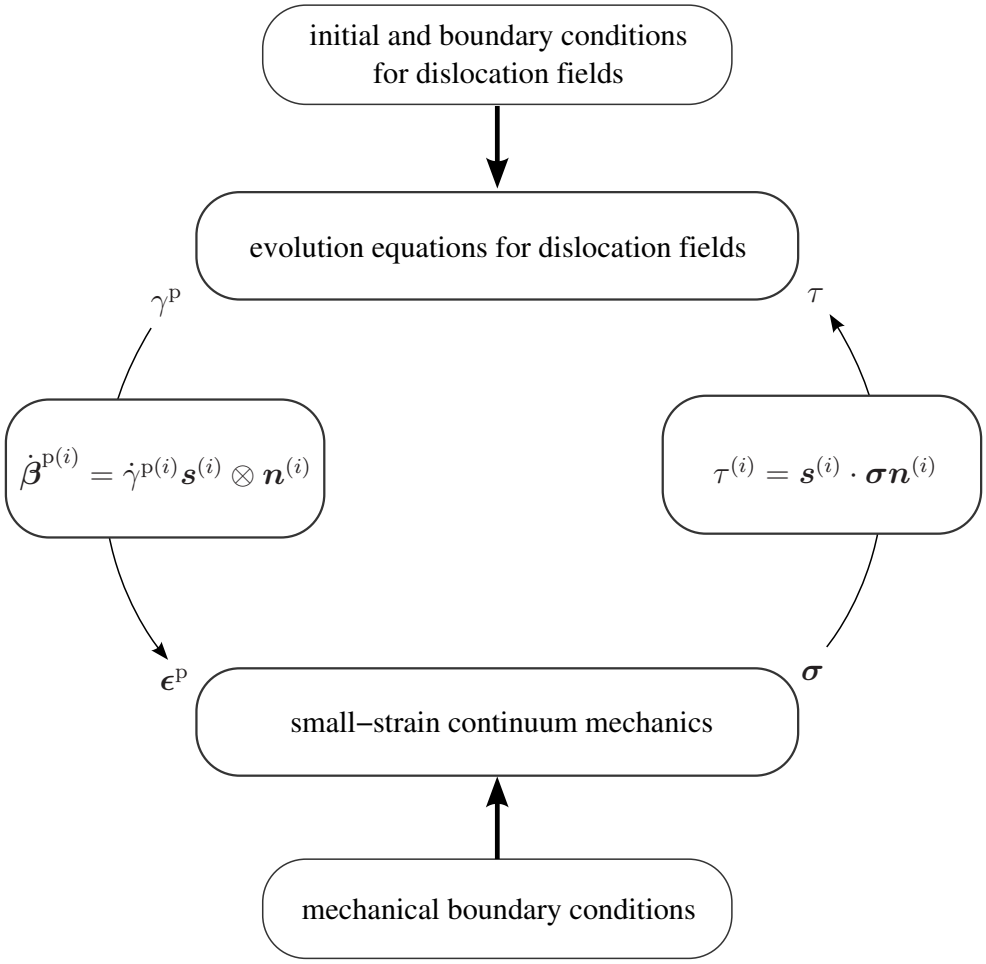

Figure 2.8: Organisation chart of the coupling between evolution equations for dislocation fields and the small-strain continuum mechanics.

2.5 Multiple-valued dislocation fields

The preceding section described in detail the treatment of single-valued dislocation fields. This is only a very special case, but nevertheless a reasonable point to start the general numerical implementation of the considered model, which is addressed in chapter 3. However, already some more general problems can be treated with the presented implementation, take for example the multiple-valued dislocation ensemble shown in the left part of figure 2.6. In this section we address the possible treatment of general multiple-valued dislocation fields by the present model. The basic idea is to separate them into single-valued fields. For this separation, Sedláček et al. [70] propose two possibilities: (*i*) to consider an initial configuration, where the separation can be performed intuitively, and then to follow the single-valued fields during evolution (special model cases, but pragmatic and simple, see applications in [70, 76, 81, 82, 94]), or (*ii*) to separate them in an automated way during computation (more general).

With regard to the treatment of multiple-valued fields a short comparison to the latest approach of Hochrainer et al. will be given.

2.5.1 ... in the model of Sedláček et al.

A concept how the presented modelling approach can be applied to multiple-valued dislocation fields has been discussed in [70]. Basically, it has to be assumed, that the mixture of dislocation segments of different orientations and curvatures in a considered volume element results from the presence of a (finite) number of continuous single-valued dislocation fields. In order to apply the theory, these fields have to be separated, and individually tracked in their time evolution. This step may be accomplished by introducing a distribution function $\phi(\boldsymbol{x}, \vartheta, \kappa, t)$ that characterises the dislocation content of a slip system in more detail than the standard scalar dislocation density $\varrho(\boldsymbol{x}, t)$. The variable $\phi(\boldsymbol{x}, \vartheta, \kappa, t)\,\mathrm{d}\boldsymbol{x}\,\mathrm{d}\vartheta\,\mathrm{d}\kappa$ has the meaning of the total length of dislocation lines on the considered slip system contained in the phase-space volume $\mathrm{d}\boldsymbol{x}\,\mathrm{d}\vartheta\,\mathrm{d}\kappa$ at time t. The scalar dislocation density of a slip system is then given as

$$\varrho(\boldsymbol{x}, t) = \int_\kappa \int_\vartheta \phi(\boldsymbol{x}, \vartheta, \kappa, t)\,\mathrm{d}\vartheta\,\mathrm{d}\kappa\,. \tag{2.92}$$

With the corresponding velocity distribution $\mathsf{v}(\boldsymbol{x}, \vartheta, \kappa, t)$, the total plastic slip rate at position $\boldsymbol{x}$ and time t results as

$$\dot\gamma^{\mathrm{P}}(\boldsymbol{x}, t) = \int_\kappa \int_\vartheta b\phi(\boldsymbol{x}, \vartheta, \kappa, t)\,\mathsf{v}(\boldsymbol{x}, \vartheta, \kappa, t)\,\mathrm{d}\vartheta\,\mathrm{d}\kappa\,. \tag{2.93}$$

The evolution equations (2.73_1) and (2.73_2) then formally read:

$$b\frac{\partial \phi}{\partial t} = -\nabla_{\boldsymbol{\nu}}(b\phi\mathsf{v})\,, \tag{2.94_1}$$

$$b\phi\frac{\partial \vartheta}{\partial t} = \nabla_{\boldsymbol{\xi}}(b\phi\mathsf{v})\,. \tag{2.94_2}$$

It is important to note, that the gradients of the dislocation density and velocity distributions required here cannot be calculated using the standard partial derivatives $\frac{\partial}{\partial x}, \frac{\partial}{\partial y}$ in the phase space for constant ϑ and κ. Instead, they have to be formed individually along the superposed single-valued dislocation fields, and thus at varying orientation and curvature. So it has to be determined, which density, orientation and curvature in the neighbourhood of a considered location in the glide plane correspond to a specific single-valued field.

The first possibility for the separation as mentioned in the introduction to section 2.5 exploits for example symmetry properties of the considered field. It was applied to model the field of expanding loops in a channel, figure 2.6, which can be clearly separated into the two single-valued fields of the upper and lower half-loops, that behave symmetrically. Method (*ii*), that is the automated separation into single-valued fields, can be accomplished considering the support of the distribution function ϕ

$$\operatorname{supp}\phi = \{(\boldsymbol{x}, \vartheta, \kappa, t) : \phi(\boldsymbol{x}, \vartheta, \kappa, t) \neq 0\}\,. \tag{2.95}$$

The supports of individual single-valued fields, each support being a three-dimensional volume in the five-dimensional phase space, in most cases separate, compare also figure 2.9. By a mapping back to the physical space, one can determine which is the correct neighbourhood of a

dislocation segment for calculating the gradients, see above. For an illustrative example, the reader is referred to [70].

As long as we presume that each dislocation configuration can be considered as a superposition of single-valued dislocation fields, the presented treatment provides a deterministic continuum model on the physical space[8].

The concept of single-valued dislocation fields is not well applicable to statistical dislocation distributions, where the individual dislocations form fully disorganised structures. However, this is a problem that any deterministic approach based on the continuum theory of dislocations has to face.

2.5.2 ... in the model of Hochrainer et al.

To set up an alternative approach to describe multiple-valued fields of curved dislocations, Hochrainer, Zaiser and co-workers very recently tackled the generalisation of Groma's statistical theory for straight edge dislocations to fields of curved dislocations. The correct treatment and averaging of curved dislocation lines in three dimensions requires elaborate mathematical concepts like differential forms and currents, which are presented in detail in [68, 74]. The resulting statistical theory is embedded in a five-dimensional phase space and essentially based on a higher order, deterministic dislocation density tensor.

The details of this very general formulation cannot be presented here. Rather attention is given to the dislocation density measure introduced by Hochrainer et al., its advantages and deficiencies. The resulting kinematic evolution equations in the case of single glide are opposed to those of the present model of Sedláček.

As starting point for their approach, Hochrainer et al. investigated a statistical density measure $\phi(\boldsymbol{x}, \boldsymbol{\theta})$ similar to El-Azab's one [66, 95], which is built on the phase space of positions and orientations[9]. It was shown [69], that its application can end up in a description of dislocation populations of different curvature by one and the same density. As a consequence, any evolution equation built on such a statistical measure cannot account for the change in total dislocation line length due to expansion or shrinkage of dislocation loops, which is based on the curvature [65]. In [72] they show furthermore, that another enlargement of the phase space by higher order contributions, for example the curvature, $\phi \rightarrow \phi(\boldsymbol{x}, \boldsymbol{\theta}, \boldsymbol{\kappa})$, could describe the evolution of a dislocation configuration only if the dislocations were restricted to conservative motion, and if the velocity of a dislocation segment depended only on the spatial point and not on the line direction or curvature of the segment. These are severe restrictions, which still hold for even higher order statistical measures.

Therefore the authors elaborated a statistical theory based on a higher order *deterministic* density

[8] Note that the introduced phase space is only a tool for the separation of single-valued fields, not fundamental for the actual model.

[9] Note that Hochrainer et al. build their theory in the three dimensional physical space, thus having not a single angle, but two angles combined to the vectorial variable $\boldsymbol{\theta}$, to define a direction/orientation of a dislocation segment.

measure [65, 68, 73]. The introduced density measure lives again on the configuration space formed by positions and directions, $(\boldsymbol{x}, \boldsymbol{\theta}) \in \mathbb{R}^3 \times S^2 =: SM$. Here S^2 is the unit sphere that can be represented by two angles. But additionally the description of the dislocation lines is lifted to the higher dimensional space SM. The lift $\mathfrak{p}$ of a dislocation line given as parametrised curve $\boldsymbol{\varphi}(\mathfrak{s})$, compare 2.1, is defined via its unit tangent vector field $\boldsymbol{\varphi}'$ as

$$\begin{aligned} \mathfrak{p} : [0, \mathfrak{S}[&\rightarrow SM\,, \\ \mathfrak{s} &\mapsto (\boldsymbol{\varphi}(\mathfrak{s}), \boldsymbol{\varphi}'(\mathfrak{s}))\,. \end{aligned} \tag{2.96}$$

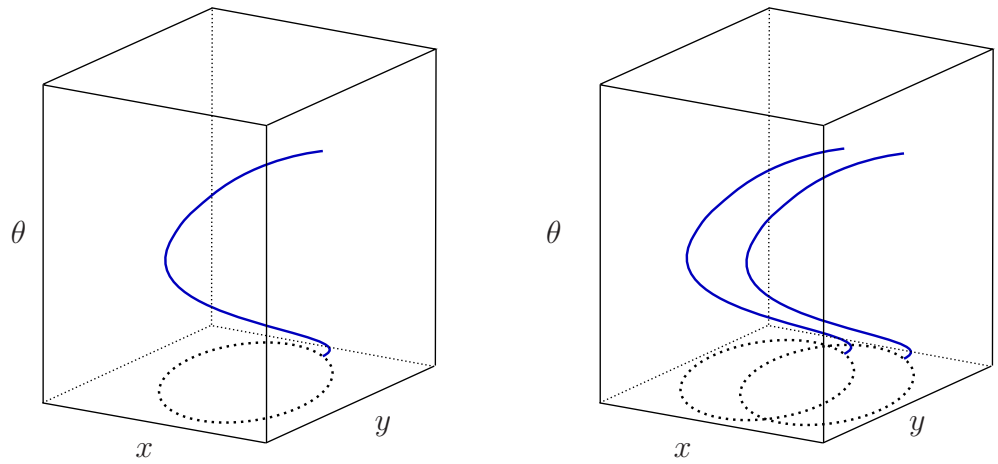

Figure 2.9: Left: Visualisation of the lift (solid, blue line) of a planar curve in the xy-plane (dashed, black line). Right: The lifts of two curves intersecting in the plane can be clearly distinguished.

The lifts of curves which cross one spatial point in $\mathbb{R}^3$, but in different directions, can be clearly distinguished, because they pass different points in SM[10], see figure 2.9 for a visualisation in the planar case ($SM = \mathbb{R}^2 \times S^1$). It is pointed out to the fact that the practical use of this lift, namely to distinguish dislocation fields passing one spatial point, is equivalent to the separation approach of Sedláček based on the support of the distribution function in the phase space.
The generalisation of the tangent to the planar curve to a tangent of its lift is given as $\mathfrak{p}'(\mathfrak{s}) = (\boldsymbol{\varphi}'(\mathfrak{s}), \boldsymbol{\varphi}''(\mathfrak{s}))$. Note that its second component is the curvature vector $\boldsymbol{\kappa} = \kappa\boldsymbol{\nu}$ of the curve. The vector field $\mathfrak{L}$ representing the tangent to the considered dislocation field in SM therefore corresponds to

$$\mathfrak{L}(\boldsymbol{x}, \boldsymbol{\theta}) \hat{=} (\boldsymbol{\xi}(\boldsymbol{\theta}), \boldsymbol{\kappa}(\boldsymbol{x}, \boldsymbol{\theta}))\,, \tag{2.97}$$

where by construction $\boldsymbol{\xi} \perp \boldsymbol{\kappa}$. From the resulting higher-order deterministic dislocation density tensor the plastic distortion and other generalised relations of the continuum theory of dislocations can be recovered.

[10] Note that $\mathfrak{p}$ can be interpreted as an element of SM because a unit vector in $\mathbb{R}^3$ can be represented by two angles, that is an element of S^2.

Remember that for the closeness of Sedláček's model all dislocation fields had to be separable into single-valued fields, which have a unique orientation in every spatial point. Hochrainer's model can now weaken this restriction: in every point in SM, only a unique curvature of the dislocations has to be presumed (or, as Hochrainer formulates [65]: 'dislocations with nearly the same direction and orientation, that is those passing the same volume element in SM, must have the same curvature'). Still it is a restriction that real dislocation configurations in non-equilibrium states will hardly ever fulfil. But if in this case some curvature averaging has to be performed, the result is still a meaningful quantity compared to an average of directions, see the introduction to this chapter and figure 2.6: while knowledge of the correct line-direction of the considered dislocations is indispensable for a meaningful definition of a velocity field, it may be tolerable to replace the actual curvature by the averaged one [65].

For a comparison to the model of Sedláček, Hochrainer et al. formulate their model for dislocations that are confined to their glide planes [74], which renders the configuration space SM a three-dimensional one, see figure 2.9:

$$SM = \mathbb{R}^2 \times S^1 = \mathbb{R}^2 \times [0, 2\pi[\,, \qquad (\boldsymbol{x}, \boldsymbol{\theta}) = (x, y, \theta)\,. \tag{2.98}$$

This assumption provides evolution equations for the total dislocation density measure $\phi(\boldsymbol{x}, \boldsymbol{\theta})$ and the curvature,

$$\frac{\partial \phi}{\partial t} = -\mathrm{Div}\,(\phi \cdot \mathsf{v}) + \phi v \kappa\,, \tag{2.99$_1$}$$

$$\frac{\partial \kappa}{\partial t} = \mathfrak{L}(\mathfrak{L}(v)) - \mathsf{v}(\kappa) - v\kappa^2\,, \tag{2.99$_2$}$$

where Div is the divergence operator on SM, v is a generalised velocity field, v is the ordinary signed scalar velocity taking effect perpendicular to the dislocation line, and $\mathfrak{L}(\cdot)$ stands for the action of a vector field on a vector in the sense of a directional derivative [65]. Formally, that is discounting the different underlying configuration spaces and sign conventions and identifying ϕ with ϱ, we find an equivalence of equations (2.99$_1$) and (2.75), that was

$$\frac{\partial \varrho}{\partial t} = -\mathrm{div}\,(\varrho \boldsymbol{v}) - \varrho v \kappa\,.$$

In both equations the curvature term accounts for the increase in total length of dislocation lines. But while in Sedláček's model the curvature is derived from the orientation due to geometrical relations, eq. (2.60), and the evolution of the orientation is described, eqs. (2.77) and (2.80$_2$), Hochrainer completes the kinematic evolution equations by the evolution equation for κ, eq. (2.99$_2$).

Remark 2.4: In [8], Sedláček for completeness also provides an evolution equation for the curvature:

$$\begin{aligned}\frac{\partial \kappa}{\partial t} &= \frac{\partial}{\partial t}(\nabla_{\boldsymbol{\xi}}\vartheta) = \nabla_{\boldsymbol{\xi}}\left(\frac{\partial \vartheta}{\partial t}\right) + \frac{\partial \vartheta}{\partial t}\nabla_{\boldsymbol{\nu}}\vartheta = \nabla^2_{\boldsymbol{\xi}} v - v\nabla_{\boldsymbol{\xi}}\nabla_{\boldsymbol{\nu}}\vartheta - v(\nabla_{\boldsymbol{\nu}}\vartheta)^2 = \\ &= \nabla^2_{\boldsymbol{\xi}} v - v\,\mathrm{grad}\,\kappa \cdot \boldsymbol{\nu} - v(\nabla_{\boldsymbol{\nu}}\vartheta)^2\,.\end{aligned} \tag{2.100}$$

The first two contributions to the curvature evolution are formally equivalent to those of Hochrainer, eq. (2.99_2), but the last is not.

In Sedláček's notation, the third term in eq. (2.99_2) corresponds to $v(\nabla_{\boldsymbol{\xi}}\vartheta)^2$. Hochrainer gives a correct and very intuitive interpretation for this term: it provides the change of curvature as found for a circular loop of radius $r = 1/\kappa$ which expands (or shrinks) with velocity v. A direct confrontation of the derivations of both equations, (2.99_2) and (2.100), is not possible, as they result from very different considerations. So we take another look at the calculation Sedláček presented in [8].

For the moment let us consider an isolated dislocation, described as parametrised curve, and not a field of dislocations as was presumed in eq. (2.100).

To get the correct Lagrangian temporal derivative with consideration of the elongation of the curve, we have to consider arbitrary time-independent parametrisation. In accordance with the present simplifications we may for example use the slip direction coordinate x as parameter. Obviously correct is the relation

$$\kappa = \frac{\mathrm{d}\vartheta}{\mathrm{d}\mathfrak{s}}\,, \quad \text{as due to Frenet} \quad \kappa\boldsymbol{\nu} := \frac{\mathrm{d}\boldsymbol{\xi}}{\mathrm{d}\mathfrak{s}} = \boldsymbol{\nu}\frac{\mathrm{d}\vartheta}{\mathrm{d}\mathfrak{s}}\,.$$

Using the relation between arc length and actual parameter x,

$$\mathrm{d}\mathfrak{s} = \left|\frac{\partial\boldsymbol{\varphi}}{\partial x}\right| \mathrm{d}x =: |\boldsymbol{\varphi}'|\,\mathrm{d}x\,, \tag{2.101}$$

this can be expressed as

$$\kappa = \frac{\vartheta'}{|\boldsymbol{\varphi}'|}\,,$$

where here and in the remainder of this remark the prime denotes the derivative with respect to x as curve parameter. The total (or Lagrangian) time derivative of κ results as

$$\frac{\mathrm{d}\kappa}{\mathrm{d}t} = \frac{\mathrm{d}}{\mathrm{d}t}\left(\frac{\vartheta'}{|\boldsymbol{\varphi}'|}\right) = \frac{1}{|\boldsymbol{\varphi}'|}\frac{\mathrm{d}}{\mathrm{d}t}\left(\vartheta'\right) - \vartheta'\frac{1}{|\boldsymbol{\varphi}'|^3}\langle\boldsymbol{\varphi}', \frac{\mathrm{d}}{\mathrm{d}t}(\boldsymbol{\varphi}')\rangle\,. \tag{2.102}$$

The parameter x is independent of t, thus we can exchange the order of differentiation. From eq. (2.65) we get the Lagrangian derivative of $\boldsymbol{\varphi}$, namely $\mathrm{d}\boldsymbol{\varphi}/\,\mathrm{d}t = v\boldsymbol{\nu}$. Further we apply the relations $\boldsymbol{\varphi}' = |\boldsymbol{\varphi}'|\boldsymbol{\xi}$, $\vartheta' = |\boldsymbol{\varphi}'|\kappa$, $\boldsymbol{\nu}' = -|\boldsymbol{\varphi}'|\kappa\boldsymbol{\xi}$, $\mathrm{d}\vartheta/\,\mathrm{d}t = \mathrm{d}v/\,\mathrm{d}\mathfrak{s}$ and the bilinearity of the scalar product. Thus the last equation simplifies to

$$\frac{\mathrm{d}\kappa}{\mathrm{d}t} = \frac{1}{|\boldsymbol{\varphi}'|}\left(\frac{\mathrm{d}v}{\mathrm{d}\mathfrak{s}}\right)' - \kappa\langle\boldsymbol{\xi}, v'\,\boldsymbol{\nu} - v\kappa\boldsymbol{\xi}\rangle = \frac{1}{|\boldsymbol{\varphi}'|}\left(\frac{\mathrm{d}v}{\mathrm{d}\mathfrak{s}}\right)' + v\kappa^2\,. \tag{2.103}$$

Applying the relations stated in eqs. (2.101) and (2.61), this is equivalent to

$$\frac{\mathrm{d}\kappa}{\mathrm{d}t} = \nabla^2_{\boldsymbol{\xi}} v + v\kappa^2\,. \tag{2.104}$$

The corresponding Eulerian evolution equation according to eq. (2.78) reads

$$\frac{\partial\kappa}{\partial t} = \nabla^2_{\boldsymbol{\xi}} v - \nabla_{\boldsymbol{v}}\kappa + v\kappa^2 = \nabla^2_{\boldsymbol{\xi}} v - v\nabla_{\boldsymbol{\nu}}\nabla_{\boldsymbol{\xi}}\vartheta + v\kappa^2\,, \tag{2.105}$$

where again $\kappa = \nabla_{\boldsymbol{\xi}}\vartheta$ was used. This now coincides with Hochrainer's evolution equation (2.99_2). Actually, the description of $\boldsymbol{\varphi}$ as parametrised curve is not available in applications of our model.

Therefore we would like to understand how the evolution of κ can be derived from the definition $\kappa = \nabla_{\boldsymbol{\xi}}\vartheta$. As was already marked in the paragraph right before eq. (2.61), the gradient in this formula has to be understood as a gradient on the curve, thus with respect to the coordinates $(\varphi_x(\mathfrak{s},t),\varphi_y(\mathfrak{s},t))$. Therefore we find due to the rules of the total derivative:

$$\begin{aligned}
\frac{\mathrm{d}}{\mathrm{d}t}\left(\nabla_{\boldsymbol{\xi}}\vartheta\right) &= \frac{\mathrm{d}}{\mathrm{d}t}\left[\cos\vartheta\,\frac{\partial\vartheta}{\partial\varphi_x}+\sin\vartheta\,\frac{\partial\vartheta}{\partial\varphi_y}\right] = \qquad (2.106)\\
&= \frac{\mathrm{d}}{\mathrm{d}t}(\cos\vartheta)\,\frac{\partial\vartheta}{\partial\varphi_x}+\frac{\mathrm{d}}{\mathrm{d}t}(\sin\vartheta)\,\frac{\partial\vartheta}{\partial\varphi_y}+\cos\vartheta\,\frac{\mathrm{d}}{\mathrm{d}t}\left(\frac{\partial\vartheta}{\partial\varphi_x}\right)+\sin\vartheta\,\frac{\mathrm{d}}{\mathrm{d}t}\left(\frac{\partial\vartheta}{\partial\varphi_y}\right) =\\
&= \nabla_{\boldsymbol{\nu}}\vartheta\,\frac{\mathrm{d}\vartheta}{\mathrm{d}t}+\cos\vartheta\left(\frac{\partial}{\partial t}\frac{\partial\vartheta}{\partial\varphi_x}+\frac{\partial^2\vartheta}{\partial\varphi_x^2}\frac{\mathrm{d}\varphi_x}{\mathrm{d}t}+\frac{\partial^2\vartheta}{\partial\varphi_x\partial\varphi_y}\frac{\mathrm{d}\varphi_y}{\mathrm{d}t}\right)+\\
&\qquad +\sin\vartheta\left(\frac{\partial}{\partial t}\frac{\partial\vartheta}{\partial\varphi_y}+\frac{\partial^2\vartheta}{\partial\varphi_x\partial\varphi_y}\frac{\mathrm{d}\varphi_x}{\mathrm{d}t}+\frac{\partial^2\vartheta}{\partial\varphi_y^2}\frac{\mathrm{d}\varphi_y}{\mathrm{d}t}\right) = \langle(2.80_2, 2.65)\rangle\\
&= \nabla_{\boldsymbol{\nu}}\vartheta\,\nabla_{\boldsymbol{\xi}}v+\nabla_{\boldsymbol{\xi}}\left(\frac{\partial\vartheta}{\partial t}\right)+v\left(\cos\vartheta\sin\vartheta\left[-\frac{\partial^2\vartheta}{\partial\varphi_x^2}+\frac{\partial^2\vartheta}{\partial\varphi_y^2}\right]+[\cos^2\vartheta-\sin^2\vartheta]\frac{\partial^2\vartheta}{\partial\varphi_x\partial\varphi_y}\right) = \langle(2.77)\rangle\\
&= \nabla_{\boldsymbol{\nu}}\vartheta\,\nabla_{\boldsymbol{\xi}}v+\nabla_{\boldsymbol{\xi}}\left(\nabla_{\boldsymbol{\xi}}v-v\mathrm{div}\,\boldsymbol{\xi}\right)+v\Big(\ldots\Big) = \langle(\mathrm{C}.4_1)\rangle\\
&= \widetilde{\nabla_{\boldsymbol{\nu}}\vartheta\,\nabla_{\boldsymbol{\xi}}}v+\nabla_{\boldsymbol{\xi}}^2v-\widetilde{\nabla_{\boldsymbol{\xi}}v\nabla_{\boldsymbol{\nu}}}\vartheta-v\nabla_{\boldsymbol{\xi}}\nabla_{\boldsymbol{\nu}}\vartheta+v\Big(\ldots\Big) =\\
&= \nabla_{\boldsymbol{\xi}}^2v-v\nabla_{\boldsymbol{\xi}}\nabla_{\boldsymbol{\nu}}\vartheta+v\Big(\ldots\Big) = \qquad \langle\text{see the following calculation on the 2nd term}\rangle\\
&= \nabla_{\boldsymbol{\xi}}^2v+v\kappa^2
\end{aligned}$$

$$\begin{aligned}
\nabla_{\boldsymbol{\xi}}\nabla_{\boldsymbol{\nu}}\vartheta &= \qquad (2.107)\\
&= \cos\vartheta\frac{\partial}{\partial\varphi_x}\left(-\sin\vartheta\frac{\partial\vartheta}{\partial\varphi_x}+\cos\vartheta\frac{\partial\vartheta}{\partial\varphi_y}\right)+\sin\vartheta\frac{\partial}{\partial\varphi_y}\left(-\sin\vartheta\frac{\partial\vartheta}{\partial\varphi_x}+\cos\vartheta\frac{\partial\vartheta}{\partial\varphi_y}\right) =\\
&= \cos\vartheta\left(-\sin\vartheta\frac{\partial^2\vartheta}{\partial\varphi_x^2}-\cos\vartheta\left(\frac{\partial\vartheta}{\partial\varphi_x}\right)^2+\cos\vartheta\frac{\partial^2\vartheta}{\partial\varphi_x\partial\varphi_y}-\sin\vartheta\frac{\partial\vartheta}{\partial\varphi_x}\frac{\partial\vartheta}{\partial\varphi_y}\right)+\\
&\qquad +\sin\vartheta\left(-\sin\vartheta\frac{\partial^2\vartheta}{\partial\varphi_x\partial\varphi_y}-\cos\vartheta\frac{\partial\vartheta}{\partial\varphi_x}\frac{\partial\vartheta}{\partial\varphi_y}+\cos\vartheta\frac{\partial^2\vartheta}{\partial\varphi_y^2}-\sin\vartheta\left(\frac{\partial\vartheta}{\partial\varphi_y}\right)^2\right) =\\
&= \left(\cos\vartheta\sin\vartheta\left[-\frac{\partial^2\vartheta}{\partial\varphi_x^2}+\frac{\partial^2\vartheta}{\partial\varphi_y^2}\right]+[\cos^2\vartheta-\sin^2\vartheta]\frac{\partial^2\vartheta}{\partial\varphi_x\partial\varphi_y}\right)-\\
&\qquad -\left[\cos^2\vartheta\left(\frac{\partial\vartheta}{\partial\varphi_x}\right)^2+2\cos\vartheta\sin\vartheta\frac{\partial\vartheta}{\partial\varphi_x}\frac{\partial\vartheta}{\partial\varphi_y}+\sin^2\vartheta\left(\frac{\partial\vartheta}{\partial\varphi_y}\right)^2\right] =\\
&= \Big(\ldots\Big)-\left[\cos\vartheta\,\frac{\partial\vartheta}{\partial\varphi_x}+\sin\vartheta\,\frac{\partial\vartheta}{\partial\varphi_y}\right]^2 = \Big(\ldots\Big)-(\nabla_{\boldsymbol{\xi}}\vartheta)^2
\end{aligned}$$

Hence it is found, that Sedláček's derivation of the curvature evolution presented in [8] was not correct. However, this now corrected result coincides with Hochrainer's evolution equations, revealing conformity of both models.

As a theoretical concept, we really appreciate Hochrainer's model and recognise a number of benefits. But concerning its applicability, that is its numerical implementation, some fundamental difficulties arise [73]. The dislocation line orientation is considered as an independent variable (in the model which is the topic of this thesis, only the directions of the physical space are the independent variables!). So to resolve this further degree of freedom, a large number of dislocation fields $\phi(\boldsymbol{x}, \boldsymbol{\theta}^{(i)})$ are required, which increases the numerical costs dramatically. A retrenchment of degrees of freedom is sought by a limitation to an edge-screw type model. For details on this very interesting approach, the reader is referred to [73].
Moreover, the general choice of reasonable boundary conditions for the dislocation curvature remains unclear.

CHAPTER 3

Numerical treatment

> I have not failed. I've just found 10000 ways that won't work.
>
> *Thomas Alva Edison (1847-1931)*

This chapter aims at giving insight into the numerical implementation of the continuum dislocation-based model for special two-dimensional applications. The problem class that can be treated with the realised implementation is described in the first section. Then difficulties we have faced during the development of first numerical schemes are reconsidered and analysed, yielding a deep understanding of the model equations and a stable implementation approach. The technical details of the two-dimensional dislocation-Lagrangian method are presented. The chapter closes with a brief introduction into the planned coupling to the Finite Element software ZeBuLoN, which unfortunately could not be completed yet due to some impediments in the progress of our cooperation with partners in Paris.

3.1 Simplifying assumptions

The scope for the examples and applications presented in this second part of the thesis is as follows.

Only such mechanical loading conditions that can be treated in a plane strain framework are considered, that implies $\epsilon^{\mathrm{e}}_{31}, \epsilon^{\mathrm{e}}_{32}$ and $\epsilon^{\mathrm{e}}_{33}$ equal zero, while σ_{33} adjusts itself to fulfil balance and to accomplish $\epsilon^{\mathrm{e}}_{33} = 0$. Voigt notation will be used, that is vector notation for the remaining components of the tensors $\boldsymbol{\epsilon}^{\mathrm{e}}$ and $\boldsymbol{\sigma}$, see section 2.4.5. Hooke's law is then phrased as

$$\boldsymbol{\sigma}_{\mathrm{V}} = \boldsymbol{C}_{\mathrm{V}} \boldsymbol{\epsilon}^{\mathrm{e}}_{\mathrm{V}} \quad \Leftrightarrow \quad \begin{pmatrix} \sigma_{11} \\ \sigma_{22} \\ \sigma_{12} \end{pmatrix} = \frac{2\mu}{1-2\nu} \begin{pmatrix} 1-\nu & \nu & 0 \\ \nu & 1-\nu & 0 \\ 0 & 0 & \frac{1-2\nu}{2} \end{pmatrix} \begin{pmatrix} \epsilon^{\mathrm{e}}_{11} \\ \epsilon^{\mathrm{e}}_{22} \\ 2\epsilon^{\mathrm{e}}_{12} \end{pmatrix} . \tag{3.1}$$

As to the dislocation part of the model, we want to consider only slip systems for which the slip direction $\boldsymbol{s}$ lies in the global x_1-x_2 plane, and the y-direction coincides with the negative x_3-direction. Such slip systems can be characterised by the angle ϕ enclosed by the slip direction $\boldsymbol{s}$ and the x_2-direction, figure 3.1, which then yields the correlations

$$\boldsymbol{e}_x = \boldsymbol{s} = \sin\phi\,\boldsymbol{e}_1 + \cos\phi\,\boldsymbol{e}_2\,, \tag{3.2$_1$}$$

$$\boldsymbol{e}_y = \boldsymbol{n}\times\boldsymbol{s} = -\boldsymbol{e}_3\,, \tag{3.2$_2$}$$

$$\boldsymbol{e}_z = \boldsymbol{n} = -\cos\phi\,\boldsymbol{e}_1 + \sin\phi\,\boldsymbol{e}_2\,. \tag{3.2$_3$}$$

The tangent and normal directions to the dislocation then can be expressed in terms of the global coordinate system:

$$\boldsymbol{\xi} = \cos\vartheta\,\boldsymbol{e}_x + \sin\vartheta\,\boldsymbol{e}_y = \cos\vartheta(\sin\phi\,\boldsymbol{e}_1 + \cos\phi\,\boldsymbol{e}_2) - \sin\vartheta\,\boldsymbol{e}_3\,, \tag{3.3$_1$}$$

$$\boldsymbol{\nu} = -\sin\vartheta\,\boldsymbol{e}_x + \cos\vartheta\,\boldsymbol{e}_y = -\sin\vartheta(\sin\phi\,\boldsymbol{e}_1 + \cos\phi\,\boldsymbol{e}_2) + \cos\vartheta\,\boldsymbol{e}_3\,. \tag{3.3$_2$}$$

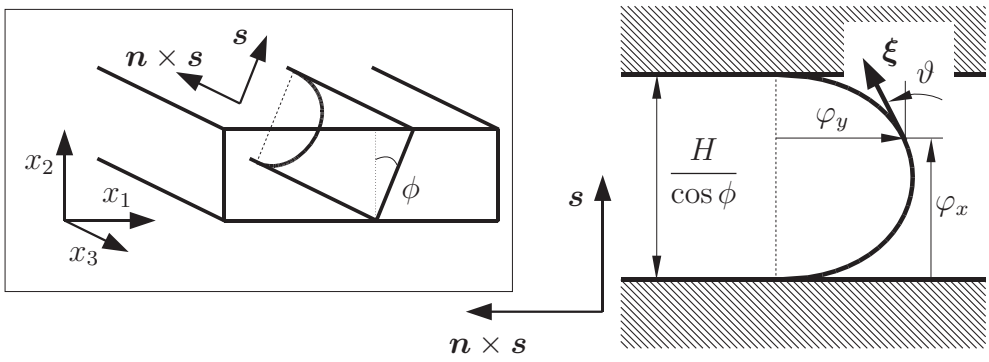

Figure 3.1: Sketch of a possible application of the present model: a single-slip system in a constrained strip is drawn in the left part of the figure and is zoomed-in in the right part; the variables describing the dislocation field are explained in the text. $\boldsymbol{s}$ is the slip direction, $\boldsymbol{n}$ the normal to the glide plane, and it is valid $\boldsymbol{n}\times\boldsymbol{s} = -\boldsymbol{e}_3$. Note that any number of slip systems can be considered, provided a deformation in the x_1-x_2 plane results. The slip systems are identified by the angle ϕ enclosed by the slip direction $\boldsymbol{s}$ and the x_2-direction.

As an initial configuration a density $\bar{\varrho}$ of straight dislocations, represented by a straight dislocation positioned at the reference position $y = 0$, with $\boldsymbol{\xi} = \boldsymbol{s}$ is assumed. Moreover we presume homogeneity of the deformation in y/x_3-direction, such that all field quantities become functions of x and time t only. In this case the curvature, eq. (2.60), is directly related to the orientation by

$$\kappa(x,t) = \frac{\partial(\sin\vartheta(x,t))}{\partial x}\,. \tag{3.4}$$

The remaining initial conditions can be phrased as:

$$\gamma^{\mathrm{P}}(x,0) = 0, \quad \vartheta(x,0) = 0\,. \tag{3.5}$$

The dislocation density ϱ is assumed to change only due to the bowing of the existing dislocations. A possible production of new dislocations is not accounted for. The current, local density $\varrho(x,t)$ is related to the constant initial density $\bar{\varrho}$ (of straight dislocations) by the local dislocation orientation:

$$\varrho(x,t) = \frac{\bar{\varrho}}{\cos(\vartheta(x,t))}\,. \tag{3.6}$$

The resulting density fulfils the compatibility condition (2.68) in the form

$$\frac{\partial(\varrho\cos\vartheta)}{\partial x} = 0\,. \tag{3.7}$$

One does not necessarily have to follow the evolution equation for $\varrho(x,t)$, but can calculate ϱ directly from the evolved orientation according to (3.6), see also the recent review article of Sedláček et al. [96]. The resulting evolution equations, that will be actually used, and the equation of motion (2.32) are summarised in table 3.1. Here the evolution of γ^{p} was specified instead of that of φ_y, cf. eqs. (2.84_1) and (2.84_2). Note that this set of equations has to be completed by suitable boundary conditions, e.g. $v = 0$ on impenetrable interfaces like passivation layers or matrix/inclusion boundaries, or $\vartheta = 0$ on free surfaces. The boundary condition $\vartheta = 0$ roughly accounts for the effect of image forces.

Lagrangian	**Eulerian**
$\dfrac{\mathrm{d}\varphi_x}{\mathrm{d}t} = -v\sin\vartheta$	
$\dfrac{\mathrm{d}\gamma^{\mathrm{p}}}{\mathrm{d}t} = b\bar{\varrho}v\cos\vartheta$	$\dfrac{\partial\gamma^{\mathrm{p}}}{\partial t} = b\varrho v = b\bar{\varrho}v/\cos\vartheta$
$\dfrac{\mathrm{d}\vartheta}{\mathrm{d}t} = \cos\vartheta v'$	$\dfrac{\partial\vartheta}{\partial t} = \cos\vartheta v' - v(\cos\vartheta)'$

Table 3.1: Comparison of the Lagrangian and Eulerian model equations in slip plane coordinates, i.e. the prime denotes $\partial/\partial x$. Each equation system has to be completed by suitable initial and boundary conditions, the correct yield condition, and the equations defining v, τ and κ: $v = \left[\operatorname{sgn}(\tau)(|\tau| - \hat{\tau})b + T\kappa\right]/B$, $\tau = \boldsymbol{s}\cdot\boldsymbol{\sigma}\boldsymbol{n}$, and $\kappa = \partial(\sin\vartheta)/\partial x$.

In the case of the Lagrangian description, a third initial condition is required in addition to those in eq. (3.5), namely that for φ_x. Remember, that $\varphi_x(X,t)$ is the function, that maps a dislocation segment X to its x-coordinate at time t. From the numerical point of view, X are discrete nodes, that carry the information of the field quantities, and that are labelled by their position at $t = 0$. Thus $\varphi_x(X,0)$ is an array of initial positions of the nodes, that are supposed to represent the segments of a representative dislocation. For the Lagrangian description it is therefore actually more correct to formulate the initial condition for a set of dislocation segments $\mathbf{X}$ as

$$\varphi_x(X,0) = X\,, \quad \gamma^{\mathrm{p}}(X,0) = 0\,, \quad \vartheta(X,0) = 0 \quad \forall X \in \mathbf{X}\,. \tag{3.8}$$

3.2 Encountered problems with the Eulerian description

The standard approach for a general implementation of the model is to use the Eulerian equations, which can be easily transformed into equations in global coordinates. But both stationary and dynamic Eulerian approach are afflicted with severe problems. They were studied in [97] on the basis of an application to the benchmark problem of shearing of a thin crystalline film in the one-dimensional form, for details see section 5.1. In this section, the findings are summarised and a rigorous mathematical analysis of the observed phenomena is performed.

3.2.1 Stationary approach

For the intended applications of the presented model, the consideration of the stationary equilibrium of the dislocation field in a given stress/deformation state according to eq. (2.23) would be sufficient. The resulting system of algebraic and partial differential equations for the single-valued dislocation fields coupled with the stationary continuum mechanics framework, table 3.2, can be treated straightforwardly by the Finite Element method.

geometrical relation, cf. fig. 2.1	$\tan\vartheta = \partial\varphi_y/\partial x$
force equilibrium	$\kappa = -[b\,\mathrm{sgn}(\tau)(\lvert\tau\rvert - \hat{\tau})]/T$
mech. balance equation	$\mathrm{div}\,\boldsymbol{\sigma} = \boldsymbol{f}$
	+ boundary conditions for $\boldsymbol{u}, \varphi_y, \vartheta$

Table 3.2: Summary of the equations describing the quasistatic equilibrium of the system.

A common weak form has to be set up using the method of weighted residuals according to Bubnov-Galerkin [98].
Using weight functions $w_i = w_i(x_2)$ and integrating over the sample height H,

$$\int_0^H \Big(w_1[\cos\phi(\sin\vartheta)' + \frac{b\,\mathrm{sgn}(\tau)}{T}(\lvert\tau\rvert - \hat{\tau})] + \\ + w_2[\cos\phi\varphi_y' - \tan\vartheta] + \boldsymbol{w}_3^{\mathrm{T}}\mathrm{div}\,\boldsymbol{\sigma}\Big)\ \mathrm{d}x_2 = 0, \quad (3.9)$$

one can find the weak form of the one-dimensional problem by application of the Gaussian integral theorem (B.11). Note the formulation in the global coordinate system, so the prime in eq. (3.9) abbreviates $\partial/\partial x_2$. The equations summarised in table 3.2 were transferred to the global coordinate system using $\partial/\partial x_2 = \cos\phi\,\partial/\partial x$. The first term in (3.9) represents the force equilibrium for the dislocations (2.23), the second term is the coupling between the material model and the mechanics, resulting from a geometrical consideration on the dislocation line, figure 2.1, and the third term accounts for the mechanical equilibrium (2.91_1) assuming $\boldsymbol{f} = 0$. Note that for brevity equation (3.9) is explicitly written for one slip system only. In

general, for each slip system a contribution of the type of the first respectively second term must be introduced. Choosing appropriate trial functions for both the weight functions w_i and the unknown functions, one arrives at a highly nonlinear system of equations.

Consider for example a one-dimensional symmetric double-slip problem. For the discretisation with $\mathcal{C}^0$ trial functions every node of the Finite Element mesh has six degrees of freedom, namely the displacements u_1, u_2, the orientation and displacement of a representative dislocation of the field on slip system 1, $\vartheta^{(1)}, \varphi_y^{(1)}$, and on slip system 2, $\vartheta^{(2)}, \varphi_y^{(2)}$. So for a Finite Element mesh of N nodes, a nonlinear equation system of size $6 \cdot N$ results, which can be solved by the Newton method.

Implementation of linear elements leads to highly dissatisfactory results: already for moderate loading, the calculated solution for the plastic slip starts to form oscillations, and consequently convergence of the Newton method fails. Using parabolic trial functions improves the behaviour somewhat, but not essentially. The reason for this behaviour is that not only the equilibria but especially the second term in (3.9), which couples the material and the mechanical model, are only weakly fulfilled, thus enabling the oscillations. It is necessary to enforce the smoothness of the results, for example by using higher order trial functions. The application of $\mathcal{C}^1$-Hermite trial functions indeed produces reasonable results which are, for our benchmark problem, in agreement with the exact solution. Note that here the number of unknowns is doubled: every node of the mesh carries now two degrees of freedom for each variable, one for its value and one for its first derivative at the node. In figure 3.2 a comparison of the profiles of the plastic slip for the double-slip shearing problem based on linear and Hermite trial functions is depicted.

The crucial problems come up when the critical bowing of the dislocations is approached, i.e. $\vartheta \to \frac{\pi}{2}$ at the impenetrable interfaces. The prescription of physically reasonable boundary conditions for the displacement φ_y of a representative dislocation line is no longer possible [76]. What is actually true for a dislocation at an impenetrable interface is a vanishing velocity, $v = 0$. But for critical bow out $v/\cos\vartheta \to$ '$0/0$', cf. eq. (2.67), so the displacement of the considered representative dislocation from the initial configuration at the interface needs not stick to 0. Retaining nevertheless the boundary condition $\varphi_y(0) = \varphi_y(H) = 0$ entails an incorrect shape of the dislocation, or in more detail, a 'bowing-back' of the dislocation line. Moreover, the computational effort for this Finite Element method for a fully two-dimensional problem with Hermite trial functions and the number of degrees of freedom at hand would be very high.

3.2.2 Dynamic approach

Allowedly, the modelling of the dislocation motion based on a drag coefficient and the Gibbs free energy, see section 2.2.2, is too rough to predict a realistic time-dependent behaviour. However, it succeeds in giving information on the qualitative way the dislocation moves, that is direction, distribution etc. of the velocity along a representative dislocation line of the field. This answers the purpose to calculate the development of the dislocation field (not considering the real time

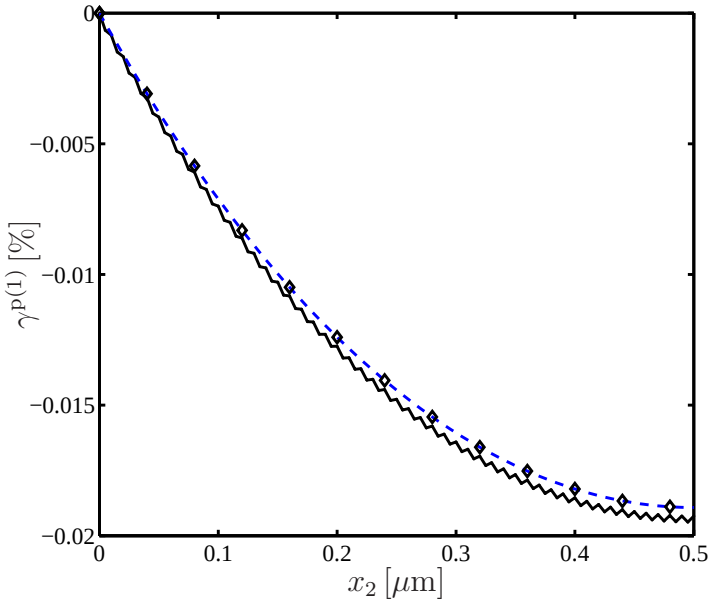

Figure 3.2: Comparison of the stationary solution of the double-slip shearing problem, presented in detail in section 5.1, calculated with linear (solid, zig-zag line) and Hermite (dashed line) trial functions. The exact solution, indicated by the diamond markers, coincides with the Hermite solution. The parameters used are $H = 1\mu\mathrm{m}$, $\phi = \pm 30$ and $\Gamma = 10^{-3}$. For the spatial discretisation 200 nodes were used. Note that for symmetry reasons only half of the strip, that is $x_2 \in (0, H/2)$, is depicted.

scale!) and its relaxed state in a given deformation/stress field. In the following, the dynamic approach is to be understood in this sense, i.e. the time-variable has no physical meaning, but is degenerated to a control parameter for the iteration / integration process. Considering the dynamic description, boundary conditions at impenetrable interfaces can be naturally set up for the dislocation velocity. A non-linear parabolic partial differential equation system for the description of the dislocation fields coupled with the elliptic problem of continuum mechanics results. A semi-discretisation method, namely the vertical line method [99], is used for the numerical solution of the parabolic system. The basic idea is to perform a discretisation in space approximating by a Finite Difference scheme the spatial derivatives in the Eulerian model equations and in the balance equation of continuum mechanics. This results in a large system of ordinary differential equations in time, which can be treated subsequently e.g. with an implicit multi-step integrator. In order to arrive at an equilibrium solution for the dislocation behaviour due to an applied load / strain, the time-integration is carried out until the dislocation velocity $v \to 0$. In the MATLAB implementation of the model, cf. section 3.4.4, a stop criterion for the time-integration has been realised using event handling. In agreement with earlier experience severe spurious oscillations in the course of the plastic slip response emerge for an increase of the applied load. In view of a two-dimensional implementation, circumvention of this phenomenon by choosing extremely small time steps is not an efficient solution. A redistribution of the nodes of the mesh used for the spatial discretisation yields more promising results. Keeping the total

number of nodes constant but pushing them closer to the boundary provides almost perfectly smooth results. The quality of the differentiation near the boundary obviously has an extremely big influence on the overall result.
This is characteristic of an entire class of partial differential equations, namely that of convection-dominated convection diffusion problems.

3.2.3 Mathematical origin of the observed phenomena

A large class of technically important partial differential equations is formed by those of convection diffusion type, also called transport equations:

$$\frac{\partial u}{\partial t} - \nabla \cdot (K \nabla u - cu) + r \cdot u = f \qquad \text{on } T \times \Omega \quad + \text{ initial \& boundary cond.} \tag{3.10}$$

The sought solution u depends on t and x, the given mapping K and functions c, r, f depend on x only. $T \times \Omega$ is called the time-space-cylinder on which u is defined. Equations of this type describe for example transport or reaction processes like heat conduction in streams or electron flow in semiconductors [99]. Probably the most famous member of this class is the Navier-Stokes equation.
The spatial discretisation must respect that information on the boundary conditions as well as possible discretisation errors are transported along streamlines only [100, p. 54]. One consequence is, that the application of explicit time integration schemes is in most cases impossible.
For a special group in this problem class, the so called **C**onvection-**D**ominated **C**onvection **D**iffusion **E**quations, the numerical treatment is even more demanding. They are characterised by a high global Péclet number, defined as

$$\mathrm{Pe} := \frac{||c||_{0,\infty} \mathrm{diam}(\Omega)}{||K||_{0,\infty}} >> 1\,, \tag{3.11}$$

where $||c||_{0,\infty} = \max_{(t,x)\in T\times\Omega} |c(t,x)|$ for continuous c, and diam(Ω) is the diameter of Ω [99]. The CD-CDEs exhibit a pronounced boundary layer behaviour: the solution is very smooth in a large domain (about 95% of Ω) and shows high gradients in a narrow zone along a boundary. They have a character very similar to that of pure advection equations, which are stable only under the **C**ourant-**F**riedrichs-**L**ewy condition restricting the ratio of temporal and spatial step size. The CFL condition embodies, that information on the discretisation mesh must not flow faster than the real physical transport [101]. Especially for two-dimensional calculations, this condition constitutes a severe drawback.

In view of these facts, the model equations at hand were investigated [96]. Consider the Eulerian description, table 3.1, and assume for simplicity a constant resolved shear stress $\bar{\tau}$ and vanishing yield stress $\hat{\tau}$. The velocity v then results as

$$v = \left[\bar{\tau} b + T \cos\vartheta \frac{\partial \vartheta}{\partial x}\right] / B\,. \tag{3.12}$$

Using this expression, a nonlinear partial differential equation of convection diffusion type for the orientation ϑ results:

$$\frac{\partial \vartheta}{\partial t} = \frac{T(\cos\vartheta)^2}{B}\frac{\partial^2 \vartheta}{\partial x^2} + \frac{\bar{\tau} b \sin\vartheta}{B}\frac{\partial \vartheta}{\partial x}\,. \tag{3.13}$$

As a constant resolved shear stress was assumed, no coupling to a mechanical problem is performed, and the equation for γ^{p} is not of interest for the analysis. The first term on the right hand side of eq. (3.13) is diffusive, the second is convective. Multiplying the coefficient of the convective term by a length $\Delta x \leq H$, one arrives at a dimensionless ratio of the coefficients of the convective and diffusive terms, which is the discrete counterpart of the above introduced Péclet number,

$$\mathrm{Pe}_{\mathrm{Eul}} = \frac{\Delta x \bar{\tau} b \sin\vartheta}{T(\cos\vartheta)^2}\,. \tag{3.14}$$

This number determines whether eq. (3.13) is locally (i.e. within a particular interval Δx) convection-dominated or diffusion-dominated.

Using order-of-magnitude estimates, $\Delta x \approx 10^{-6}[\mathrm{m}]$, $\bar{\tau} \approx 10^{7}[\mathrm{Nm}^{-2}]$, $b \approx 10^{-10}[\mathrm{m}]$ and $T \approx 10^{-9}[\mathrm{N}]$ yields $\Delta x \bar{\tau} b/T \approx 1$, so that the dislocation orientation $\vartheta(x)$ itself determines the character of the transport equation (3.13). For slightly bowed-out dislocations, cf. figure 1.7, $\vartheta \approx 0$ everywhere, so that $\mathrm{Pe}_{\mathrm{Eul}} << 1$. Equation (3.13) thus is diffusion-dominated. For dislocations in the typical bowed-out configuration, $\vartheta \to \pi/2$ in the vicinity of an impenetrable interface, figure 1.7. In this case one finds $\mathrm{Pe}_{\mathrm{Eul}} >> 1$, so that eq. (3.13) is strongly convection-dominated near the interface.

The general character and thus the behaviour of the partial differential equations building the continuum dislocation-based model does not change due to the coupling to mechanics. The mathematical explanation for the problems that have been faced since the very beginning of the numerical treatment of the present model now suggests suitable numerical methods to deal with them.

3.3 On the numerical treatment of convection-dominated transport equations

3.3.1 Eulerian schemes for convection-dominated PDEs

In the spatially one-dimensional case, a standard approach to the numerical solution of CD-CDEs are Finite Difference methods, both in semi-, that is only with respect to x, and in full-, that is with respect to t and x, discretisation schemes. Using backward differences in time, being somewhat careful with the spatial discretisation, e.g. using upwind schemes[1], and considering

[1]The idea of upwind schemes is to perform the numerical differentiation in the 'right' direction, that is considering the direction of flow, instead of just doing central finite differencing.

a number of conditions[2], reasonable computations can be accomplished. But for two- or even higher dimensional problems and complicated geometries, Finite Difference methods become very complex and inefficient.

Standard Finite Element methods suffer the same drawbacks as straightforwardly used (central) Finite Difference schemes: they are 'too symmetric', and thus do not account for the streamline direction. Therefore widely spread in the applications, see for example [102], is the streamline-upwind Petrov-Galerkin method (SUPG) [103, 104], where the idea of up-winding is transferred to the Finite Element method. The bilinear form in the weak formulation is supplemented by an additional term, which introduces an extra diffusion in direction of the convective field. Closely related to the SUPG method is the so called Galerkin least-squares FEM (GLSFEM) [105]. An application of the latter to the mechanics of dislocations can be found in [106]. Even if it is not the most accurate method, the finite volume method represents another very stable approach to the numerical solution of CD-CDEs [107]. Though based on ideas of both Finite Difference and Finite Element methods, the finite volume method is considered as a self-contained discretisation method for partial differential equations.

Especially in the materials science applications, a number of less popular methods for the treatment of CD-CDEs have been advanced recently: Limkumnerd and Sethna [108] use a 4th order viscosity regularisation for a stable treatment of their mesoscale model for grains and cells; Xiang et al. [109] take the line of level set methods [110] for dislocation dynamics: the solution curves (in their case dislocation lines) are represented as (intersections of) zero levels of higher dimensional functions.

Except for the latter, the mentioned approaches have in common, that they examine the change of the solution within a fixed region of space. A fixed mesh resp. set of control volumina can be used for the implementation, which in turn simplifies coupling to other physical processes. By this characteristic, they are classified as *Eulerian methods*.

3.3.2 The Lagrangian concept for convection-dominated PDEs

The methods presented in section 3.3.1 oppose the *Lagrangian* concept, which incorporates both Lagrange and Euler-Lagrange methods. They have in common, that the fluid particles are tracked along their trajectories. But before further discriminating the named approaches and giving some examples, let us have a look at the original idea behind Lagrange methods.

Method of characteristics In the theory of (quasi-linear) partial differential equations of first order the concept of characteristics is commonly used [111]. Characteristics are the lines in Ω along which the solution evolves in time. They can be imagined as the streamlines of a flowing

[2] as the previously mentioned CFL-condition, but also for example a restriction to the cell Reynolds number, cf. [101]

fluid. Assume the simple one-dimensional advection equation,

$$\frac{\partial u(t,x)}{\partial t} + v(t,x)\frac{\partial u(t,x)}{\partial x} = f(t,x)\,. \tag{3.15}$$

It has the same solution as the system of ordinary differential equations

$$\frac{\mathrm{d}t}{\mathrm{d}\xi} = 1, \quad \frac{\mathrm{d}x}{\mathrm{d}\xi} = v, \quad \frac{\mathrm{d}u}{\mathrm{d}\xi} = f(t(\xi), x(\xi))\,, \tag{3.16}$$

which is called the characteristic system of (3.15). The latter can be rearranged to

$$\frac{\mathrm{d}x}{\mathrm{d}t} = v, \quad \frac{\mathrm{d}u}{\mathrm{d}t} = f(t,x)\,. \tag{3.17}$$

Note, that for a vanishing source term f the trajectories along which the solution u is constant are described by $x(t)$.

The first step towards the Lagrangian methods in general is the reinterpretation of the convective part of the CD-CDE by the modified method of characteristics [112]. Suppose a generalisation of eq. (3.10) in the following form:

$$\underbrace{\frac{\partial u}{\partial t} + v(t,x,u)\cdot\nabla u}_{\text{convective part}} - \nabla\cdot(K(x)\nabla u) = f(t,x,u)\,. \tag{3.18}$$

In the convective part we find the Lagrangian or total derivative of u,

$$\frac{\mathrm{d}u}{\mathrm{d}t} = \frac{\partial u}{\partial t} + v(t,x,u)\cdot\nabla u\,, \tag{3.19}$$

compare eq. (2.78), which measures the rate of change of u following the trajectories of flow particles. The trajectories are, respectively, given as the solution of

$$\frac{\mathrm{d}x}{\mathrm{d}t} = v(t,x,u)\,. \tag{3.20}$$

Thus (3.18) can be rewritten as the convection-free PDE-system

$$\frac{\mathrm{d}u}{\mathrm{d}t} - \nabla\cdot(K(x(t))\nabla u) = f(t,x(t),u)\,, \tag{3.21$_1$}$$

$$\frac{\mathrm{d}x}{\mathrm{d}t} = v(t,x(t),u)\,. \tag{3.21$_2$}$$

In contrast to Eulerian schemes, the Lagrangian methods require only much weaker time-step restrictions. The major drawback of the plain Lagrange method is that it can go along with a severe mesh distortion as the nodes of the mesh move along the trajectories according to (3.21$_2$). This may cause accuracy problems in the solution process.

Therefore offsprings of the original concept have been developed. Methods belonging to the class of Euler-Lagrange methods implement the basic idea behind the Lagrangian concept, but include a special treatment of the mesh. The transport of information along trajectories is followed by

a projection step [113], that transmits this information to a fixed grid. The way this projection is effected has a major impact on the quality of the method. Special offsprings of this class are for example the characteristic Galerkin [114], the semi-Lagrangian [115], the grid-free semi-Lagrangian [116] or the free-Lagrangian methods [117]. The latter is for example quite close to the plain Lagrange method, but it allows for local remeshing when the mesh-distortion has become too large.

3.3.3 The Lagrangian concept applied to the continuum dislocation based model

The fundamentals necessary for the application of the Lagrangian method to the continuum dislocation based model have already been collected in section 2.4.1, see also table 3.1. Therefore, instead of manipulating the numerical solution process by artificial diffusion or by taking care of upwind directions etc. in order to conciliate the Eulerian approach, we chose to take the line of the Lagrangian methods to improve the numerical properties of the model equations.

Following the procedure in section 3.2.3 one can show that the character of the resulting equation for ϑ thus changes crucially. Assuming again a constant resolved shear stress and neglecting the yield stress, the partial differential equation for ϑ in the Lagrangian form, table 3.1, becomes,

$$\frac{\mathrm{d}\vartheta}{\mathrm{d}t} = \frac{T(\cos\vartheta)^2}{B}\frac{\partial^2\vartheta}{\partial x^2} + \frac{T\sin\vartheta\cos\vartheta}{B}\left(\frac{\partial\vartheta}{\partial x}\right)^2 , \tag{3.22}$$

see also [96]. The diffusive part is the same as in eq. (3.13), but the convective term has become nonlinear, and its coefficient has changed. The ratio

$$\frac{\Delta x\sin\vartheta}{\cos\vartheta} \tag{3.23}$$

of the coefficients of the convective part (multiplied by Δx) and of the diffusive part again goes to infinity for $\vartheta \to \pi/2$ and constant Δx. But actually, Δx represents the dislocation segment spacing, i.e. the distance between the node positions $\varphi_x(t, X)$. Because of the dislocation-Lagrangian description, the node positions evolve according to eq. (2.64), and thus Δx goes to zero in the boundary layer. Consequently, the convective term is not dominant, not even for strongly bowed out dislocations near an interface.

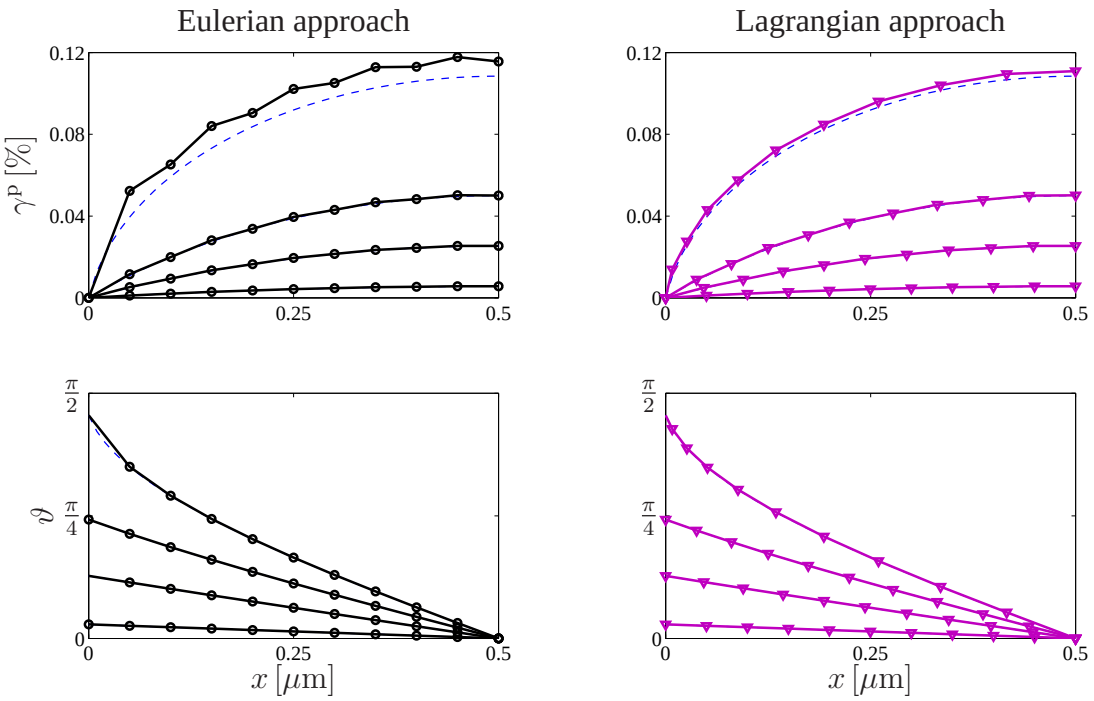

Figure 3.3: Exact solution (thin, dashed lines) for four different applied constant loads $\bar{\tau}$, cf. section 4.3, up to $99\%\tau_{\mathrm{Or}}$ compared to the numerical solution calculated with the Eulerian method (left) and with the Lagrangian method (right). Please note the redistribution of the nodes/markers for the different loads in the Lagrangian solution, that results in a very good resolution of the behaviour in the vicinity of $x = 0$.

An impressive demonstration of the performance of the plain dislocation-Lagrangian method in direct comparison to the Eulerian approach is presented in figure 3.3. In spite of the very rough discretisation, the Lagrangian solution provides sensible results. The Eulerian solution for the plastic slip, which is based on the constant node distribution, starts oscillating already for moderate stresses. In [96] it was shown by means of the simple example of concentric circular dislocation loops expanding in a constant stress field that the Lagrangian approach is even favourable when the model is applied to a problem where actually no boundary layer emerges.

3.4 Two-dimensional implementation of the dislocation-Lagrangian method

The continuum dislocation-based model is to be applied to two-dimensional plane strain settings. Let us assume a rectangular sample in the x_1-x_2 plane with width L and height H, potentially containing one or more elastic inclusions, but behaving for the most part plastically, characterised by the continuum dislocation-based model. Boundary conditions representing the mechanical load and the mobility restrictions for the contained dislocations, e.g. impenetrable interfaces, have to be imposed. Periodicity in the x_1-direction is assumed.

A short introduction to the chosen implementation of the presented model based on the dislocation-Lagrangian method in connection with the vertical line method, see section 3.2.2, for two spatial

dimensions has been presented in [118]. This chapter provides a more detailed description of the method.

3.4.1 The basic idea

In order to simulate plane strain problems, we embed the one-dimensional space of the trace of the slip plane, which was the base of all considerations in chapter 2, into a two-dimensional coordinate system. It is quite natural to take the one dimensional coordinate system of one slip plane and 'blow it up' to two dimensions by multiplication, that is by taking a finite number of slip planes to construct a discretisation of a slip system in the two-dimensional space, figure 3.4. Several distinct slip planes plus the discretisation of dislocation lines by nodes within the slip planes form the two-dimensional mesh discretising one slip system, which is not fixed due to the use of the dislocation-Lagrangian method: the nodes representing the dislocation line segments are not going to leave their slip plane, but will dynamically rearrange within this one-dimensional space according to the Lagrangian equation system of table 3.1, compare also figure 3.3.

For the solution of a mechanical problem, another mesh will be used, on which the Finite Element discretisation of the mechanical boundary value problem is based. This one will be regular and fixed in time.

For an illustration of the setting see figure 3.4. The root-points of the n slip planes representing the considered slip system, that is the intersection points with the x_1-axis, are denoted $x^0_{1i},\ i = 1, \dots n$. Note the convention, that x, y, z denote the coordinates in the slip plane, and x_1, x_2, x_3 the global coordinates, eq. (3.1).

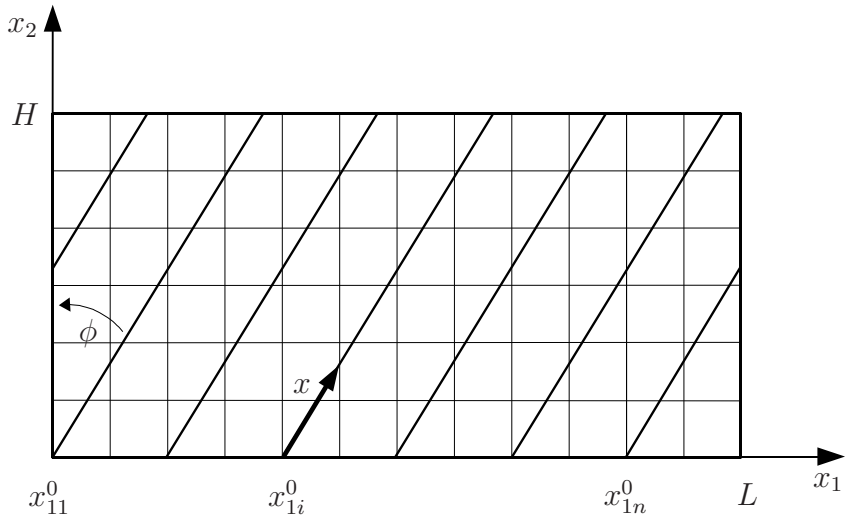

Figure 3.4: Sketch of a rectangular Finite Element mesh for the continuum mechanics computations and the discrete representative slip planes attached to root points x^0_{1i}. The global system of coordinates (x_1, x_2) and a representative local coordinate x in a slip plane with the origin at x^0_{1i} are indicated.

The transformation between the global and the slip plane coordinate systems is

$$\begin{aligned} x_1 &= x_{1i}^0 + \sin\phi \cdot x \qquad \text{if} \quad 0 \le x_{1i}^0 + \sin\phi \cdot x \le L\,, \\ x_1 &= x_{1i}^0 + \sin\phi \cdot x - L \qquad \text{if} \quad x_{1i}^0 + \sin\phi \cdot x > L\,, \\ x_1 &= x_{1i}^0 + \sin\phi \cdot x + L \qquad \text{if} \quad x_{1i}^0 + \sin\phi \cdot x < 0\,, \\ x_2 &= \cos\phi \cdot x\,. \end{aligned} \tag{3.24}$$

Note that the positioning of the root points x_{1i}^0 and the consideration of periodicity in the x_1-direction have to be implemented differently, depending on the inclination direction of the slip planes. If $\phi > 0$, the inclination to the right yields root points starting in $x_1 = 0$ but stopping before the right boundary. If $\phi < 0$, the inclination to the left yields root points starting slightly inside the sample and ending in $x_1 = L$.
The consideration of horizontal slip planes, i.e. $\phi = 90$, makes sense only in case of the presence of elastic particles. Otherwise, due to the periodicity condition in the x_1 direction, the dislocation motion would not be confined, dislocations would not have to bow out, and ideally plastic behaviour would result. In the case of horizontal slip planes a special transformation and implementation is required, which has not been implemented yet.
If one introduces more than one slip system, each of them is mostly treated individually. They meet only in the calculation of the yield stress $\hat{\tau} = \alpha\mu b\sqrt{\varrho}$, where ϱ is the sum of all slip system densities,

$$\varrho = \sum_{i=1}^{N} \varrho^{(i)}\,, \tag{3.25}$$

and when the plastic distortion tensor is calculated,

$$\boldsymbol{\beta}^{\mathrm{p}} = \sum_{i=1}^{N} \gamma^{\mathrm{p}(i)} \boldsymbol{s}^{(i)} \otimes \boldsymbol{n}^{(i)}\,, \tag{3.26}$$

compare eqs. (1.1) and (1.2) and section 2.4.5. Note that these sums are built *in every node* of either the variable slip plane-mesh or of the fixed mechanical mesh. As the variables associated with the potentially various slip systems are in generally not defined in these nodes, an interpolation step has to precede: the values of for example $\gamma^{\mathrm{p}(i)}$ given on the respective slip plane meshes first have to be interpolated to a common mesh, favourably the mechanical mesh resp. the mesh of Gauss points of the Finite Elements, in order to enable the summation over i. This can be considered as a homogenisation procedure transferring the information from the dislocation-related mesh to the course mesh used for the plane strain continuum mechanics problem.

3.4.2 Dealing with the variable mesh

To get a better impression on how the development of the node distribution within one slip plane for quite large bowing-out of a representative dislocation occurs look at figure 3.5. It shows the development of plastic slip during the time integration for the problem of shearing of a thin

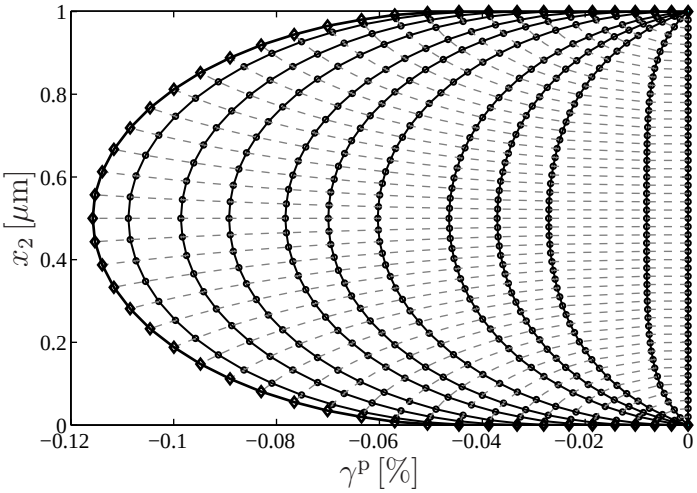

Figure 3.5: Example of the development of the node distribution in one slip plane. Shown is the plastic slip for symmetric double-slip shearing of a thin film, section 5.1, as presented in [118].

film in double-slip, compare [118] and section 5.1. The light, dashed lines indicate the course of individual nodes (dislocation segments). As the dislocation glides, the outer nodes approach the bottom and top of the film. This effect corresponds to the deposition of misfit dislocations as described by Nix [119]. Note that this pronounced effect is due to the disregard of short-range interactions, that is in the classical model the dependence of the yield stress on the current dislocation density, yielding a constant $\hat{\tau}$.

Numerically, this behaviour is quite difficult to handle. In an advanced state of the computation, the simulated dislocation line is composed of the inner nodes and the last node that has met the boundary. This last one is the node where one-sided Finite Differences have to be used to accomplish the semi-discretisation step for the PDE system. Nodes that got stuck at the boundary before are no longer part of the calculation. They are not used for the interpolation between the two meshes any longer. As the boundary condition $v = 0$ holds, neither their position nor the value of plastic slip, orientation etc. attached to these nodes is going to develop any longer. The numerical integration of the system of ordinary differential equations resulting from the vertical line method, section 3.2.2, is performed in finite time steps. Thus a node, characterised as ‘inner node’ at the beginning of a time step, that is supposed to meet the boundary in this time step will generally not meet it exactly. Different ways of how to ‘catch’ the nodes in such a case have been investigated. Quite simple, but not very accurate, is for example the usage of a thin layer around the respective interface, where nodes are pinned as soon as they enter. We finally chose to formally allow nodes to ‘leave’ the sample, that is to pass an impenetrable interface, but to reset them onto the interface each time right before the evaluation of the model equations.
A kind of characteristic array that keeps the information on the state of each node is built. This information can for example be that the node is free, pinned to an interface, has become redundant (like previous nodes that lie on an interface) or is inside an elastic particle, table 3.3. The

value in char. array	state of the node
-2	inside an elastic particle
-1	redundant on an interface
0	first node on interface, neighboured to moving nodes
1	'normal' dislocation segment **or** a free-surface node, if on the edge of the sample
2	node on a x_2-periodic boundary

Table 3.3: Overview of the used characteristic values that describe the position or state of a node representing a dislocation segment.

characteristic array is computed based on the geometry definition of the considered sample and the current node position every time right before the model equations are evaluated. The initial idea to only update the information instead of calculating it every time anew failed due to the usage of an integrator with step size control for the resulting ordinary differential equation system: an incorrect information resulting from a failed time step could not be revised in the characteristic array.

In some calculations, a strange effect could be observed: the nodes did not approach the interface uniformly, that is one by one, but were sometimes outrun by the next inner node (e.g. 2nd and 4th node already left the sample, while the 3rd is still inside), figure 3.6. The problem became obvious as the interpolation routine failed due to non-sorted nodes. For the test on the character of the nodes, this effect is fatal, as well as for the behaviour of the 'slow' node, which departs even more from the interface once it is outrun. The effect is only due to numerical inaccuracies, as it is independent of the actual implementation. An extra query to catch such exceptions has been incorporated in the code.

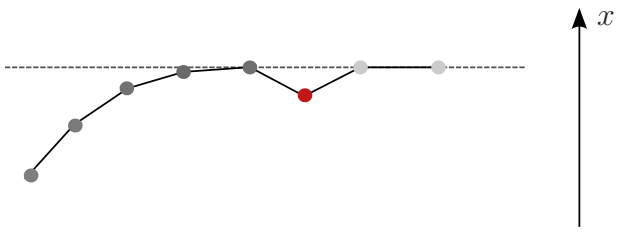

Figure 3.6: Sketch of the so called 3rd node problem: actually, only the five dark nodes on the left are of interest for the remaining calculation, the three nodes on the right have become redundant. But due to inaccuracies, the third node counted from the right end has not yet reached the interface.

Note that the specifications made in this section are valid not only for impenetrable surfaces of the entire sample, but for every interface, that is also those between plastic matrix and elastic particles, see below. In the case of more complicated structures like for example a representative cell of a composite structure, a number of further details has to be handled, the most important of which are presented in the following section.

3.4.3 2D-specific details to take care about

Dealing with more complicated two-dimensional structures requires taking care of some very special details in the implementation. As an example structure the two-dimensional projection of the metal matrix composite treated by Groh et al. [28, 30] was adopted. These authors extend a representative cell of the composite structure periodically in all three spatial directions. A three-dimensional discrete dislocations simulation in this cell acts as constitutive part for a Finite Element code used for calculating the material response to tensile loading. This is the so called discrete-continuum model (DCM), see also below, section 3.5. A first application of the continuum dislocation-based model to this composite structure was presented in [118]. In the following sketches, the white areas represent the elastic particles situated within a plastically deforming matrix. The slip planes, for clarity indicated for one slip system only, are formally introduced everywhere in the sample, but nodes within the elastic particles are accordingly labelled '-2' within the characteristic array, see table 3.3.

Care must be taken for the nodes on slip planes having intersection points with elastic-plastic interfaces, figure 3.7(a). In order to catch the internal boundary condition coming up here correctly, namely that dislocations are pinned at the interface, $v = 0$, there must be a node lying exactly on the interface, which in general is not the case after the initial uniform discretisation of the slip planes. The developed code realises this with a preprocessing step, where the node on the respective slip plane, which is inside the elastic particle the closest one to the interface, is pushed onto the interface.

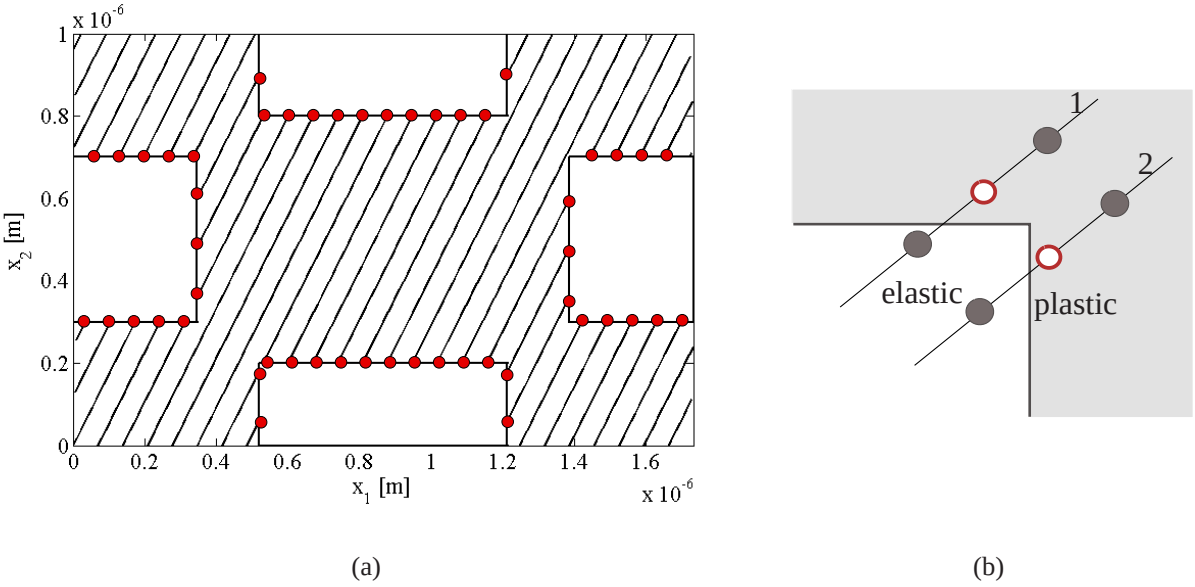

(a) (b)

Figure 3.7: Slip planes intersecting elastic-plastic interfaces.

This may not always work in a straight forward way: slip planes curtly crossing the corner of

an elastic particle will have to be more closely investigated. In the case demonstrated in figure 3.7(b), a bisection method (indicated by the empty circles) will be necessary to find out which boundary of the particle is cut. In the case where the slip plane is inclined in the other direction, it is possible that only one node is inside the elastic particle, and one has to decide onto which of the interfaces it is to be positioned.

In order to avoid numerical inaccuracies, nodes on a periodic or mechanically (stress-)free boundary, $x_2 = 0, H$, which are modelled as having orientation angle $\vartheta = 0$, are treated as Eulerian nodes, figure 3.8. In both cases the nodes are not supposed to change their position even in the Lagrangian description - theoretically. But practically numerics might yield $\mathrm{d}\varphi_x/\mathrm{d}t \neq 0$, thus moving these nodes. It is therefore favourable to use the Eulerian equations for these distinct nodes.

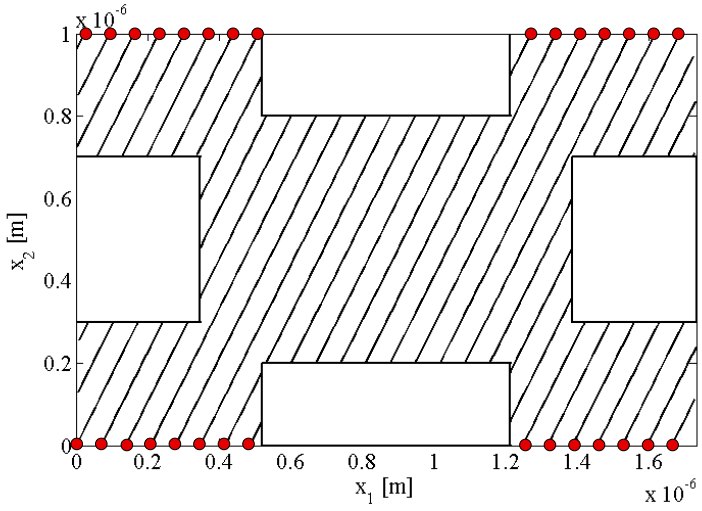

Figure 3.8: Nodes on periodic or mechanically (stress-) free boundaries.

Implementing periodic boundary conditions in the x_2-direction normally requires some extra effort. As indicated in figure 3.9 the vertical projection from top to bottom will hardly ever meet the root point of a slip plane. In the applications it showed, that using the value at the next slip plane provides more reasonable results than interpolating to the actual projection position. Actually, in this way at least a reasonable value is used. This is not the case if one meets a position close to an elastic-plastic interface, such that the two values that would serve for an interpolation represent once an elastic, and once a plastic behaviour, which yields a useless result for the projection position.

For a test on the accuracy and performance of the presented methodology, the reader is referred to [118].

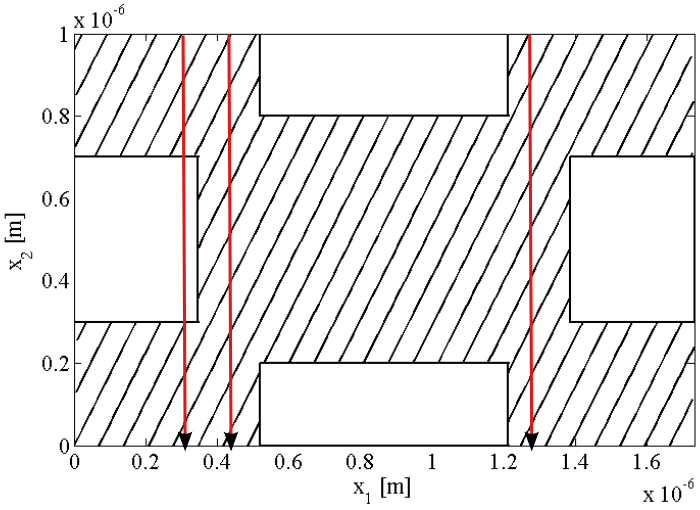

Figure 3.9: Projection required for periodic boundary conditions in x_2-direction.

3.4.4 Matlab implementation

The presented numerical solution scheme was implemented with MATLAB. This commercial software for technical computing provides a high-level language and development tools that allow for a quick development and analysis of algorithms, models and applications. The MATLAB programming language supports the vector and matrix operations that are fundamental to engineering and scientific problems and comes with a variety of numerical tools e.g. for interpolating data or solving ordinary differential equations.

The model was implemented as described in this chapter. For every sample geometry, that is considering varying boundary conditions for the dislocations or different composite structures, individual routines for building the characteristic array and doing the preprocessing step of node redistribution had to be developed. The remainder of the code is very general, especially with respect to number and orientation of slip planes. Only a computation with horizontal slip planes has not been realised.

The time integration is performed by MATLAB's explicit multi-step solver `ode113`. One-dimensional interpolation is performed by means of `interp1` with the option for piecewise cubic Hermite interpolands, two-dimensional interpolation by `interp2`, respectively. The individual slip systems and planes are organised in the data type 'cell', which is similar to a 'struct' in the programming language C. This allows for a collection of objects of different size, whereas for example in a multidimensional array all elements of a certain dimension need to have equal length.

The boundary value problem of the continuum mechanics part is solved by self-made two-dimensional linear Finite Elements on a regular rectangular grid. As to the consideration of the plastic strain in the mechanical part, we refrained from introducing Gauss points. The weak

form of the balance equation

$$\operatorname{div}\boldsymbol{\sigma} = \operatorname{div}\left(\boldsymbol{C}(\nabla\boldsymbol{u} - \boldsymbol{\epsilon}^{\mathrm{p}})\right) \quad \Rightarrow \quad \operatorname{div}\left(\boldsymbol{C}\,\nabla\boldsymbol{u}\right) = \operatorname{div}\left(\boldsymbol{C}\boldsymbol{\epsilon}^{\mathrm{p}}\right) \tag{3.27}$$

is discretised by nodal trial functions $\boldsymbol{w}$. Thus the approximation of $\boldsymbol{u}$ and $\boldsymbol{\epsilon}^{\mathrm{p}}$ based on their values in the nodes of the constant regular mesh, collected in the vectors $\hat{\boldsymbol{u}}$ and $\hat{\boldsymbol{\epsilon}}^{\mathrm{p}}$, is given by

$$\boldsymbol{u} = \boldsymbol{w}^{\mathrm{T}}\hat{\boldsymbol{u}}, \quad \boldsymbol{\epsilon}^{\mathrm{p}} = \boldsymbol{w}^{\mathrm{T}}\hat{\boldsymbol{\epsilon}}^{\mathrm{p}}\,. \tag{3.28}$$

Applying the method of weighted residuals, one arrives at a linear relation between $\hat{\boldsymbol{u}}$ and $\hat{\boldsymbol{\epsilon}}^{\mathrm{p}}$:

$$\boldsymbol{K}\hat{\boldsymbol{u}} = \boldsymbol{f}(\hat{\boldsymbol{\epsilon}}^{\mathrm{p}})\,. \tag{3.29}$$

The elastic stiffness matrix $\boldsymbol{K}$ is constructed only once at the beginning of the calculation while the right hand side vector $\boldsymbol{f}(\hat{\boldsymbol{\epsilon}}^{\mathrm{p}})$ has to be built in each time step based on the new values of $\gamma^{\mathrm{p}} \rightarrow \boldsymbol{\epsilon}^{\mathrm{p}}$. Thus actually in each time step an eigenstrain problem is solved.

Boundary conditions

Both the Dirichlet and the periodic boundary conditions are considered as constraint equations which are attended by the method of Lagrange multipliers. The constraint equation for a Dirichlet boundary condition is set up very simply: if for example the displacement in x_1-direction in a node with coordinates $\boldsymbol{x}_i$ is prescribed to be some value S, the equation is

$$u_1(\boldsymbol{x}_i) = S\,. \tag{3.30}$$

Periodic boundary conditions are in general implemented by means of a master and slave principle [120], figure 3.10. A representative volume element (RVE) of a periodic structure is supposed to have a boundary that can be decomposed into an active and a passive part[3]: the displacement at the active boundary is actually calculated while the displacement at the passive boundary is 'slaved' to the latter and to the displacement of a master node such that the deformed RVEs fit into each other like parts of a jigsaw puzzle. One often speaks of 'tying together' the nodes of active and passive boundary, that is imposing the constraint that the displacement of the corresponding nodes differs by a fixed value, the displacement of a master node. The introduction of a master node, which can be an extra node outside of the RVE or a node which is already a part of the RVE, is necessary to enable an overall strain of the considered cell, which would be prevented by tying the nodes of the corresponding boundaries directly together. In terms of the notation in figure 3.10, periodicity in x_1-direction considering the western boundary as active and the corner 2 as the master node, yields the constraint equation

$$u_i(\boldsymbol{x}_E) = u_i(\boldsymbol{x}_W) + u_i(2) \quad i = 1, 2\,, \tag{3.31}$$

[3] in many applications, this decomposition is already a very complicated task

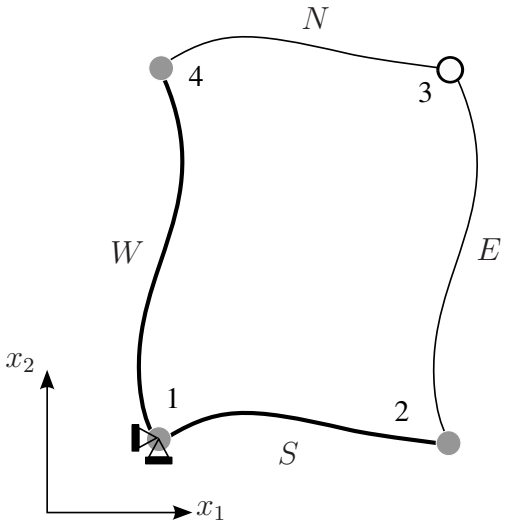

Figure 3.10: The master-slave principle for the implementation of periodic boundary conditions. In this figure, both the western and eastern face and the northern and southern face of the RVE are supposed to be equivalent with respect to the periodicity. The heavy lines form the active boundary (master faces), nodes 2 and 4 act as master nodes.

defining the displacement of the eastern boundary. The variables $\boldsymbol{x}_E, \boldsymbol{x}_W$ are representative of the corresponding nodal positions[4] on the two faces. Note that in addition, one has to assume that the undeformed geometry fulfils the condition $\boldsymbol{x}_E - \boldsymbol{x}_W = \boldsymbol{x}(2) - \boldsymbol{x}(1)$, and that vertex 1 is fixed, i.e. $u_i(1) = 0,\ i = 1, 2$.

To summarise, for every node on a Dirichlet boundary and for each pair of nodes on a periodic boundary, one gets a linear constraint equation of the form $\hat{c}(\hat{\boldsymbol{u}}) = S$, which can be combined to a linear equation system of constraints

$$\hat{\boldsymbol{C}}\hat{\boldsymbol{u}} = \boldsymbol{S}\,. \tag{3.32}$$

This system is formally appended to the formulation of eq. (3.29) in terms of potentials by means of Lagrange multipliers λ [122, p.124]. From the stationary conditions applied to the potential formulation one finds the enlarged system

$$\begin{pmatrix} \boldsymbol{K} & \hat{\boldsymbol{C}}^{\mathrm{T}} \\ \hat{\boldsymbol{C}} & 0 \end{pmatrix} \begin{pmatrix} \hat{\boldsymbol{u}} \\ \boldsymbol{\lambda} \end{pmatrix} = \begin{pmatrix} \boldsymbol{f} \\ \boldsymbol{S} \end{pmatrix}, \tag{3.33}$$

which yields the correct nodal displacements for the imposed boundary conditions.

The principle of Lagrangian multipliers, especially when applied to the Dirichlet boundary conditions, for sure is not the most economic approach: the linear equation system that has to be solved grows. However it is necessary to successfully account for the periodic boundary conditions, cf. remark 3.1, and as the principle also works well for assuring the Dirichlet boundary conditions, we stick to it for the sake of uniformity.

Remark 3.1: Initially we wanted to use the penalty method [122] to enforce the constraint equations. It works as follows: Let the value of u_i be prescribed. Then the diagonal entry (i, i) of the stiffness matrix is augmented by a number such that an entry much larger than the other entries in the ith

[4] In order to get 'corresponding' nodes, one of course has to take care for the same discretisation to be used on both faces of the cell, respectively on active and passive boundary in general. This is not a problem for our simple geometries, but a big challenge when working on voronoi meshes for example [121].

row results. The same number is added to the ith row of the right hand side vector. This yields a numerical solution with the specified u_i.
In the case of Dirichlet boundary conditions, this method works well. But when we additionally used it to accomplish periodic boundary conditions, they were not met. We suppose that the positions of the large entries in the stiffness matrix result in an ill-conditioned system, which cannot correctly provide periodicity.

It turned out that the linear elements provide a satisfying numerical solution for simple geometries, see [118] and figure 5.2. However, they are not well applicable to, for example, complicated composite structures, where discontinuous solutions for the field variables at the transition from elastic to plastic regions have to be represented. But self-made Finite Elements of higher order or for non-rectangular geometries are a technically hard job. It is therefore desirable to be able to use the present model as a material model within a standard Finite Element software. This would allow for the simulation of elaborate mechanical problems concerning the geometry of the sample and the boundary conditions.

3.5 Coupling with ZeBuLoN

Among the large variety of commercial FE software tools, ZeBuLoN was selected as the coupling partner for the continuum dislocation-based material model. This Finite Element tool, which is developed at Onera, École des Mines in Paris and NorthWest Numerics, is noted for the large variety of provided material laws.
Nevertheless, the standard interface for adding new materials is restricted to local material laws. The term 'local' means that the material model equations can be evaluated in each Gauss point independently. This fact also determines the way the FE program calls the constitutive law, namely once for each Gauss point, which is the most economic approach for the majority of available models.
However, there are also nonlocal material laws, among them the three-dimensional DD simulation, section 1.3.1, interpreted as a constitutive law [31], or the present continuum dislocation-based model. Let us try to understand the origin of non-locality in these models: clearly, the discrete dislocation segments in the DD simulation cannot move independently from each other, so in order to determine an incremental change in the dislocation arrangement both mutual stresses between the segments and external stresses on the segments are required all at once. Moreover, the segments are not related to the FE Gauss points, such that a homogenisation process (stress on centres of dislocation segments $\Leftrightarrow$ stress in Gauss points) has to be introduced. The continuum dislocation based model is after all a partial differential equation system: the temporal development at a certain spatial position is determined non-locally, that is based on spatial derivatives. The computational problem becomes clear with a look at the equations in table 3.1: to calculate the increment $\mathrm{d}\vartheta/\mathrm{d}t$, a spatial derivative of the velocity is required, i.e. a nonlocal information

on the velocity. To get the velocity everywhere, the stress τ must be available everywhere, that is in all Gauss points and not only in individual Gauss points separately. From the Lagrangian viewpoint, see section 2.4.1, this expresses that dislocation segments cannot move independently of each other.

Remark 3.2: The terms 'local' and 'non-local' constitutive law are also used in the context of multi-scale problems. A local law in this context means, that in each Gauss point of a large structure a scale transition is carried out, meaning that a separate problem on a (usually) much lower scale is solved there. Only macroscopic stresses and strains are exchanged between both problems. The Gauss points of the large structure are completely independently treated here, provided that their distance is large enough to allow for independence of the lower scale problems.

In the present cases, however, the length scale discretised by the Finite Element mesh is the same as the length scale of the material description, and we have a non-local constitutive law in the sense discussed above.

ZeBuLoN developers at Onera managed to build a library that makes it possible to choose the DD simulation implemented in the code microMegas (mM) as a material law in ZeBuLoN [31, 123, 124]. This is the technical background of the DCM mentioned before. Rather than a nonlinear material problem, ZeBuLoN solves an eigenstrain problem, which enables the work-around to the model evaluation Gauss point by Gauss point. Both codes run 'hand in hand', i.e. they run independently, but wait for some input provided by the other one at certain stations of the computation, which is realised by a parallel virtual machine (PVM), see appendix D.2. This communication is defined in the zMDC library on ZeBuLoN's side, and in the module 20gammaplas.f90 within the latest version of microMegas. For details on the communication see table D.1. It should be possible to use this library for a coupling of the continuum dislocation-based model with ZeBuLoN, 'just' replacing mM by a suitable implementation of the continuum dislocation-based model.

With this objective in mind, we developed a basic Fortran implementation of the principles presented in section 3.4. It allows for multiple slip on arbitrarily inclined slip systems, individually discretised, but so far only with the standard 'shearing of a thin strip' boundary conditions, that is periodicity in the x_1-direction and impenetrable interfaces for the dislocations in the x_2-direction [118]. A Finite Element discretisation for the mechanical problem, which was implemented in the MATLAB version of the model, was not written in Fortran, as here ZeBuLoN is intended to take that part. So testing of the implementation prior to the coupling was restricted to a constant stress.

The time integration of the ordinary differential equation resulting after a discretisation of the spatial derivatives is realised by means of the odepack-routine DLSODE, see D.3, written in Fortran77 and available at netlib.org. Even though ZeBuLoN already performs a time integration, the time step Δt_Z of which is passed to the material model, it might be necessary to use an inner

time integration in the dislocation related part of the model, too. This is similar to the possibility described in [123] for the DD simulation to take smaller time steps than the Z-integrator. But note that this inner integration will be performed for a constant stress state, the one present at the beginning of the ZeBuLoN time step. Convergence to a coupled equilibrium state is accomplished by the Newton procedure which ZeBuLoN performs to check if a time step has been successful.

For the interpolation between the variable slip plane mesh and the Gauss points of the Finite Element mesh, as a first try the bivariate polynomial interpolation routine IDBVIP, provided in the netlib package toms/526, can be used. This is certainly not optimal, neither concerning the computational effort nor the result, which is quite oscillatory for polynomial interpolation. More sophisticated interpolation routines can only be developed knowing details about the elements ZeBuLoN will use.

Some information on the acquisition and the basic handling of the used software as well as some useful links are collected in appendix D.

Remark 3.3: Unfortunately, not more details or even results of the intended coupling can be presented. One and a half year before the end of this PhD thesis, the opportunity to use the zMDC library as a tool for coupling the continuum dislocation-based model to ZeBuLoN was realised. Colleagues at Onera and ENSMP are very motivated to provide assistance on the coupling. However, it has been worked on a new version of mM and zMDC for quite a long time now, and no running ensemble was available up to now. zMDC and ZeBuLoN probably would work together and allow for a coupling of the continuum dislocation-base model, but some running test cases are required to verify all the settings before this new challenge can be tackled.

Part II

The enhanced model

CHAPTER 4

Introduction of a back stress

The continuum dislocation-based model as presented in the first part of this thesis took into account only two kinds of short-range stress fields acting on the continuously distributed dislocations: the line tension of a dislocation, which is the very essential ingredient of the model and basis for the size-effect it predicts, and the mutual short-range interactions which are approximated by the Taylor formula (2.86) for the yield stress.

However, as part of this thesis, the continuum dislocation-based model is supplemented by another short-range stress field. This *back stress* takes into account mutual interactions between different dislocations in a more detailed way than the Taylor approximation.
Both stress fields complement each other. It will be shown in section 4.3.4 that the Taylor relation is especially important for high dislocation densities, where dislocations may provide the required amount of plastic slip already by little bow-out, while the back stress gains in importance for low densities.

The chapter starts with a short consideration of the basic idea behind the back stress, that actually goes back to the pile-up stress. We continue with a short review of the present concepts to introduce the back stress in statistical and deterministic continuum models. Section 4.2 describes the definition of the back stress as it will be used to enhance the present continuum dislocation-based model. Advancing the previous approaches, we will distinguish between the interactions of parallel dislocation segments, which is sufficient when considering single-valued fields, and non-parallel dislocation segments, which is the general case. This is realised by defining the back stress as a function of the intersection angle of the considered dislocations. In order to verify a reasonable choice of the back stress, we apply the enhanced model to a simple test problem. Results for slightly deviating definitions of the back stress are compared, the numerical character of the enhanced model is investigated, and the impact of the Taylor relation and of the back stress as short-range stress fields are opposed. It appears that models considering only one of the two contributions can be considered as border cases for high respectively low dislocation densities.

4.1 The back stress in continuum models

The basis for the notion of the back stress is the effect of the pile-up stress. Consider dislocations emitted by one dislocation source, and thus lying in one slip plane. If the leading dislocation meets a barrier, further expansion of the loop will be prevented, and the following dislocations are going to pile-up behind the leading dislocation. Having the same sign, they will not annihilate, but interact elastically, such that the spacing decreases towards the front of the pile-up, see figure 4.1. If the barrier is for example a grain boundary, the described pile-up effect corresponds to the Hall-Petch mechanism, compare figure 1.5(b).

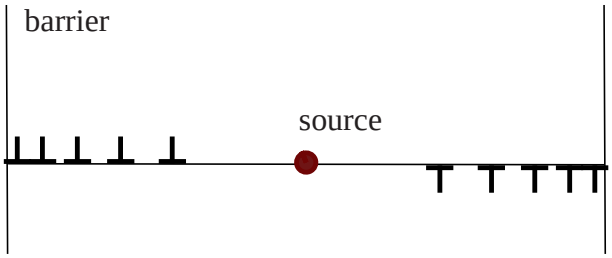

Figure 4.1: Dislocations emitted from a source and piling up against barriers: the dislocation spacing reduces in the vicinity of the barrier, see also [77] .

The stress that acts upon a dislocation in such a pile-up configuration due to the presence of the other dislocations is called pile-up or back stress. It is the foundation of the size effect predicted by the discrete dislocation dynamics model of van der Giessen and Needleman [17].

4.1.1 Statistically based model for straight dislocations

To introduce a back stress in his statistically based model [61, 62], Groma generalised the notion of the pile-up stress: a back stress of pile-up character is supposed to act not only between dislocations in one slip plane, but also between such positioned on neighbouring, parallel slip planes. In the special case of straight edge dislocations, Groma and co-workers derived an expression for the back stress by using rigorous statistical methods [62]:

$$\tau_{\mathrm{b}}^{\mathrm{Gr}}(r) = \frac{\mu b D}{2\pi(1-\nu)\rho(r)} \frac{\partial \varkappa}{\partial r} \,. \tag{4.1}$$

The authors distinguish the total dislocation density ρ and the geometrically necessary dislocation density $\varkappa$. The factor $\mu b/(2\pi(1-\nu))$ stems from the elastic stress field between edge dislocations, see for example [86]. The value of the constant $D \sim 0.8$ is determined from statistical analysis of a large number of discrete dislocation dynamics simulations of arbitrary dislocation settings.

4.1.2 Deterministic models for curved dislocations

To the author's knowledge, today no approach exists for a rigorous treatment of the mutual short-range interactions among curved dislocations in a continuum description. Nevertheless, recently

some generalisations of Groma's back stress concept were presented, eq. (4.1), to be used in continuum models for curved dislocations.

Kratochvíl et al.

Kratochvíl and Sedláček [125] introduced the back stress for fields of locally parallel curved dislocations. Instead of the geometrically necessary dislocation density $\varkappa$ the density of the well-defined single-valued dislocation fields is used. In order to account for the curved shape of the dislocations, the gradient in eq. (4.1) is evaluated in perpendicular direction to the dislocation line. The factor $\mu b/(2\pi(1-\nu))$ and the constant D were retained. The expression for the back stress proposed in [125] reads

$$\tau_{\mathrm{b}}^{\mathrm{Kr}} = \frac{\mu b D}{2\pi(1-\nu)\hat{\varrho}} \nabla_{\boldsymbol{\nu}} \varrho \,, \tag{4.2}$$

with an average reference dislocation density $\hat{\varrho}$ and the constant factor $D \sim 0.8$.

Zaiser et al.

Zaiser, Hochrainer et al. [68, 69, 73] consider a back stress in a similar form for the more general case of curved dislocations described in a three-dimensional configuration space, cf. section 2.5.2. They propose the definition

$$\tau_{\mathrm{b}}^{\mathrm{Zai}} = \frac{D_{\mathrm{z}} \mu b}{\varrho_{\mathrm{t}}} \int \nabla_{\boldsymbol{\nu}} \varrho(\boldsymbol{x}, \theta) \, \mathrm{d}\theta \,, \tag{4.3}$$

where $\varrho_{\mathrm{t}} := \int \varrho(\boldsymbol{x}, \theta) \, \mathrm{d}\theta$ is the total dislocation density. The constant D_{z} is considered as a fitting parameter of order 1 in this model.
The integrand $\nabla_{\boldsymbol{\nu}} \varrho(\boldsymbol{x}, \theta)$ measures the interactions of dislocations of one and the same orientation θ only, that is in fact parallel dislocations. Only the integral then provides the contribution of non-parallel dislocations to the back stress as it is evaluated over the various orientations present in $\boldsymbol{x}$. This means, that the back stress which acts on a dislocation of one orientation depends on the state of all the other, arbitrarily oriented dislocations in the respective position, where all orientations have equal influence. The same amount of back stress effects on every dislocation in $\boldsymbol{x}$.

4.2 The additional short-range interaction in the present model

The definition of the back stress τ_{b} as it will be introduced in the present model is geared to Kratochvíl's approach, eq. (4.2). However, considering multiple-valued fields of dislocations, we aim at a more refined treatment of the interactions of the non-parallel dislocations at hand. Suppose a multiple-valued field that is separable into N single-valued fields. For an appropriate

definition of τ_b we propose to choose the factor $D := D(\psi)$ as dependent on the angle $\psi \hat{=} \psi_{ij}$ enclosed by the line directions of the interacting single-valued fields i and j in the current position, see figure 4.2. In this chapter, we denote the dislocation density of a specific single-valued field by the variable ϱ, occasionally labeled by an index, $\varrho^{(i)}$, while representing the total dislocation density by ϱ_t, thus $\varrho_\mathrm{t} = \sum_{i=1}^{N} \varrho^{(i)}$. The back stress acting on dislocations of field number i is then defined as

$$\tau_\mathrm{b}^{(i)} = \frac{\mu b}{2\pi(1-\nu)\varrho_\mathrm{t}} \sum_{j=1}^{N} D(\psi_{ij}) \nabla_{\boldsymbol{\nu}^{(i)}} \varrho^{(j)} \,. \tag{4.4}$$

The gradient is calculated in perpendicular direction to the field i for which the effective back stress is required, that is $\boldsymbol{\nu}^{(i)}$, as this is the direction of motion and thus the sense of the repulsive back stress acting on dislocations of field i, too. However, for the effect which 'the other' fields have on field i, this gradient is applied to their respective density. By this approach we take into account the effect of all the 'other' single-valued fields, considering their relative orientations, which may result in a different amount of back stress acting on different fields.

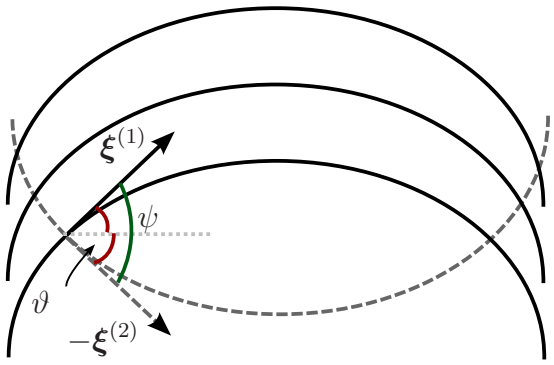

Figure 4.2: Two dislocation fields intersecting each other. The back stress effecting on the upper half loops is not determined by the mere sum of the density gradient of both upper and lower half loops. We assume, that the back stress effected by dislocations of the 'other' field depends on the angle enclosed by dislocations of both fields. This angle ψ is in the present model a unique function of x. In the depicted symmetric case, where the two fields combine to the field describing expanding loops, it results as $\psi = 2\vartheta$, compare also figure 2.6.

The functional dependence for $D(\psi)$, accounting for the contribution of 'the other' field to the back stress, shall be subject to the following two conditions:

- Dislocations meeting almost parallel, $\boldsymbol{\xi}^{(i)} \parallel \boldsymbol{\xi}^{(j)}$, for example dislocations of one single-valued field, exert the maximum possible stress onto each other. In accordance with Kratochvíl, eq. (4.2), we assume $D(0) = 0.8$.

- Dislocations intersecting perpendicularly, $\boldsymbol{\xi}^{(i)} \perp \boldsymbol{\xi}^{(j)}$, do not interact at all, $D(\pi/2) = 0$.

The second condition is reasonable only in view of the present assumptions, namely that the interacting dislocations glide in parallel slip planes and that only in-plane interactions are of interest. The perpendicularity is thus measured between the projections of the dislocations onto a representative of these planes. Generally, dislocations meeting perpendicularly in the crystal may for example interact through intersection mechanisms like kink and jog formation [86].

In section 4.3 the simple example of a multiple valued dislocation field is considered which results if one treats the upper and lower half loops of expanding loops in a channel as two single-valued fields. In this highly symmetric case, where only the motion of one of the fields needs to be explicitly calculated, the intersection angle results directly from the dislocation orientation as $\psi = 2\vartheta$, figure 4.2.

Remark 4.1: In the present continuum description not one isolated slip plane is considered, but continuously distributed slip planes in a sample. Having this in mind, the interaction of non-parallel dislocation fields residing on different slip planes may also be understood as a passing stress. This is the attractive force encumbering the dissociation of a dipole formed by two dislocations of opposite sign that reside on neighbouring slip planes.
Recently, Křišťan and Kratochvíl investigated the interactions of dislocations in a channel of a persistent slip band [126]. Using a similar description for curved dislocations as in the present model, upper and lower bounds for the passing stress of two screw dislocations were determined. To provide a valuable model for the endurance limit found in fatigue tests also line tension effects and the internal stress resulting from inhomogeneous plastic deformation were taken into account.

Equation of motion

The repulsive stress acting between two parallel dislocation segments impedes the dislocation motion, and can thus be assumed to act perpendicular to the dislocation line. We generalise this notion to the back stress, and introduce its effect as perpendicular to the dislocation line, too. Therefore, it can be appended to the equilibrium of forces (2.32). We consider the back stress as acting in any case against the resolved shear stress τ, thus ending up with

$$Bv = \begin{cases} b(\tau - \hat{\tau} - |\tau_\mathrm{b}|) + T\kappa & \text{if} \quad b\tau + T\kappa > b(\hat{\tau} + |\tau_\mathrm{b}|) \\ 0 & \text{if} \quad |b\tau + T\kappa| \leq b(\hat{\tau} + |\tau_\mathrm{b}|) \\ b(\tau + \hat{\tau} + |\tau_\mathrm{b}|) + T\kappa & \text{if} \quad b\tau + T\kappa < -b(\hat{\tau} + |\tau_\mathrm{b}|) \end{cases} , \tag{4.5}$$

or in the abbreviated form

$$Bv = b\,\mathrm{sgn}(\tau)(|\tau| - |\tau_\mathrm{b}| - \hat{\tau}) + T\kappa \quad \text{if} \quad |b\tau + T\kappa| > b(\hat{\tau} + |\tau_\mathrm{b}|)\,. \tag{4.6}$$

As for the yield condition we accept Kratochvíl's interpretation in [64], that the back stress has the same character as the yield stress, so that it contributes as a stress to be overcome to the right hand side of the yield condition.

4.3 Verification of the enhanced model

Before using the back stress in real applications of the present model, we need to ascertain that a reasonable expression for the back stress was chosen. We examine the simple case of expanding loops in a channel of width H, which decompose into two symmetrically evolving single-valued

fields, figures 2.6 and 4.2. Each field is described by a density ϱ, such that $\varrho_\mathrm{t} = \varrho^{(1)} + \varrho^{(2)} = 2\varrho$. They are exposed to a constant homogeneous load $\tau =: \bar{\tau} = \text{const.} > 0$, such that the coupling to continuum mechanics is eliminated. The calculations are performed in the one-dimensional framework, that is with all variables depending only on the slip direction coordinate x.
As the border case of a rather small dislocation density is examined, the yield stress, and with it the short-range interactions approximated by the Taylor relation, is neglected. This allows for analytic solutions and provides a better understanding for the basic character of the back stress. These assumptions will be justified in section 4.3.4.
For this setting, the following ordinary differential equation for the orientation ϑ can be derived from the static equilibrium of forces, resulting from eq. (4.6) in the limit $B \to 0$:

$$(\bar{\tau} - |\tau_\mathrm{b}|)\, b + T \cos\vartheta \frac{\partial \vartheta}{\partial x} = 0\,, \tag{4.7}$$

where $\kappa = \frac{\partial(\sin\vartheta)}{\partial x}$, eq. (3.4), was used.
Inserting a concrete definition of τ_b, using $T = \mu b^2$ and applying the method of the separation of variables, this differential equation can be solved at least for the inverse function $x(\vartheta)$.

Remark 4.2: Neglecting *both* yield stress and back stress, the analytic solution for the shape of a representative dislocation $\varphi_y(x)$ in a constant stress field is found as a segment of a circle with radius $r = \mu b/\bar{\tau} \geq H/2$. The maximum allowed stress corresponds to a circular arc of radius $H/2$ and is denoted the Orowan stress:

$$\tau_\mathrm{Or} = \frac{2\mu b}{H}\,. \tag{4.8}$$

4.3.1 Zaiser's definition of the back stress, constant D

For a first simple reference solution of our problem, we go back to Zaiser's definition of the back stress, eq. (4.3). In the present example, only two different orientations θ are present, which behave moreover equally, such that the integral collapses. Using our notation and $\varrho = \bar{\varrho}/\cos\vartheta$, eq. (3.6), which is valid for a single-valued dislocation field with the initial density $\bar{\varrho}$ of straight dislocations, we end up with the following expression for Zaiser's back stress:

$$\tau_\mathrm{b}^\mathrm{Zai} = -\mu b D_\mathrm{z} \cos\vartheta \sin\vartheta \frac{\partial}{\partial x}\left(\frac{1}{\cos\vartheta}\right) = -\mu b D_\mathrm{z} \sin\vartheta \tan\vartheta \frac{\partial\vartheta}{\partial x} \;\; (>0 \text{ here})\,. \tag{4.9}$$

Introducing the abbreviation $\bar{D} = \mu b D_\mathrm{z}$, the solution of eq. (4.7) results as

$$x(\vartheta) = -\left[\bar{D}\left(\log\left|\tan\left(\frac{\vartheta}{2} + \frac{\pi}{4}\right)\right| - \sin\vartheta\right) + \mu b \sin\vartheta\right]/\bar{\tau} + c\,. \tag{4.10}$$

The integration constant c is determined from the symmetry condition $x(0) = H/2$ as

$$c = \frac{H}{2}\,. \tag{4.11}$$

The correct interval from which ϑ may be taken to yield $x \in [0, H]$ depends on the applied stress $\bar{\tau}$. A closed form solution for the maximum value of the orientation, $\beta := \max\vartheta$, cannot be

found for an arbitrary choice of D_z, so it needs to be approached numerically.
In [73], Zaiser et al. use $D_z = 1$, which results in a very high back stress and thus a strong retardation of the plastic deformation. For this special case a closed solution for ϑ can be found, see remark 4.3.
Alternatively we choose, consistent with Kratochvíl's definition of the back stress, on which in turn our refined definition is based, $D_z = D/2\pi(1-\nu)$, where $D = 0.8$ =const. This choice yields, in our opinion, a more realistic amount of the back stress.
The results for both values of D_z are opposed in figure 4.3.

Remark 4.3: Using Zaiser's choice $D_z = 1 \rightsquigarrow \bar{D} = \mu b$, and presumed $\vartheta \in [-\pi/2, \pi/2] \rightsquigarrow \tan(\frac{\vartheta}{2} + \frac{\pi}{4}) > 0$, the closed solution for $\vartheta(x)$ results as:

$$\vartheta(x) = 2\left[\arctan\left(\exp\left[-\frac{\bar{\tau}}{\zeta}(x - \frac{H}{2})\right]\right) - \frac{\pi}{4}\right], \tag{4.12}$$

such that $\vartheta \in [-\beta, \beta]$ with

$$\beta = 2\left(\arctan\left[\exp\left(\frac{\bar{\tau}H}{2\mu b}\right)\right] - \frac{\pi}{4}\right). \tag{4.13}$$

As was already observed in [73], the plastic slip approaches a shape where a pronounced boundary layer and a flat plateau region in the centre of the slip plane dominate. In terms of the orientation, this shows as a plateau in the vicinity of the surfaces at a level close to $\pi/2$, and an approximately linear course in the centre. The stress-strain curves for both choices of D_z and for two different widths H are depicted in figure 4.5: for $D_z = 1$, the linear τ-$\langle\gamma^{\mathrm{p}}\rangle$-dependence is hardly affected, while for $D_z = D/2\pi(1-\nu)$, $D = 0.8$, the stress is notably released through the plastic deformation.

4.3.2 Refined back stress, orientation-dependent D

Equation (4.4) for the refined back stress acting on one of the two single-valued fields reduces for the considered one-dimensional and symmetric case to

$$\tau_{\mathrm{b}} = \frac{\mu b}{2\pi(1-\nu)\varrho_{\mathrm{t}}}(D(\psi) + D(0))(-\sin\vartheta)\frac{\partial\varrho}{\partial x} := -\frac{\tilde{D}(\psi)}{\varrho}\sin\vartheta\,\frac{\partial\varrho}{\partial x}, \tag{4.14}$$

$$\text{where } \psi \hat{=} \psi_{12}\,, 0 \hat{=} \psi_{11} \text{ and } \tilde{D}(\psi) := \frac{\mu b}{4\pi(1-\nu)}(D(0) + D(\psi))\,.$$

$D(0)$ accounts for the interactions within one single-valued field, and $D(\psi)$ for the interactions between dislocations belonging to different fields, thus being in general non-parallel.
Using again $\varrho = \bar{\varrho}/\cos\vartheta$, this yields the following simple expression for τ_{b} depending on ϑ only:

$$\tau_{\mathrm{b}} = -\tilde{D}(\psi)\cos\vartheta\sin\vartheta\,\frac{\partial}{\partial x}\left(\frac{1}{\cos\vartheta}\right) = -\tilde{D}(\psi)\sin\vartheta\tan\vartheta\,\frac{\partial\vartheta}{\partial x}\,. \tag{4.15}$$

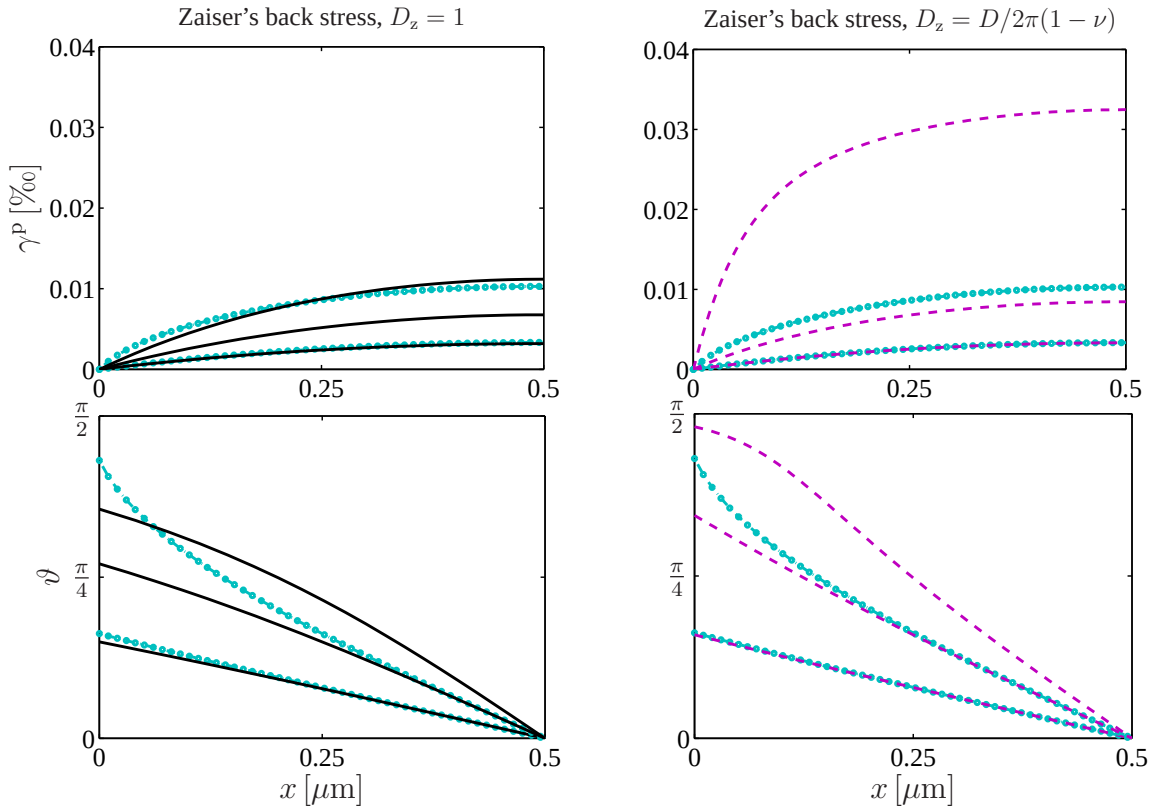

Figure 4.3: For applied constant loads $\tau = \{10, 20, 30\}$MPa, the solutions without a back stress (cyan, markered lines, only for the first two cases as $\tau_{\mathrm{Or}} = 20.48$ MPa) are opposed to the solutions with a back stress considered: the black solid lines on the left correspond to the back stress due to Zaiser's formula with $D_z = 1$, while the magenta, dashed lines on the right represent the solution for $D_z = D/2\pi(1-\nu)$, $D = 0.8$. The factor $D/(2\pi(1-\nu))$ has crucial effect on the strength of influence of the back stress. The depicted results are based on parameters $\bar{\varrho}_t = 10^{11}\mathrm{m}^{-2}, \mu = 40\mathrm{GPa}, b = 0.256\mathrm{nm}$ and $H = 1\mu$m. Note that the symmetry of the solution was exploited and only half of the slip plane is shown.

Remark 4.4: Note that in case $D(0) = D(\psi)$, that is $D =$const., we have a correspondence to Zaiser's approach where $D_z := D/2\pi(1-\nu)$, as then $\tilde{D} = \bar{D}$, see section 4.3.1.

If we apply $\tau_b > 0$, which is for the present problem true as $\partial\vartheta/\partial x < 0$ and $\vartheta \in [-\pi/2, \pi/2]$, such that $\mathrm{sgn}(\sin\vartheta\tan\vartheta) = 1$, eq. (4.7) expands into

$$\left(\bar{\tau} + \tilde{D}(\psi)\sin\vartheta\tan\vartheta\,\frac{\partial\vartheta}{\partial x}\right) b + T\cos\vartheta\,\frac{\partial\vartheta}{\partial x} = 0\,. \tag{4.16}$$

As a simple functional expression for $D(\psi)$ we now choose

$$D(\psi) = \frac{2}{5}\left[\cos(2\psi) + 1\right] = \begin{cases} 0.8 & \text{for } \psi = 0, \pi, \\ 0 & \text{for } \psi = \pi/2\,. \end{cases} \tag{4.17}$$

Using $\psi = 2\vartheta$, this yields

$$\tilde{D}(\vartheta) = \frac{\mu b}{4\pi(1-\nu)}\,\frac{2}{5}\left[2 + (\cos(4\vartheta) + 1)\right]\,. \tag{4.18}$$

For this special choice of $D(\psi)$, the analytic solution to the problem of dislocations in a homogeneous stress field, eq. (4.16), is given as:

$$x(\vartheta) = -\Big(\frac{4}{5}\cdot\frac{\mu b}{2\pi(1-\nu)}\left[\log(\sec\vartheta+\tan\vartheta) - \frac{\sin\vartheta}{5}\left(2\cos^4\vartheta - 4\cos^2\vartheta + 7\right)\right] + \mu b\sin\vartheta\Big)/\bar{\tau} + \frac{H}{2}$$

Note that also here a suitable interval $\vartheta \in [\beta, -\beta]$ has to be determined according to the applied stress $\bar{\tau}$.

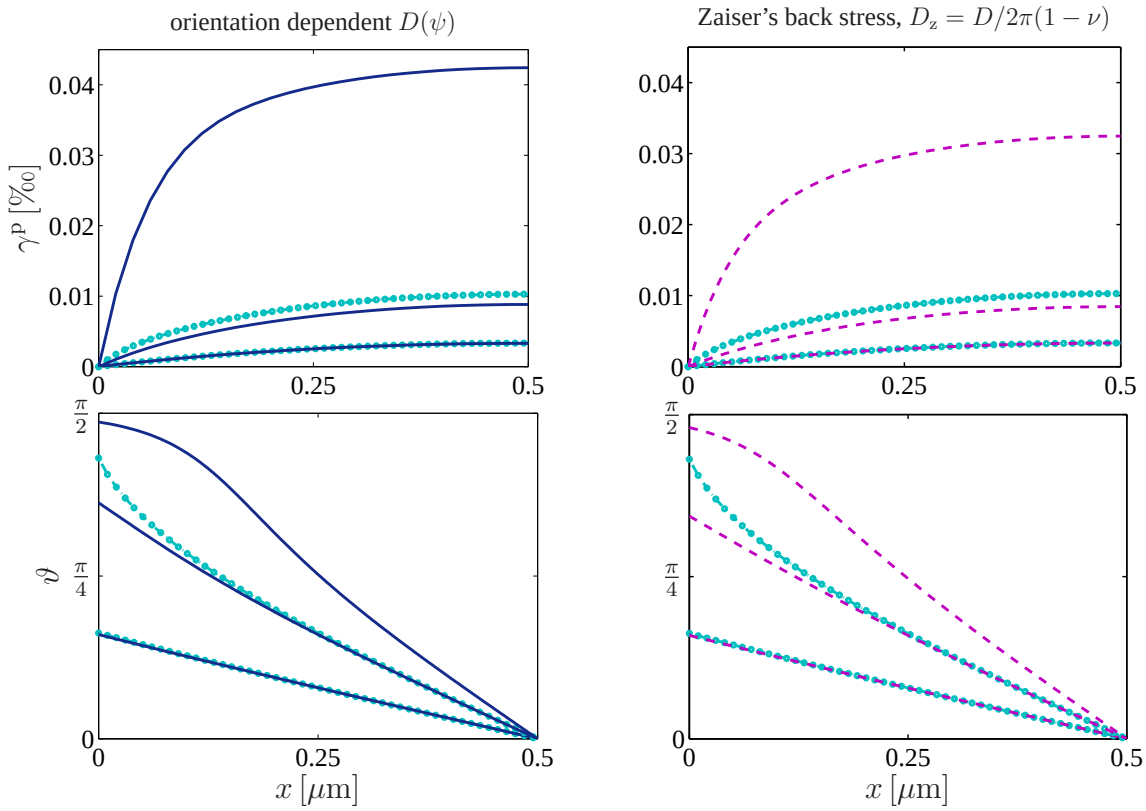

Figure 4.4: For applied constant loads $\tau = \{10, 20, 30\}$MPa, the solutions without a back stress (cyan, markered lines, only for the first two cases as $\tau_{\mathrm{Or}} = 20.48$ MPa) are opposed to the solutions with a back stress considered: for the solution depicted with blue solid lines on the left, the orientation dependent factor $D(\psi) = \frac{2}{5}[\cos(2\psi) + 1]$ was used; the magenta, dashed lines on the right represent the solution for the back stress based on a constant $D = 0.8$, which is equivalent to Zaiser's back stress with $D_{\mathrm{z}} = D/2\pi(1-\nu)$ in figure 4.3, cf. remark 4.4. The results are based on parameters $\bar{\varrho}_{\mathrm{t}} = 10^{11}\mathrm{m}^{-2}, \mu = 40\mathrm{GPa}, b = 0.256\mathrm{nm}$ and $H = 1\mu$m. Note that for symmetry reasons, only half of the slip plane is shown.

In figure 4.4, this result is opposed to the reference case of a constant factor $D = 0.8$, which is equivalent to the case considered in the previous section where $D_{\mathrm{z}} = D/2\pi(1-\nu)$ was chosen, see also figure 4.3. It is distinct, that the plastic deformation can be more effectively transported by the dislocations if the back stress due to 'the other' field is assumed to be softer, that is when $D(\psi)$ is chosen orientation dependent. Figure 4.5 shows the stress-strain relation for both possibilities for two different widths $H = 1$ and 2.5μm of the channel. Assuming the back stress being affected by another dislocation field to be softer than the back stress among parallel

dislocations yields a softer material response. Again it shows, that the orientation dependent back stress results in a minor retardation of the dislocation motion.

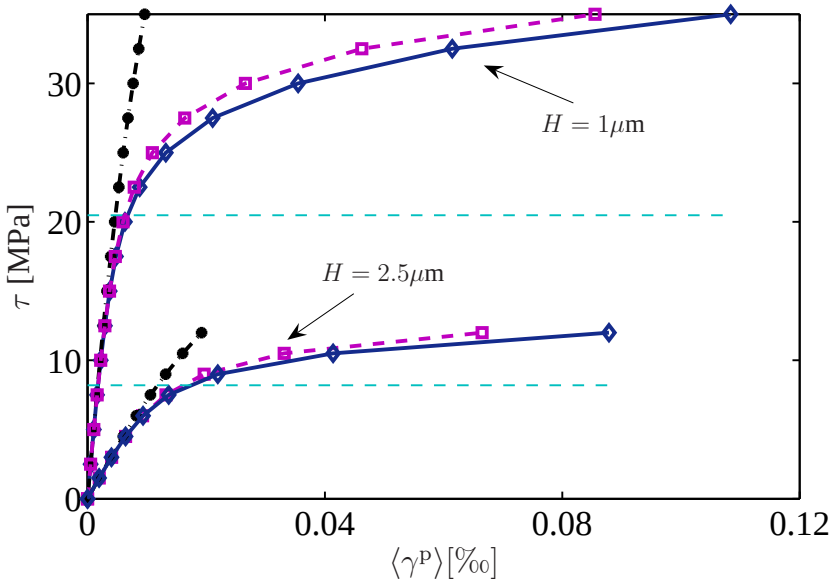

Figure 4.5: Stress-strain curves for $H = 1\mu$m and $H = 2.5\mu$m, where for both values the results with orientation dependent (diamond markers) and constant (square markers) D as well as for Zaiser's choice $D_{\mathrm{z}} = 1$ (circle markers) are shown. The thin horizontal lines correspond to the classical Orowan stress $\tau_{\mathrm{Or}} = 2\mu b/H$. As dislocations are more slowed down using a constant factor D, the plastic slip for a prescribed constant load has a lower value. For $D_{\mathrm{z}} = 1$ hardly any plastic deformation develops, and a very steep τ-$\langle\gamma^{\mathrm{p}}\rangle$-response results. The depicted results are based on parameters $\bar{\varrho}_{\mathrm{t}} = 10^{11}\mathrm{m}^{-2}, \mu = 40\mathrm{GPa}, b = 0.256\mathrm{nm}$.

4.3.3 Numerical character of the enhanced model

The introduction of the back stress has a very positive effect on the behaviour of the numerical solution of the partial differential equation system of the dynamic approach, cf. table 3.1. Large bow-out of dislocations can be simulated using the Eulerian description without any problems coming up. We would like to give an explanation for this observation by means of the Péclet analysis, compare section 3.2.3, of the Eulerian evolution equation for ϑ based on the velocity

$$v = \left[\bar{\tau}b - \tau_b^* b + T\cos\vartheta\frac{\partial\vartheta}{\partial x}\right]/B\,. \tag{4.19}$$

For simplicity of the Péclet analysis, we consider only one dislocation field, i.e. $\varrho_{\mathrm{t}} = \varrho$, and assume, corresponding to Zaiser's approach based on $D_{\mathrm{z}} = 1$, sec. 4.3.1, the constant parameter $\tilde{D}^* = \mu b$ in eq. (4.14). The back stress then results in the form

$$\tau_b^* = \frac{\mu b}{\varrho}\nabla_{\boldsymbol{\nu}}\varrho = -\mu b\sin\vartheta\tan\vartheta\,\frac{\partial\vartheta}{\partial x}\,. \tag{4.20}$$

After lengthy calculation, one arrives at the parabolic equation

$$\frac{\partial\vartheta}{\partial t} = (\mu b^2 \sin^2\vartheta + T\cos^2\vartheta)\,\frac{\partial^2\vartheta}{\partial x^2} + \left[\mu b^2(\cos\vartheta\sin\vartheta + \tan\vartheta + \sin^2\vartheta\tan\vartheta)\right]\left(\frac{\partial\vartheta}{\partial x}\right)^2 + \\ + \bar\tau b\sin\vartheta\,\frac{\partial\vartheta}{\partial x}\,. \quad (4.21)$$

There are now two 'convective' terms, one in $\partial\vartheta/\partial x$ and one in $(\partial\vartheta/\partial x)^2$, both with coefficients making them highly nonlinear. A Péclet analysis in the mathematically strict sense is not possible here, as the treatment of the quadratic convective term is not defined. However we make the following ad-hoc consideration yielding again a dimensionless measure, denoted Pe^*, to quantify the numerical character of the problem:

$$\mathrm{Pe}^* := \frac{\Delta x\left|\bar\tau b\sin\vartheta + \mu b^2(\cos\vartheta\sin\vartheta + \tan\vartheta + \sin^2\vartheta\tan\vartheta)\frac{\partial\vartheta}{\partial x}\right|}{\left|\mu b^2\sin^2\vartheta + T\cos^2\vartheta\right|}\,. \quad (4.22)$$

One observes the divergent $\tan$-terms in the numerator, and that all the other terms remain bounded and of order 1. To verify whether or not $\tan\vartheta\cdot\partial\vartheta/\partial x$ diverges for $\vartheta\to\frac{\pi}{2}$ requires a more detailed investigation.

First of all, we note that the following relation holds:

$$\tan\vartheta\,\frac{\partial\vartheta}{\partial x} = \cos\vartheta\,\frac{\partial}{\partial x}\left(\frac{1}{\cos\vartheta}\right)\,. \quad (4.23)$$

Considering the discrete approximation to the differential, $\frac{\partial\cdot}{\partial x}\doteq\frac{\Delta\cdot}{\Delta x}$, we estimate:

$$\cos\vartheta\,\frac{\partial}{\partial x}\left(\frac{1}{\cos\vartheta}\right)\doteq\cos\vartheta\,\frac{1}{\Delta x}\,\Delta\left(\frac{1}{\cos\vartheta}\right) = \\ = \cos\vartheta\,\frac{1}{\Delta x}\left(\frac{1}{\cos(\vartheta+\Delta\vartheta)} - \frac{1}{\cos\vartheta}\right) = \cos\vartheta\,\frac{1}{\Delta x}\left(\frac{1}{\cos\vartheta - \Delta\vartheta\sin\vartheta + \mathcal{O}(\Delta\vartheta^2)} - \frac{1}{\cos\vartheta}\right) = \\ = \frac{1}{\Delta x}\left(\frac{1}{1 - \Delta\vartheta\tan\vartheta + \mathcal{O}(\Delta\vartheta^2)/\cos\vartheta} - 1\right) = -\frac{1}{\Delta x} \quad \text{for } \vartheta\to\frac{\pi}{2}\,, \quad (4.24)$$

where $\Delta\vartheta = \vartheta(x+\Delta x) - \vartheta(x)$.

So replacing $\tan\vartheta\cdot\partial\vartheta/\partial x$ in eq. (4.22) by $-\frac{1}{\Delta x}$ and using again order of magnitude estimates $\Delta x\approx 10^{-6}$[m], $\bar\tau\approx 10^{7}$[Nm^{-2}], $b\approx 10^{-10}$[m] and $T=\mu b^2\approx 10^{-9}$[N], compare sec. 3.2.3, we find the limit

$$\mathrm{Pe}^*\to\frac{\Delta x\,|10^{-3} + 10^{-9}(-1/\Delta x - 1/\Delta x)|}{10^{-9}} = 1 \quad \text{for } \vartheta\to\frac{\pi}{2}\,. \quad (4.25)$$

Here we used the experience we made in calculations that $\partial\vartheta/\partial x$ remains bounded and even approaches the value 0 as $\vartheta\to\frac{\pi}{2}$, allowing for the limit

$$\cos\vartheta\sin\vartheta\frac{\partial\vartheta}{\partial x} = 0 \quad \text{for } \vartheta\to\frac{\pi}{2}\,. \quad (4.26)$$

This shows that even for the worst case, $\vartheta \to \frac{\pi}{2}$, we have no convection dominance in the enhanced model.
Choosing $\tilde{D}^* = \mu b$ one actually assumes a rather high back stress, but numerical calculations show that the convection-dominated character of the problem is accordingly reduced using the orientation dependent factor $D(\psi)$ for the definition of the back stress, too.
Note that this result is based on the disregard of the yield stress. Thus strictly speaking it is significant only for small dislocation densities, a fact which will be further examined in the following section.

4.3.4 Comparison of the short-range stress concepts: Taylor relation vs. back stress

As a closing to this chapter we will compare the two considered sources of short-range stresses between dislocations, the Taylor relation, providing the yield stress, and the back stress. We will show, that the two concepts can be considered as complementary, being dominant either for comparatively high respectively low initial dislocation densities. Thus actually both of them should be contained in the continuum dislocation-based model in order to be reasonably close to reality.
Let us again consider the simple problem of dislocation loops expanding in a narrow channel of width H under the effect of a constant applied shear stress $\bar{\tau}$. Now both the yield stress $\hat{\tau} = \alpha\mu b\sqrt{\varrho_{\mathrm{t}}}$, based on the current value of the evolved dislocation density, and the back stress τ_{b} eq. (4.4), calculated with the orientation dependent factor $D(\psi)$ according to eq. (4.17), are taken into account.
In figure 4.6 we oppose the yield and back stress acting in the numerically calculated relaxed state of the loaded channel for different initial dislocation densities. Figure 4.6(a) reflects the spatial influence of the stresses. Both back stress and yield stress grow in the vicinity of the channel walls, $x = 0$ and 1μm. For a low initial dislocation density (dashed lines), here for example $\bar{\varrho}_{\mathrm{t}} = 10^{11}\mathrm{m}^{-2}$, a pronounced slope of the back stress towards the walls is revealed, while the yield stress due to the Taylor relation remains on a low level. In contrast we find for the high dislocation density $\bar{\varrho}_{\mathrm{t}} = 10^{13}\mathrm{m}^{-2}$ hardly any back stress but a yield stress at an overall high level. Note that the back stress is equal to zero in the center of the channel, where the dislocation remains of screw type and where no (density-)gradients in perpendicular direction to the dislocation line arise. This indicates that a continuum model that would treat the dislocation population as completely homogeneous could not account for a back stress at all.
In the depiction of the mean values of both stress fields in figure 4.6(b) it is once more distinct, that they develop contrarily with respect to the initial dislocation density: while the yield stress is dominant for high dislocation densities, it is surmounted by the back stress in the case of a comparatively small number of dislocations gliding in the channel. In this spirit we consider the model that neglects the influence of the back stress as a valid extreme for high dislocation densities. In return one might neglect the contribution from the Taylor relation for small initial dislocation densities, which affirms the approach in the previous sections.

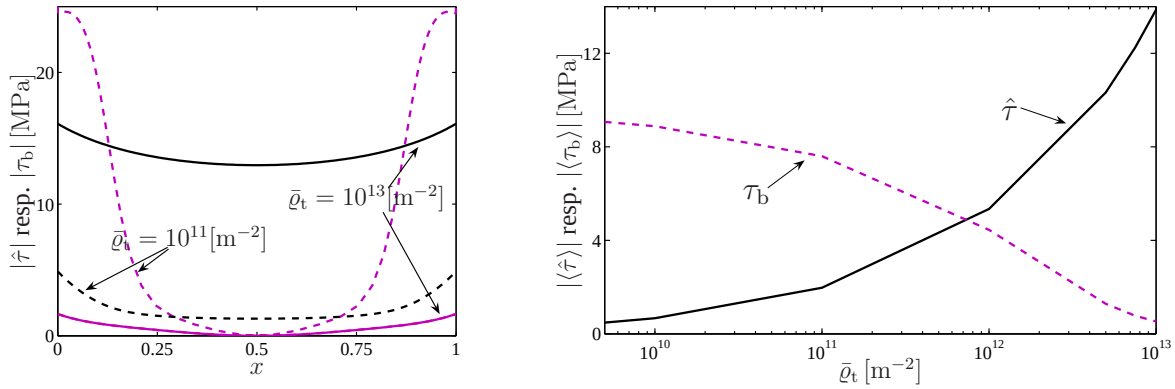

(a) Spatial distribution of Taylor and back stress for initial dislocation densities $\bar{\varrho}_\mathrm{t} = 10^{11}$ and $10^{13}\mathrm{m}^{-2}$. Note that the back stress vanishes in the centre of the channel where $\vartheta = 0$.

(b) Development of the mean Taylor resp. back stress with the initial dislocation density in a logarithmic scale

Figure 4.6: Comparison of yield and back stress in the relaxed state of the loaded channel. The depicted results are based on parameters $\bar{\tau} = 30\mathrm{MPa}$, $\hat{\tau} = 0.4\mu b\sqrt{\varrho_\mathrm{t}}$, $H = 1\mu\mathrm{m}$, $\mu = 40\mathrm{GPa}$, $\nu = 0.33$ and $b = 0.256\mathrm{nm}$.

With figure 4.7 we try to elucidate this observation from another perspective. It shows the actual shape of a bowed dislocation line in the relaxed state. The variable φ_y embodies the displacement of a representative dislocation of the considered field from its initial configuration, which was chosen as a straight line. Dislocations present in the channel reach the relaxed state when resolved shear stress, here equivalent to the applied constant shear stress $\bar{\tau}$, yield stress $\hat{\tau}$, back stress τ_b and dislocation self force $T\kappa$ compensate each other, eq. (4.6). In the case of a high initial dislocation density $\bar{\varrho}$, the yield stress is already very high at the beginning of the relaxation process, thus requiring a smaller amount of glide resp. bowing out of the dislocations to provide balance. The back stress in the present simple arrangement is related only to the dislocation orientation ϑ, eq. (4.15), that is the degree of bow-out of the individual dislocations, and thus accordingly low. Reverse reasoning explains the effect for a small initial dislocation density. The curve based on $\varrho = 10^{11}\mathrm{m}^{-2}$ is bowed out the most. The detachment of the curve from the channel boundaries, $x = 0, 1\mu\mathrm{m}$, can be identified with the formation of pile-ups against these boundaries.

A substantiated affirmation of our choice for the back stress could be supplied by some 3D dislocation dynamics simulations. For future calculations, an orientation dependent factor $D(\psi)$ similar to eq. (4.17), but adjusted to the particular dislocation fields, will be considered.

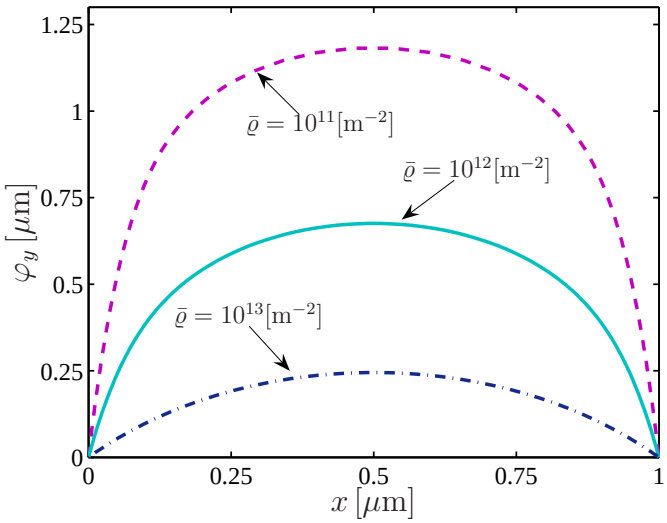

Figure 4.7: Displacement of a representative dislocation line from its initially straight configuration. For small dislocation densities, dislocations have to bow out stronger in order to reach the equilibrium, thus facing a larger amount of back stress. The depicted results are based on parameters $\bar{\tau} = 30\mathrm{MPa}$, $\hat{\tau} = 0.4\mu b\sqrt{\varrho_\mathrm{t}}$, $H = 1\mu\mathrm{m}$, $\mu = 40\mathrm{GPa}$, $\nu = 0.33$ and $b = 0.256\mathrm{nm}$.

CHAPTER 5

Application of the enhanced model

The model as presented in the first part of the thesis has already been applied to various problems: shearing of a thin crystalline strip [76], see below, bending of free-standing strips [81, 82], tension of a thin film [94], plastic deformation of a simple composite structure [118], expanding dislocation loops [96], internal stresses in dislocation cell structures [127], and a two-phase laminate structure, for which a comparison to the Cosserat continuum [41, 42] was made. It is not the intention of this chapter to recapitulate all these. For the sake of completeness only, the model problem of shearing of a thin crystalline strip, on which most of the presented pictures are based, is resumed. The investigations on the so-called source-shortening, presented in [118], are subsumed, and we discuss the effect of the introduction of the back stress on these results.

5.1 Shearing of a thin crystalline strip

Shearing of a thin crystalline strip has become the benchmark problem for the different models of microscale plasticity. It was first posed by Shu et al. [23], later addressed for example by Cleveringa [128], Bassani [18] and Yefimov [24], and has been solved in its reduced form, see 5.1.2, with the present model in [76]. However, for the reader's convenience, the problem is briefly reviewed.

5.1.1 Posing the two-dimensional problem

The simple shear of a thin crystalline strip can be modelled as a plane strain problem. Assume that the deformation is homogeneous in the x_3-direction. The normal of the strip, which has thickness H, coincides with the x_2-direction, and a shear load is applied in the x_1-direction, see figure 5.1.

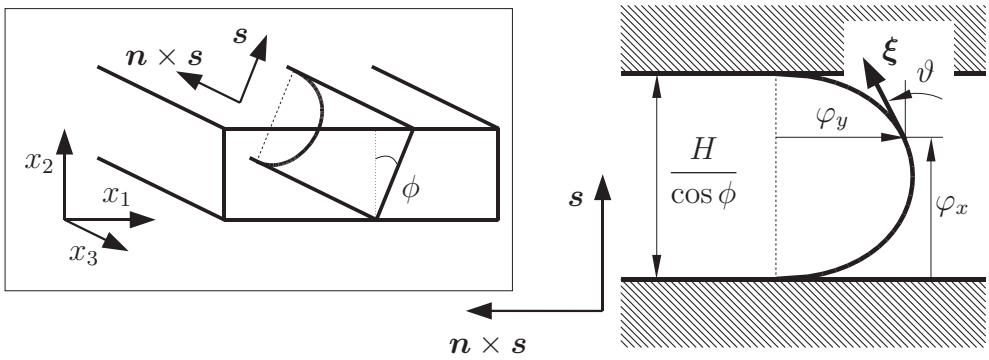

Figure 5.1: The problem setting for the simple shear of a thin crystalline strip, see also figure 3.1: a single-slip system in a constrained strip is drawn in the left part of the figure and is zoomed-in in the right part; the depicted variables have already been introduced. A shear load resp. displacement in x_1-direction is prescribed at the top of the strip, $x_2 = H$. The lower boundary is fixed.

The deformation is considered as strain-driven, i.e. a shear strain $\Gamma \hat{=} \epsilon_{12}^{\max}$ is applied at the surface $x_2 = H$. No displacement u_1 in the x_1-direction is allowed at the bottom of the strip $x_2 = 0$. A displacement u_2 in the x_2-direction is forbidden at both top and bottom of the film. One or more slip systems can be considered, each characterised by the angle enclosed by the slip direction and the x_2-direction, see section 3.1. Here we want to model symmetric double-slip, thus assuming two slip systems with $\phi := \phi^{(1)} = -\phi^{(2)}$. On each of them, initially two dislocation fields of opposite sign are introduced, characterised by the equally distributed total constant dislocation density $\varrho(x_2) = \bar{\varrho}$[1] and by the straight configuration $\gamma^{\mathrm{p}}(x_2) = 0$. Both fields are going to behave symmetrically, such that only the evolution of one of them needs to be calculated, see the first separation method presented in section 2.5.1. The strip surface is supposed to be impenetrable for dislocations. Using the stationary approach, table 3.2, this is in the subcritical case expressed by the conditions $\gamma^{\mathrm{p}}(0) = \gamma^{\mathrm{p}}(H) = 0$ for the plastic slip. For the dynamic formulation the condition $v(0) = v(H) = 0$ accounts for the boundary conditions. These initial and boundary conditions complete the continuum dislocation based model summarised in sections 2.4.5, 3.1 and 3.2.1.

A typical result for the plastic slip from a two-dimensional computation of this problem according to chapter 3 is presented in figure 5.2.

5.1.2 Reduction to one dimension

For the prescribed boundary conditions, we find without loss of generality that the strip deforms homogeneously with respect to x_1. Therefore, the problem can be reduced to one dimension, all variables depending on x_2 only. In the case of shearing under symmetric double-slip assumption, where on both slip systems the same plastic slip results, i.e. $\gamma^{\mathrm{p}} := \gamma^{\mathrm{p}(1)} = \gamma^{\mathrm{p}(2)}$, the mechanical

[1] The given value of ϱ describes the total number of dislocations on all considered slip systems. So one of the dislocation fields on one of the two slip systems considered in double-slip is characterised by the density $\bar{\varrho}/4$.

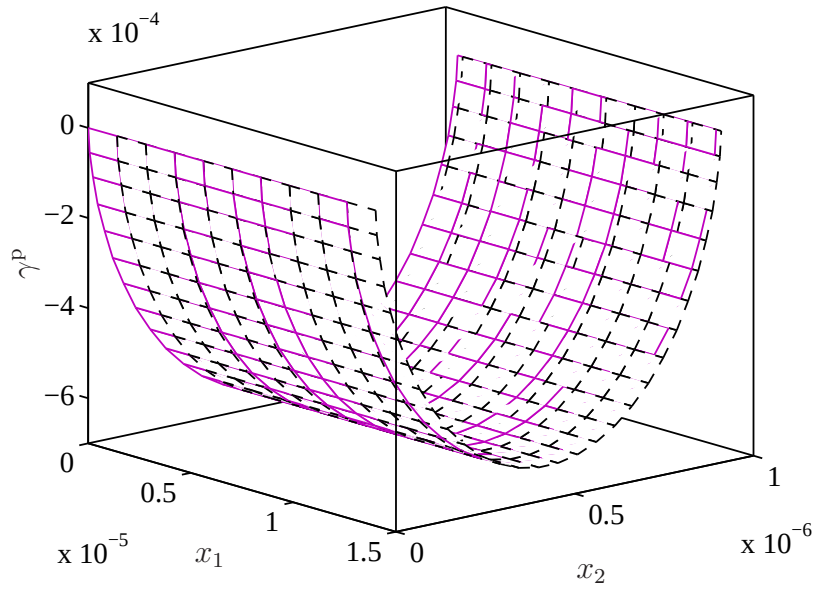

Figure 5.2: Typical profile of plastic slip as resulting from the two-dimensional computation of the shearing problem under the assumption of symmetric double-slip with MATLAB. Both slip systems as introduced for the discretisation for the Lagrangian method are indicated, one with solid (magenta) lines, and one with dashed (black) lines. The meshes overlap and partially cover each other.

part of the problem reduces to [76]

$$u_1'' = -2\gamma^{\mathrm{p}\prime}\cos(2\phi) \quad \text{with} \quad u_1(0) = 0,\ u_1(H) = \Gamma H\,. \tag{5.1}$$

The prime denotes the derivative with respect to the x_2-direction.
From the displacement we find the effective shear stress in the slip planes:

$$\tau = -\mu\left[u_1' + 2\gamma^{\mathrm{p}}\cos(2\phi)\right]\cos(2\phi)\,. \tag{5.2}$$

Analytic solution

A combination of eqs. (5.1) and (5.2) shows that the shear stress is homogeneous, that is $\tau' = 0$. If one approximates the yield stress using the constant initial dislocation density, $\hat{\tau} = \hat{\tau}_{\mathrm{ref}} = \alpha\mu b\sqrt{\bar{\varrho}}$, this enables one to analytically calculate the quasistatic solution, table 3.2, for this special problem. Using $\frac{\partial\,\cdot}{\partial x_1} = 0$ we find $-\operatorname{div}\boldsymbol{\nu} = \frac{\partial}{\partial x_2}(\cos\phi\sin\vartheta)$, which provides the solution for the orientation ϑ:

$$\kappa = \cos\phi(\sin\vartheta)' = -\frac{\tau-\hat{\tau}}{\mu b} =: -\frac{\tau_{\mathrm{eff}}}{\mu b} \quad \Rightarrow \quad \vartheta(x_2) = \arcsin\left(\frac{\tau_{\mathrm{eff}}}{\mu b\cos\phi}\left(\frac{H}{2}-x_2\right)\right)\,. \tag{5.3}$$

Given the orientation at the surfaces of the strip, $-\pi/2 < \beta = \vartheta(0) = -\vartheta(H) < 0$, and using $\vartheta(H/2) = 0$, we find

$$\tau = \tau_{\mathrm{eff}} + \hat{\tau} = \frac{2\mu b\sin\beta\cos\phi}{H} + \hat{\tau}\,. \tag{5.4}$$

From geometrical considerations within the slip plane, table 3.2, we find the differential equation for the plastic slip,

$$\gamma^{\mathrm{p}\prime} = \frac{b\bar{\varrho}}{2\cos\phi}\tan\vartheta\,, \qquad \gamma^{\mathrm{p}}(0) = 0\,, \tag{5.5}$$

where $\bar{\varrho}/2$ is the initial dislocation density on one slip system.
When the dislocations are critically bowed out, i.e. $\vartheta \to \pi/2$ at the interface, the effective shear stress and the shape of the dislocations doesn't change anymore upon increasing deformation, but the dislocations glide in the channel. This is what we call a supercritical configuration of the representative dislocation. So for τ and ϑ, the recently derived solution using $\beta = -\pi/2$ is true:

$$\tau_{\mathrm{eff}} = -\frac{2\mu b\cos\phi}{H}\,, \qquad \vartheta(x_2) = \arcsin\left(\frac{2}{H}\left(\frac{H}{2} - x_2\right)\right) \tag{5.6}$$

Based on the displacement, resulting as the solution to the boundary value problem

$$u_1'' = -\frac{2\cos(2\phi)\, b\bar{\varrho}}{2\cos\phi}\tan\vartheta\,, \quad u_1(0) = 0, u_1(H) = \Gamma H\,, \tag{5.7}$$

finally the plastic shear is given as

$$\gamma^{\mathrm{p}} = \left(-\frac{\tau}{\mu\cos(2\phi)} - u_1'\right)/(2\cos 2\phi)\,. \tag{5.8}$$

This analytic solution has been used to check the quality of numerical computations, see for example [97, 118].

Remark 5.1: The numerical solution of the presented one-dimensional reduction of the shearing problem involves the solution of the boundary value problem for the mechanical part eq. (5.1). There are a number of elaborate techniques like for example shooting methods, collocation method or discretisation of the problem by Finite Differences. Disregarding the boundary effects, the simplest and most accurate solution was found by the FD method used within the Eulerian approach. Note that FD based on the non-equidistant grid resulting from the dislocation-Lagrangian method yields a non-constant resolved shear stress τ, figure 5.3, resulting in a slightly deviant solution for the plastic slip, see also figure 3.3. This is due to the varying order of approximation provided by the Finite Difference operator along the strip: for an equidistant mesh, the Taylor-expansion of the approximation error starts with a term in h^2, yielding order $\mathcal{O}(h^2)$, whereas the error related to an approximation based on non-equidistantly distributed nodes starts with a term $h_n - h_{n-1}$, thus being of order $\mathcal{O}(h)$. The exact quality of approximation in the latter case depends on the actual node distribution and thus varies along the strip.
For high-accuracy solutions in the sub-critical region or when a back stress is considered, the Eulerian approach is therefore favourable.

With the application of the continuum dislocation-based model to the shearing problem it was observed that the model in its classical version, that is without consideration of a back stress, can provide an explanation for the source-shortening effect observed in composite materials. The following section recapitulates the results published in [118].

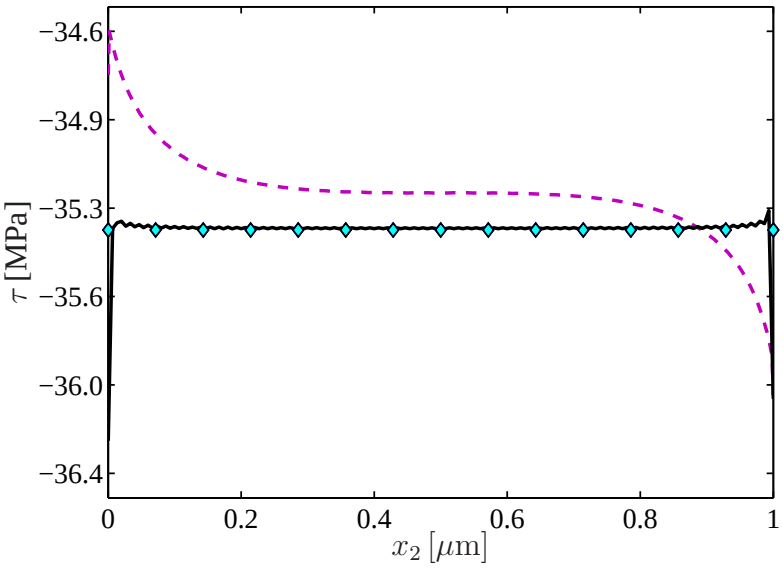

Figure 5.3: Confrontation of the resolved shear stress in the one-dimensional shearing example calculated based on the analytic solution (diamond markers), based on FD on an equidistant mesh (black, solid line) and on FD on a non-equidistant mesh resulting from the dislocation-Lagrangian method (magenta, dashed lines). $\mu = 40\text{GPa}$, $b = 0.256\text{nm}$, $\varrho = 2 \cdot 10^{13}\text{m}^{-2}$, $H = 1\mu\text{m}$, $\phi = \pi/6$, $\Gamma = 0.26\%$.

5.2 Source-shortening

The work hardening behaviour of plastically non-homogeneous materials, such as composites and two-phase alloys has been intensively studied in the seventies. It has been observed that the work hardening rate in these materials is higher than estimated from simple theoretical models based on the forest hardening. In this context, Ashby [88] has introduced the term 'geometrically necessary dislocations' to account for the dislocations related to the mesoscopic gradients of plastic deformation in the plastically non-homogeneous materials. Being deposited in the vicinity of the inclusions in addition to the usual 'statistically stored' ones, these dislocations have been suggested to increase the work hardening of the composite materials. Another analysis of the work hardening in composites has been presented later by Brown and Clarke [129]. These authors have suggested three contributions to the flow stress: (i) the mean internal stress in the matrix which can be estimated using the Eshelby and Tanaka-Mori approaches, (ii) the usual forest contribution, and (iii) the so called 'source-shortening' term. The latter has been explained as the effect of the Orowan loops around the inclusions left behind by glide dislocations. The local stresses due to the Orowan loops reduce the effective inclusion spacing by causing the successive dislocations to stand off the fibres, thus increasing the dislocation bowing stress above the Orowan stress. Recent three-dimensional discrete dislocation dynamics simulations of the plastic deformation of a composite material have shown that, in a plastic channel between impenetrable inclusions, (i) dislocations of one sign accumulate at each interface in the vicinity of the inclusions ('polarisation'), and (ii) the resolved shear stress (including the stresses of

the individual dislocations) effectively closes up the channel as the deformation proceeds [28]. This is in accord with the experiments of Prantl et al. [130] on fibre-reinforced aluminium, who observed very high dislocation densities and strain gradients in the vicinity of the fibres, figure 5.4. The mechanical characteristics of the composite can be reproduced by models only if an increased hardening is assumed [131]. An unpublished length-scale independent ad-hoc modelling of this composite confirmed, that the extraordinary high strength in transversal direction to the fibres can for instance be explained by a region of increased hardening surrounding the fibres.

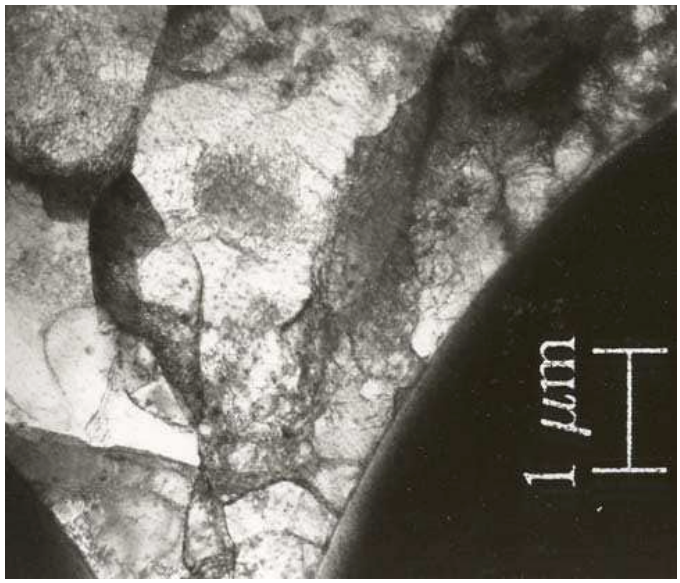

Figure 5.4: Transmission Electron Microscope picture of the aluminium composite examined in [131]. The fibre sections are shown as the dark circle segments in the lower corners. The small dislocation cells close to the fibres indicate a very high dislocation density in the vicinity of the aluminium-fibre interfaces compared to the interior of the matrix. (Previously unpublished figure)

The present non-local continuum dislocation-based model allows us to relate the above theoretical, computational and experimental results and to reconsider them from a common perspective. Consider the shearing of the thin strip first. In the calculations presented in section 5.1, the flow stress has been computed from the initial reference dislocation density: $\hat{\tau} = \hat{\tau}_{\text{ref}} = \alpha\mu b\sqrt{\bar{\varrho}}$. This was only to enable the calculation of the analytic solution. However, due to the bowing-out of the initially straight dislocations, the current density locally grows, see equation (3.6), especially in the vicinity of the impenetrable edges of the strip. If the flow stress is computed according to $\hat{\tau} = \hat{\tau}_{\text{curr}} = \alpha\mu b\sqrt{\varrho}$, that is based on the current density, the storage of geometrically necessary dislocations as well as the source-shortening effect are accounted for by the model. This is because in this way, the mutual short-range interactions between dislocations are approximately taken into account.

The increase in dislocation density $\varrho(x_2)$ goes along with gradients of plastic strain, see the shear strain profiles in figure 5.5(a). The edge content of the originally straight screw dislocations thus corresponds to the geometrically necessary dislocations of Ashby [88], see also Nye [46], which can be computed using the continuum theory of dislocations [83]. This geometrically necessary

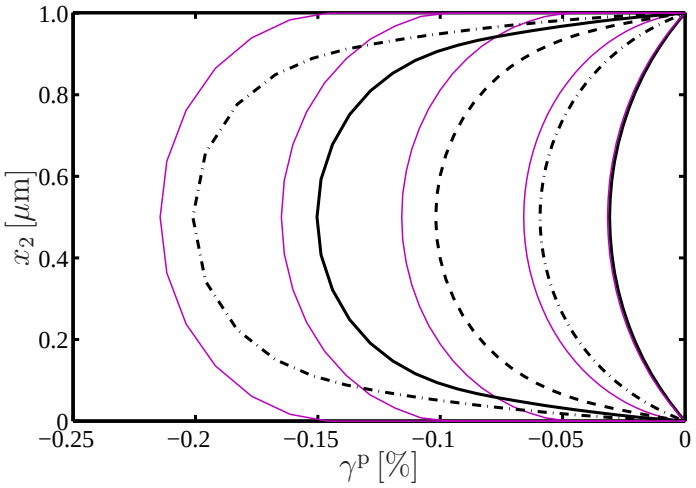

(a) The plastic shear profile for the 'reference' (magenta, thin lines), and for the 'current' yield stress for different applied shear, see the legend in subfigure (b). In the case of the 'current' yield stress, the dislocations stand off the interface.

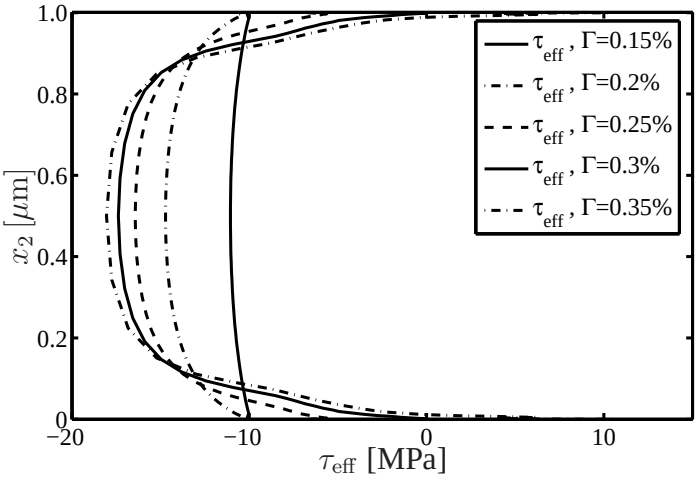

(b) The profile of the effective shear stress $\tau(x_2) - \hat{\tau}(x_2)$ in the case of the 'current' yield stress is depicted. As described in [28], the channels close up during increased straining, as the absolute value of the effective shear stress progressively decreases in the vicinity of the interface, up to a change in sign.

Figure 5.5: The source-shortening effect. The presented results are based on a double-slip assumption with parameters $\phi = \pm 30$, $\mu = 26.3$ GPa, $b = 0.25$ nm, $\nu = 0.33$ and $\bar{\varrho} = 10^{13}\mathrm{m}^{-2}$.

density is polarised in the sense of [28], since edge dislocation content of one sign concentrates in the vicinity of each interface. We also noted that in a local model (that is without an internal length-scale), the geometrically necessary dislocation density would collapse to a surface density related to steps in plastic deformation at the interfaces, cf. Mughrabi [132] and the discussion

in [76], so there would be no source-shortening. However, in the present non-local model, the locally varying density enters the Taylor formula for the flow stress $\hat{\tau} = \hat{\tau}_{\mathrm{curr}}$, so the material near the interface becomes harder, cf. the experimental results in [131]. The edge dislocation content deposited along the infinitely extended interface corresponds to the Orowan loops around finite inclusions. As it can be inferred from figure 5.5(a), the dislocations stay off the interfaces, so that the strip thickness is effectively reduced. Note that the profile of plastic shear is directly related to the shape of a representative bowed-out dislocation (2.83). The increase in flow stress near the interfaces also influences the profile of the effective stress $\tau(x_2) - \hat{\tau}(x_2)$ that drives the dislocation motion, see figure 5.5(b). As the channel effectively becomes narrower, the bowing stress necessary to sustain the dislocation motion increases. Accordingly, the source-shortening effect is reflected in the corresponding stress-strain curve that reveals enhanced hardening, figure 5.6. In the case of the 'reference' flow stress the stress saturates at $\hat{\tau}_{\mathrm{ref}}$ augmented by the Orowan stress, cf. [76]. In the case of the 'current' flow stress the hardening continues, in accordance with the source-shortening effect.

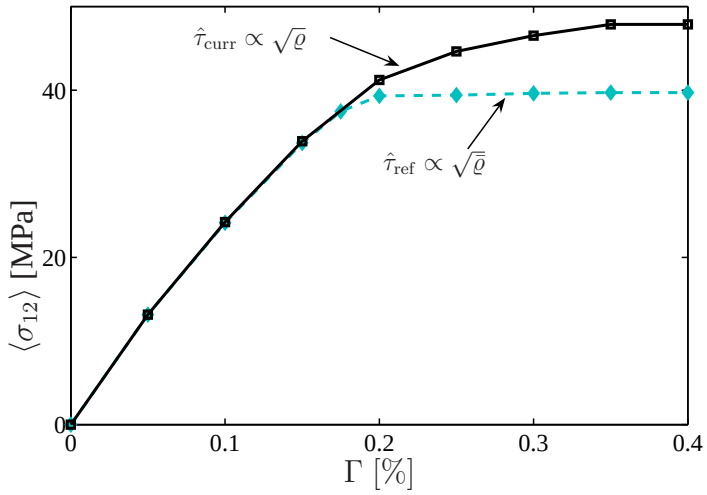

Figure 5.6: The source-shortening effect expressed in stress-strain-curves. For calculations with the 'reference' yield stress, the stress saturates at a shear of approximately $\Gamma = 0.2\%$ at a level of the 'reference' yield stress augmented by the Orowan stress, while for the calculations based upon the 'current' yield stress, the mean shear stress grows beyond that point, and saturates much later and slower.

Calculations on the composite structure introduced in section 3.4.3 were performed, too, but only for quite small deformations where the source-shortening due to the concentration of dislocations at the matrix-particle interfaces has not yet a marked effect on the results. Nevertheless, the origin of the source-shortening effect is already evident in the presented calculation, cf. figure 5.7. Dislocations accumulate at the boundaries to the reinforcement particles, such that the yield stress increases according to $\hat{\tau}_{\mathrm{curr}} = \alpha \mu b \sqrt{\varrho}$. Figure 3 in [28] shows the same effect in the results of the discrete-dislocation simulations.

The mean matrix stress, which is actually a compatibility stress, is captured by the rigorous continuum-mechanics framework of the model.

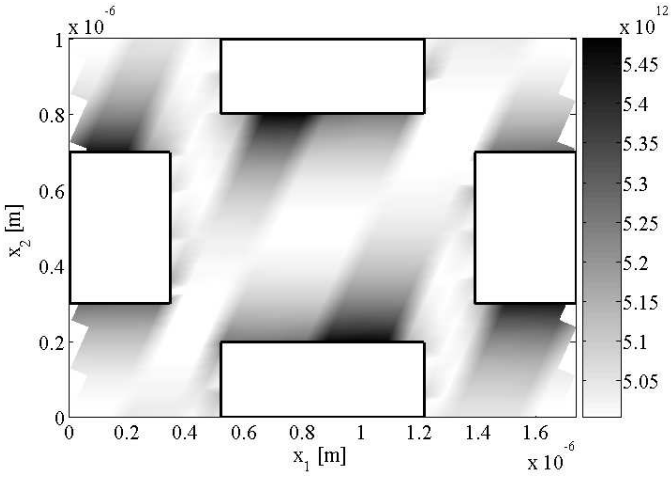

Figure 5.7: Distribution of the dislocation density in the composite structure, introduced in section 3.4.3 A concentration of dislocations at the interfaces between the hard and soft phases is evident: the darker the colouring, the higher is the dislocation density. Note that the rectangular reinforcement particles are completely dislocation free.The colorbar to the right of the picture relate the gray scale value to the value of the dislocation density.

5.3 The impact of the back stress on the source-shortening

In section 5.2 it was shown, that the classical continuum dislocation-based model can provide a very simple explanation for the source-shortening effect observed in composite structures. As was already mentioned, this effect is normally ascribed to the formation of pile-ups by Orowan loops left behind around reinforcement particles of a composite by passing dislocations [129]. These pile-ups effectively narrow the channel for subsequent dislocations. In terms of the present enhanced model this means, that the back stress rather than the 'current' yield stress is supposed to be the primary cause for a source shortening effect.

However, the results in section 4.3.4 suggest that neither the effect represented by the Taylor relation based on the current dislocation density, nor the contribution of the pile-ups must be ignored. Especially in the case of high dislocation densities the effect of a local yield stress for moderate loading even surmounts that of the back stress, figure 4.6. On the other hand, for low dislocation densities, the back stress, which in our model depends directly only on the dislocation shape, not on the absolute value of the the dislocation density, eq. (4.15), is the major source of the local hardening.

Reconsidering the case investigated in section 5.2, but now taking into account the effect of the back stress, we find that indeed both stress fields have comparable influence on the results.

In figure 5.8 we show parts of figure 5.5 plus the corresponding results for an additional consideration of the back stress. The retardation of the plastic deformation is virtually doubled in the considered case.

Figure 5.9 compares the stress-strain response for the sheared film of thickness $H = 1\mu$m for two different initial dislocation densities according to three different approaches: (*i*) considering

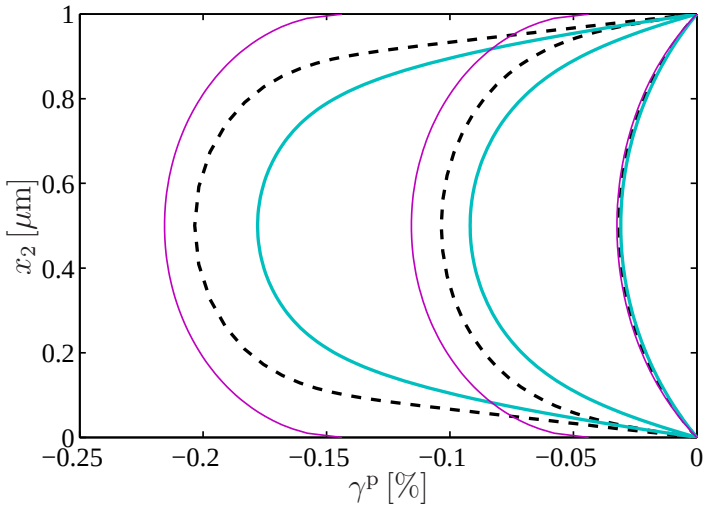

Figure 5.8: The source-shortening effect. The plastic shear profile for the 'reference' (magenta, thin solid lines), for only the 'current' yield stress considered (black, dashed lines) and for both 'current' yield stress and back stress considered (cyan, thick solid lines) are confronted. As in completion of figure 5.5 a third quantity is depicted, only three different values for the applied shear were used, namely $\Gamma = \{0.15, 0.25, 0.35\}\%$. For the considered initial dislocation density $\bar{\varrho} = 10^{13}\mathrm{m}^{-2}$, the effects of the Taylor-type interactions and of the back stress are comparably strong. The presented results are based on parameters values $\phi = \pm 30$, $\mu = 26.3$ GPa, $b = 0.25$ nm, and $\nu = 0.33$. For the spatial discretisation, at least 150 nodes were used.

the current yield stress as the only origin of the source-shortening (square markers), (*ii*) using the constant reference yield stress but in addition the back stress (circle markers), and (*iii*) considering both short-range stress fields (triangle markers). The complete disregard of short-range interactions like in figure 5.8 is not investigated here, as this would result in a solution that doesn't show any hardening behaviour at all. In the treated loading spectrum the underlying initial dislocation density takes a big influence on the impact each contribution may have. While for the smaller value of $\bar{\varrho} = 5 \cdot 10^{12}\mathrm{m}^{-2}$, the differences between the three cases are articulate, we can hardly distinguish the responses for $\bar{\varrho} = 5 \cdot 10^{13}\mathrm{m}^{-2}$.

These examples show, that neither the increase of the yield stress, which is local and directly related to an increase of the dislocation density, nor the back stress, which is related only to the dislocation shape, must be neglected when describing the narrowing of channels during the plastic deformation. Note that it is important to use a good approximation to the real dislocation density, as especially with respect to the short-range interactions of dislocations its value has a big effect even on the qualitative behaviour of the material.

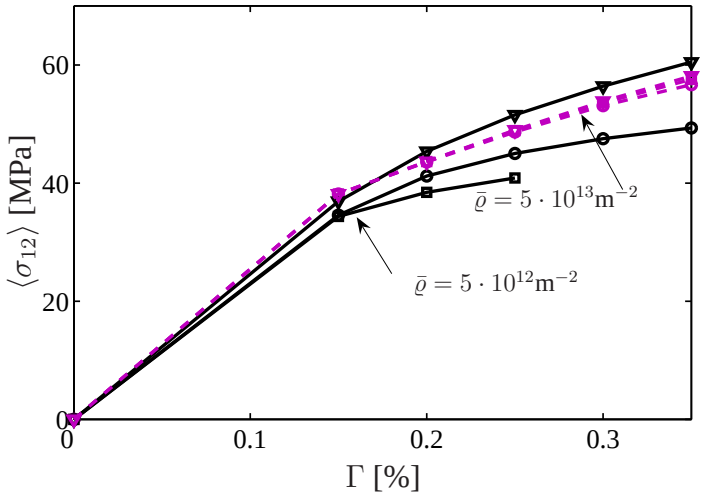

Figure 5.9: For two different densities, the stress-strain response with and without consideration of the current yield stress resp. a back stress is depicted. In each triple of curves, the square markered curve represents the response with only the current yield stress considered. The curve with circle markers is the result for a constant yield stress but a back stress taken into account. Finally the curves with the triangle markers stand for the solution when both contributions are used, which yields the hardest material response. The curves for $\bar{\varrho} = 5 \cdot 10^{13}\mathrm{m}^{-2}$, depicted as magenta dashed lines, are virtually indistinguishable. It shows again, that for decreasing dislocation density the effect of the back stress for moderate deformation makes a big difference to the predicted material response. The presented results are based on parameters values $\phi = \pm 30$, $\mu = 26.3$ GPa, $b = 0.25$ nm, and $\nu = 0.33$. For the spatial discretisation, at least 150 nodes were used.

CHAPTER 6

Summary and outlook

This thesis is concerned with the continuum dislocation-based model that was first presented by Sedláček in [70]. After a general review on the current models for plasticity on the μm-scale, that account for size effects, the set-up of the present model was resumed in chapter 2. Two issues were addressed in the remainder of the thesis:

(*i*) the numerical implementation of the continuum dislocation-based model for two-dimensional plane-strain applications with the prospect of a coupling of the material model to standard Finite Element software,

(*ii*) the enhancement of the classical model by the introduction of an additional short-range stress contribution, the back stress.

Implementation even for the very simple one-dimensional problems has revealed a difficult numerical character of the material model. The investigation of the partial differential equation system showed that a convection-dominated convection diffusion problem is faced which requires special treatment to get a stable numerical solution. Among a plenty of elaborate techniques, the Lagrangian particle tracking method was chosen as a basis for our numerical scheme. It very naturally describes the actual 'flow' of dislocation segments as the dislocation glides, thus accounting very well for the emerging boundary layers. In view of the coupling to small strain continuum mechanics, two meshes have to be organised: the first one as a basis for the Finite Element discretisation of the continuum mechanics problem is regular and constant in time, while the second mesh is bound to distinct slip planes representing a slip system, and consists of automatically redistributed nodes on this slip planes that represent the Lagrangian dislocation segments. The MATLAB implementation for simple plane strain problems was presented in detail. The aimed coupling to the Finite Element software ZeBuLoN could not be completed, as our cooperation partners had problems with the development of the required library. However the principles of such a coupling could be worked out and preliminary work has been done and was described in this work.

The enhancement of the model by an additional short-range stress field, the back stress, yielded reasonable and very interesting results. In advance of earlier approaches to introduce a back stress in deterministic continuum models the relative orientation of interacting dislocations was considered for the actual strength of the back stress. In view of its effect on the interpretation of the source-shortening, we consider both back stress and the Taylor relation for the yield stress as non-negligible contributions to the short-range interactions in our model. The enhanced model revealed a numerically rather good-natured behaviour. For small dislocation densities it could be shown, that the back stress counteracts the formation of the critical boundary layer and thus potentially simplifies the numerical implementation.

In the near future a number of issues are pending: besides the coupling to ZeBuLoN, a detailed investigation of the unloading/cyclic behaviour of the model with regard to the prediction of the Bauschinger effect is on the list.

Moreover, we intend to incorporate an algorithm for an optimal redistribution of the nodes during the integration of the model by the Lagrangian method. It has been developed in the group of Prof. M. Beneš in Prague, and is already successfully used by the group of our collaborator Prof. J. Kratochvíl.

Part III

Appendices

APPENDIX A

Frequently used symbols

The following tabular provides a collection of frequently used symbols.

Greek and fraktur symbols

∇	Nabla operator, for example $(\frac{\partial}{\partial x}, \frac{\partial}{\partial y}, \frac{\partial}{\partial z})$
$\boldsymbol{\alpha}$	Kröner's dislocation density tensor
α	constant factor (in yield stress resp. strain energy)
$\boldsymbol{\beta}$	distortion tensor: $\boldsymbol{\beta} = \nabla \boldsymbol{u}$
$\boldsymbol{\beta}^{\mathrm{e}}, \boldsymbol{\beta}^{\mathrm{p}}$	elastic and plastic part of distortion tensor
$\boldsymbol{\epsilon}, \boldsymbol{\epsilon}_V$	strain or deformation tensor resp. vector in Voigt notation
$\boldsymbol{\epsilon}^{\mathrm{e}}, \boldsymbol{\epsilon}^{\mathrm{p}}$	elastic and plastic part of strain tensor
γ^{p}	plastic slip
$\boldsymbol{\kappa}$	dislocation line curvature
$\boldsymbol{\lambda}$	vector of Lagrangian multipliers
$\mathfrak{L}$	tangent to a lifted curve in the space SM
μ	elastic shear modulus
ν	Poisson number
$\boldsymbol{\nu}$	unit normal to dislocation line
$\boldsymbol{\omega}$	tensor of material rotation
$\boldsymbol{\omega}^{\mathrm{e}}, \boldsymbol{\omega}^{\mathrm{p}}$	elastic and plastic part of rotation tensor
ϕ	inclination angle characterising the slip system (except for section 2.5, where ϕ is a generalised density measure)
$\boldsymbol{\varphi}$	parametric curve, describing a dislocation line
$\mathfrak{p}$	mapping defining the lift of a curve in the space SM
$\boldsymbol{\varrho}, \varrho$	scalar dislocation density (as vector oriented in $\boldsymbol{\xi}$-direction)
$\bar{\varrho}$	constant initial dislocation density

$\hat{\varrho}$	average dislocation density as reference for τ_b
$\mathfrak{S}$	total length of a (dislocation) line
$\mathfrak{s}$	arc length of a (dislocation) line
$\mathrm{d}\mathfrak{s}$	length of line element
$\boldsymbol{\sigma}, \boldsymbol{\sigma}_V, \sigma$	stress (tensor, vector in Voigt notation or scalar)
τ	(resolved) shear stress
τ_b	back stress resp. pile-up stress
$\hat{\tau}$	yield stress
$\hat{\tau}_\mathrm{curr}$	yield stress based on current dislocation density
$\hat{\tau}_\mathrm{ref}$	yield stress based on initial dislocation density
ϑ	dislocation line orientation
$\boldsymbol{\xi}$	unit tangent to dislocation line

Further symbols

$\mathrm{d}\boldsymbol{a}$	normal to (small) surface element
A	a surface
$\boldsymbol{b}, b$	Burgers vector (vector or magnitude)
B	drag coefficient
C	closed curve
$\boldsymbol{C}$	elastic stiffness tensor
D	coefficient in pile-up stress definition
$\boldsymbol{e}_1, \boldsymbol{e}_2, \boldsymbol{e}_3$	unit vectors of global coordinate system
$\boldsymbol{e}_x, \boldsymbol{e}_y, \boldsymbol{e}_z$	unit vectors of slip system coordinate system
H, L	height and length of the considered sample/film
$\boldsymbol{K}$	stiffness matrix in Finite Element discretisation
$\boldsymbol{L}$	material distortion rate $\boldsymbol{L} = \partial\boldsymbol{\beta}/\partial t$
$\mathrm{d}\boldsymbol{l}$	oriented line element (of a curve f. ex.)
$\boldsymbol{n}$	slip plane normal
Pe	Péclet number
$\boldsymbol{s}$	slip direction
t	time
T	line tension
$\boldsymbol{u}$	spatial displacement: $\boldsymbol{u} = (u_1, u_2, u_3)$
V	volume
$\boldsymbol{v}, v$	velocity (vector or magnitude)
v	generalised velocity field (section 2.5.2)
w_1, w_2	ansatz or trial function for Finite Elements

W_{el}	elastic strain energy of a dislocation
W_{F}	energy of interaction of a dislocation with a stress field ($\leftrightarrow$ Peach-Koehler force)
W_{G}	Gibbs free energy
W_{S}	line energy ($\leftrightarrow$ dislocation self force)
$\boldsymbol{x}$	point in space (i.e. (x, y, z) or (x_1, x_2, x_3))
x_{1i}^0	root points of discrete slip planes, section 3.4
x_1, x_2, x_3	global coordinates
x, y, z	coordinates of slip plane system

APPENDIX B

Mathematical relations

Throughout the thesis, scalar variables are in normal font, while vectors, matrices and tensors are set boldface. The scalar product is expressed in a minimalist way by the $\cdot$ operator.
Differentials of a scalar function a resp. a field $\boldsymbol{v}$ of one (spatial) variable, e.g. s, are denoted $\mathrm{d}a/\,\mathrm{d}s$ resp. $\mathrm{d}\boldsymbol{v}/\,\mathrm{d}s$ or, if unambiguous, abbreviated by a prime, that is e.g. a'. The gradient of a function / field of multiple variables, e.g. (x, y, z), is either explicitly written as $\mathrm{grad}\,(\,)$ or abbreviated using the nabla operator $\nabla := \left(\frac{\partial}{\partial x}, \frac{\partial}{\partial y}, \frac{\partial}{\partial z}\right)$. Accordingly directional derivatives, in for example direction $\boldsymbol{\xi}$, are denoted

$$\nabla_{\boldsymbol{\xi}} a := (\nabla a) \cdot \boldsymbol{\xi} = (\mathrm{grad}\,(a)) \cdot \boldsymbol{\xi}\,, \quad \nabla_{\boldsymbol{\xi}} \boldsymbol{v} := (\nabla \otimes \boldsymbol{v})\boldsymbol{\xi} = (\mathrm{grad}\,(\boldsymbol{v}))\boldsymbol{\xi}\,, \tag{B.1}$$

where usually the position where the gradient is evaluated is not explicitly specified. A similar notation is used for the divergence and curl operations, which are however only applicable to fields $\boldsymbol{v}$:

$$\nabla \cdot \boldsymbol{v} := \mathrm{div}\,(\boldsymbol{v})\,, \quad \nabla \times \boldsymbol{v} := \mathrm{curl}\,(\boldsymbol{v})\,. \tag{B.2}$$

Concerning the temporal derivatives we strictly distinguish between the Eulerian (partial, i.e. $\frac{\partial \cdot}{\partial t}$) and Lagrangian (total, i.e. $\mathrm{d}/\,\mathrm{d}t$) derivative. The partial derivative of a function a with respect to time t is sometimes abbreviated by a superposed dot, e.g. $\dot{a}$.

Identities

Let $\boldsymbol{v}(\boldsymbol{x})$ be a vector field on $\mathbb{R}^3$, a is a scalar valued function on $\mathbb{R}^3$.

The following identities and 'product rules' hold:

$$\mathrm{curl}\,\mathrm{grad}\,\boldsymbol{v} = \nabla \times (\nabla \otimes \boldsymbol{v}) = 0 \tag{B.3}$$

$$\mathrm{div}\,\mathrm{curl}\,\boldsymbol{v} = \nabla \cdot (\nabla \otimes \boldsymbol{v}) = 0 \tag{B.4}$$

$$\mathrm{curl}\,(a\boldsymbol{v}) = a\,\mathrm{curl}\,\boldsymbol{v} + \mathrm{grad}\,(a) \times \boldsymbol{v} \tag{B.5}$$

$$\operatorname{div}(a\boldsymbol{v}) = a \operatorname{div}\, \boldsymbol{v} + \operatorname{grad} a \cdot \boldsymbol{v} \tag{B.6}$$

$$\operatorname{grad}(ab) = a \operatorname{grad} b + b \operatorname{grad} a \tag{B.7}$$

Vectors, tensors and products

A second-order tensor $\boldsymbol{T}$ can be written as tensor product of two vectors, $\boldsymbol{p}$ and $\boldsymbol{q}$:

$$\boldsymbol{T} = \boldsymbol{p} \otimes \boldsymbol{q} \equiv T_{kl} \boldsymbol{e}_k \otimes \boldsymbol{e}_l = p_k q_l \boldsymbol{e}_k \otimes \boldsymbol{e}_l \tag{B.8}$$

The linear transformation of a vector field $\boldsymbol{v}$ by $\boldsymbol{T}$ can be performed as:

$$\boldsymbol{T}\boldsymbol{v} = (\boldsymbol{p} \otimes \boldsymbol{q})\boldsymbol{v} = \boldsymbol{p}(\boldsymbol{q} \cdot \boldsymbol{v}) \tag{B.9}$$

Note that all vectors $\boldsymbol{v}$ are transformed to vectors parallel to $\boldsymbol{p}$.

Stokes' theorem

Let C be the boundary of a surface A. Let further $\boldsymbol{v}(\boldsymbol{x})$ be a vector field, $\boldsymbol{T}(\boldsymbol{x})$ a second order tensor field. Stokes theorem states:

$$\oint_C \boldsymbol{v} \, \mathrm{d}\boldsymbol{l} = \int_A \operatorname{curl} \boldsymbol{v} \, \mathrm{d}\boldsymbol{a} \tag{B.10$_1$}$$

$$\oint_C \boldsymbol{T} \, \mathrm{d}\boldsymbol{l} = \int_A \operatorname{curl} \boldsymbol{T} \, \mathrm{d}\boldsymbol{a} \tag{B.10$_2$}$$

Gaussian Integral theorem

Let $V \subset \mathbb{R}^3$ be a compact set with piecewise smooth boundary S. Let the orientation of the boundary be given by an outward normal field $\boldsymbol{n}$. Consider a $\mathcal{C}^1$ vector field $\boldsymbol{v}$ on an open neighbourhood of V. Then it is found

$$\int_V \operatorname{div} \boldsymbol{v} \, \mathrm{d}V = \oint_S \boldsymbol{v} \cdot \boldsymbol{n} \, \mathrm{d}S \,. \tag{B.11}$$

APPENDIX C

Some useful correlations within the slip plane coordinate system

This chapter of the appendix is a supplement to section 2.4. Remember the basic assumptions:

$$\boldsymbol{e}_x = \boldsymbol{s}\,,\ \boldsymbol{e}_y = \boldsymbol{n} \times \boldsymbol{s}\,,\ \boldsymbol{e}_z = \boldsymbol{n}\,. \tag{C.1}$$

Thus unit tangent and unit normal to the dislocation line are functions of the line orientation according to

$$\boldsymbol{\xi} = \begin{pmatrix} \cos\vartheta \\ \sin\vartheta \\ 0 \end{pmatrix}\,,\ \boldsymbol{\nu} = \begin{pmatrix} -\sin\vartheta \\ \cos\vartheta \\ 0 \end{pmatrix}\,. \tag{C.2}$$

Derivatives with respect to the orientation ϑ provide:

$$\frac{\partial \boldsymbol{\xi}}{\partial \vartheta} = \boldsymbol{\nu} \tag{C.3$_1$}$$

$$\frac{\partial \boldsymbol{\nu}}{\partial \vartheta} = -\boldsymbol{\xi} \tag{C.3$_2$}$$

The divergences of line tangent and normal can be expressed as directional derivative of the orientation:

$$\operatorname{div}\boldsymbol{\xi} = \operatorname{grad}\vartheta \cdot \boldsymbol{\nu} = \nabla_{\boldsymbol{\nu}}\vartheta\,, \tag{C.4$_1$}$$

$$\operatorname{div}\boldsymbol{\nu} = -\operatorname{grad}\vartheta \cdot \boldsymbol{\xi} = -\nabla_{\boldsymbol{\xi}}\vartheta\,. \tag{C.4$_2$}$$

It is also easy to see, that

$$\operatorname{grad}\boldsymbol{\xi} = \boldsymbol{\nu} \otimes \operatorname{grad}\vartheta\,, \tag{C.5$_1$}$$

$$\operatorname{div}\boldsymbol{\nu} = -\boldsymbol{\xi} \otimes \operatorname{grad}\vartheta\,, \tag{C.5$_2$}$$

and that

$$\boldsymbol{n} \cdot \operatorname{curl}\boldsymbol{\xi} = \operatorname{grad}\vartheta \cdot \boldsymbol{\xi} = -\operatorname{div}\boldsymbol{\nu}\,, \tag{C.6$_1$}$$

$$\boldsymbol{n} \cdot \operatorname{curl}\boldsymbol{\nu} = \operatorname{grad}\vartheta \cdot \boldsymbol{\nu} = \operatorname{div}\boldsymbol{\xi}\,. \tag{C.6$_2$}$$

APPENDIX D

Technical notes on the used software

It is strongly recommended to realise the coupling of the continuum dislocation-based model with ZeBuLoN on a computer equipped with the operating system Linux. On the utilised PC, that is equipped with Debian-Linux, no serious problems with any of the subsequent software were encountered. The descriptions provided in this chapter therefore in most cases will only apply to the usage of the software tools on Linux.

D.1 ZeBuLoN

ZeBuLoN is part of the Z-set package, which includes the Z-mat material constitutive model library and the full-featured general purpose FEA solver ZeBuLoN. Recent activities have been related to the development of ZeBuLoN's testing facility, including elevated temperature, fatigue crack growth, creep and general mechanical testing capabilities.
The principal commands provided by Zset are the following:

Zmaster:	graphics interface
Zrun:	FE calculation
Zrun -S:	Simulation on volume elements
Zrun -o:	Optimisation
Zrun -pp:	Batch post-processing
Zrun -m:	Batch mesher

Amendments to the .bashrc

To get ZeBuLoN running, the `.bashrc` (according to the installation path, which here was /usr/local) has to be adjusted as follows.

```
#ZeBuLoN-related variables
export PATH=$PATH:/usr/local/Z8.3_Jul_15_2005:/usr/local/Z8.3_Jul_15_2005/bin
export Z7PATH=/usr/local/Z8.3_Jul_15_2005
```

```
export Z7LICENSE=/usr/local/Z8.3_Jul_15_2005/lib/Zebulon.zlic
source /usr/local/Z8.3_Jul_15_2005/lib/Z7_profile
#export Z7_MAX_NB_DOF=1
export Z7_TMP_DIR=/tmp/Z7
export ZEBU_PATH=/usr/local/Zeb_mM_coupling/
```

Remark D.1: Bash is the shell, or command language interpreter, for the GNU operating system. The name is an acronym for the 'Bourne-Again SHell', a pun on Stephen Bourne, the author of the direct ancestor of the current Unix shell `/bin/sh`, which appeared in the Seventh Edition Bell Labs Research version of Unix. A Unix shell is both a command interpreter, which provides the user interface to the rich set of GNU utilities, and a programming language, allowing these utilitites to be combined. When an interactive shell that is not a login shell is started, bash reads and executes commands from `/.bashrc` in the respective users home directory, provided that file exists. If it is to be read in a running shell, e.g. to updated for some modifications, one has to type

```
. ~/.bashrc
```

where the tilde refers to the user's home directory, and the leading '.' is essential. This only has effect on the shell in which it was typed! Commands in the bash are for example used to set and export PATH variables or to define abbreviations ('alias') for some shell commands.
Parts of this remark were taken from the web page [133].

ZeBuLoN-mM-coupling – the zMDC-library

At Onera a library was developed that enables a coupling of ZeBuLoN with the DD-code microMegas (mM), see also section 3.5.
The data exchanges between ZeBuLoN and mM are carried out through a parallel virtual machine, so PVM has to be installed, see below. The zMDC-library is just a plugin that adds some special objects to the main code such that not all the code is needed to do some development. Moreover, only a small share of the code has to be recompiled when something is changed or added in the library.
Having unpacked the zMDC.tar to some `Zeb_mM_coupling`-directory, in theory all that has to be done is go into the directory containing the source code (at the level where a file called 'library_files' is located), and then type `Zmake` (or `Zmake -g` for debug mode), which should generate a dynamic library called libZmdc.so (or libgZmdc.so respectively). Finally the library is introduced to ZeBuLoN by defining the environment variable `$ZEBU_PATH` pointing to the directory where `libZmdc.so` is located. In any case, if the compilation gives some error messages (always possible given the small differences between the current version and the development version which was worked with here), the people at Onera (arjen.roos@onera.fr and benoit.devincre@onera.fr) can be contacted.
Not all the files contained in the source directory are needed for the present purpose, because some of them are required only for the superposition method, wich is also implemented in the

zMDC module.

Now, in order to see whether ZeBuLoN can load the library, a simple calculation (not necessarily dislocation-related) can be run. It has to be checked whether in the very first lines of output there is a message like

```
cur 3 /home/roos/Zebulon/Z8.4/External/MDC/libgZmdc.so Done.
```

If it says `Done` at the end of the line, the library has been successfully installed. Otherwise it will say that the library could not be loaded because of... (some reason, which is usually an unresolved symbol). The main thing is that there are no error messages associated to libZmdc.so. To ensure this again, one may type `Zrun -H | grep dislocation`. This should provide a list of the objects and associated keywords coming from the libZmdc library. If it contains, for example, something similar to

```
dislocation_behavior  zMDC/Dislocation_behavior.c 0x0x7260d0
```

then it's OK.
The DD simulation is called right from within a ZeBuLoN-.inp file by the key-word `****dislocation`. This is defined in the library (in fact, there are two lines in `Static_dislocation.c`):

```
DECLARE_OBJECT(BASE_PROBLEM,PROBLEM_STATIC_MECHANICAL_DISLOCATION,dislocation)

ADD_PB_TYPE(dd,dislocation)
```

This means that there is a class called `PROBLEM_STATIC_MECHANICAL_DISLOCATION` (that derives from `BASE_PROBLEM`), that is associated to the keyword 'dislocation'. The second line says that the command line switch `-dd` (so : `Zrun -dd` + options for PVM + problem name) tells ZeBuLoN to use the class associated to the keyword 'dislocation'.

position within the zMDC-library	***what happens***	***position within the gammaplas-module***
	Initialization communication	
0 Static_dislocation.c -- open_Micromegas	Z->DD 0 spawning mM	
1 Static_dislocation.c -- load	Z->DD 1 transfer problem name	1 nom_du_probleme
2 Static_dislocation.c -- load -- send_mesh_info	Z->DD 2 transfer mesh	2 transformation_maillage
3 Static_dislocation.c -- load -- elasticity_for_dislocation	Z->DD 3 transfer elasticity matrix	3 matrice_elasticite_gauss
4 Static_dislocation.c -- load	Z->DD 4 send info on "new calculation or restart"	4 redemarrage
7 Static_dislocation.c -- execute -- make_increment	Z->DD 7 send dt_z to mM	7 increment_du_temps
	loop for time integration	
	loop for newton-procedure	
5 Dislocation_behavior.c -- get_strain_dislocation (called by the sequence: make_increment -- (Algorithm_mqn_dislocation.c -- convergence_loop) -- (Algorithm_mqn_dislocation.c -- compute_internal_reaction) -- (Mcesd_std_dislocation.c -- compute_strain_for_dislocation))	*loop over all elements* Z->DD 5 transfer increment of total deformation in Gauss points	5 increment_deformation_iteration
	DO THE DISLOCATION CALCULATION	
6 Dislocation_behavior.c -- integrate (called by the sequence: make_increment -- (Algorithm_mqn_dislocation.c -- convergence_loop) -- (Algorithm_mqn_dislocation.c -- compute_internal_reaction) -- (Mcesd_std_dislocation.c -- internal_reaction))	*loop over all elements* Z<-DD 6 transfer increment of plastic deformation in Gauss points	6 resultat_calcul
8 Algorithm_mqn_dislocation.c -- convergence_loop	Z->DD 8 information if time repeated or not	8 poursuite_calcul
9 Static_dislocation.c -- make_increment	Z->DD 9 information if calculation, i.e. time integration, is done	9 fin_calcul
7 Static_dislocation.c -- execute -- make_increment	Z->DD 7 send new dt_z to mM	7 increment_du_temps

Table D.1: Chart of the communication between ZeBuLoN and microMegas respectively the continuum dislocation-based model.

Acquisition and useful links

ZeBuLoN can be downloaded from the Northwestern Numerics homepage.

Commercial ZeBuLoN: http://www.nwnumerics.com/
Home page of microMegas: http://zig.onera.fr/mm_home_page/

This is also where a lot of documentation and examples can be found.
A free license for education and research can be obtained from the École des Mines de Paris, where a big part of the software is developed.
For licensing purposes contact e.g. farida.azzouz@ensmp.fr or samuel.forest@ensmp.fr. Some information about the architecture of the Linux PC on which ZeBuLoN is going to be installed is required for generating the license:

* the hostname (result of the UNIX command `hostname`)
* the hostid (result of the UNIX command `hostid`).

A license file 'Zebulon.License' is then to be copied in the directory `$Z7PATH/lib/` to get the license decoder working.
After installation, it should be checked if ZeBuLoN principally works. Tests for the different modules are in `$Z7PATH/TESTS`. Having checked the access rights to the test files or having copied them to a local directory, a quick test can be run as follows:

```
me@pc:$ cd $Z7PATH/TESTS/Static_test/INP
me@pc:$ Zrun aube          (run FE calculation)
me@pc:$ Zmaster aube       (graphics visualization of mesh/results)
```

zMDC is not yet part of the official ZeBuLoN distribution. Further information on the current status can be provided by arjen.roos@onera.fr or benoit.devincre@onera.fr.

D.2 PVM

PVM (Parallel Virtual Machine) is a software package that permits a heterogeneous collection of Unix and/or Windows computers hooked together by a network to be used as a single large parallel computer. Thus large computational problems can be solved more cost effectively by using the aggregate power and memory of many computers. As a side capability, it can be used on one machine as a message passing interface solely, that is to manage the exchange of data between two programs running simultaneously but depending from time to time on the other's results.
In this sense it will be used to pass data between ZeBuLoN and the Fortran program that implements the time integration of the continuum dislocation-based model.

Remark D.2: Actually PVM is not providing the most modern message passing interface, but rather MPI is, so to say, the state of the art. The reason why PVM was chosen by the developers anyway is that the `spawn` command was supposed to be used in order to launch the DD simulation mM, which was not possible with MPI at that time. The latest version of MPI enables this proceeding, but it is said to be somewhat delicate to use. After all, the capabilities of PVM are by far sufficient for the present application.

Amendments to the .bashrc

To get PVM running, the `.bashrc` has to be adjusted as follows.

```
#PVM related variables
export PVM_ROOT=/usr/lib/pvm3
export PVM_ARCH=LINUX
export LD_LIBRARY_PATH=$LD_LIBRARY_PATH:$PVM_ROOT/lib/LINUX:$PVM_ROOT/libfpvm/LINUX
export PVM_DPATH=$PVM_ROOT/lib/pvmd
export PATH=$PATH:/$PVM_ROOT/bin/:$PVM_ROOT/lib/
```

PVM and Fortran 90

To enable working with Fortran90 codes, the header file `/usr/include/fpvm3.h` has to be adjusted. The compiler cannot work when Fortran77 and Fortran90 style is mixed within one[1] file. One possibility is to create a new one called `f90pvm3.h`, where the old comment signs '`C`' are replaced by the modern '!'.
The compile command for a file `hello.f90` using PVM and thus including `f90pvm3.h` then is:

```
gfortran -g -o hello.o hello.f90 -L/usr/lib/ -I/usr/include -lpvm3 -lf90pvm3
```

Remark D.3: The `/usr/include` directory is a standard place for putting header-files. Probably a direct debian installation of the PVM-package will put the header-files right there (and the libraries to `/usr/lib`). There is a simple command that provides the location of a specific file. The location of `fpvm3.h` can be found by typing in a shell:

```
root@pc:$ updatedb
me@pc:$ locate fpvm3.h
```

The first command needs super user / root rights and might take some time to be executed.

PVM and Matlab

Initially, the coupling between ZeBuLoN and the continuum dislocation-based model was supposed to be established based on a MATLAB implementation of the latter. For crucial changes on the code of the continuum dislocation-based model, this would provide the fastest way to check

[1] Note that the parses inserts the content of the header file in the user routine where it is included.

out the interface to ZeBuLoN. As on the ZeBuLoN side, use of PVM is fixed, communication with MATLAB using PVM is required, too. Indeed, a toolbox for MATLAB has been developed by Javier Fernández Baldomer at the University of Granade (Spain) some years ago. However, it does not work with the latest version of MATLAB at the moment.

PVM and ZeBuLoN

In ZeBuLoN, there exists a special wrapper around PVM respectively around an alternative to it, MPI, which unifies the calling sequences. The wrapper `MP_INTERFACE` takes care of the actual calls, so that the programmer only has to program for the wrapper instead of for two different interfaces. The one that is actually running depends on the command line switches used when running a parallel calculation with ZeBuLoN:

```
Zrun -PP -s MPI pvm3,      or
Zrun -PP -s MPI mpi,
```

where in the present case the `-PP` (which stands for Parallel Problem) should be replaced by `-dd` (for dislocation dynamics).

PVM in a nutshell

In this section, a brief collection of the required settings for PVM and some basic commands that are used in the present application is provided. Before running any simulation, the 'virtual machine' has to be defined. PVM is launched by typing `pvm` in a shell. Entering '`add` *machine_name*', PVM is informed that, apart from the machine on which it has just been launched, processes will be run on (at least) one more machine, called *machine_name*. Instead of adding several machines every time PVM is launched, a host file can be written, where all machines are listed, and which is loaded at startup. Information on the current virtual machine is displayed by typing `conf` in the PVM environment. Typing `ps` gives a list of processes running on the virtual machine, `quit` exits from the PVM environment, but leaves PVM running in the background, such that processes can still communicate. In order to really stop PVM, the command `halt` has to be entered. Another useful command is `reset`, that kills all running PVM processes and resets the virtual machine.
For the intended application, only very basic commands are used: Spawning of processes, that is launching a program via PVM; identifying the PVM-processes by their respective IDs; packing, sending, receiving and unpacking information. ZeBuLoN uses a wrapper, such that no matter if PVM or MPI is used for the message passing, the commands are the same. The 'other' partner of the communication, e.g. represented by the implementation in `20gammaplas.f90` within mM, uses the standard Fortran commands for PVM. A collection of the commands is given in table D.2. Details on the arguments and how to call the functions can be found in the PVM books and references, see below.

Z-wrapper	Fortran	Effect
mpi→get_tid	pvmfmytid	get ones own ID
mpi→spawn	pvmfspawn	launch a child process
	pvmfparent	get parent's ID
mpi→initsend	pvmfinitsend	initialize buffer
mpi→pack	pvmfpack	adding numbers/strings to the current buffer
mpi→send	pvmfsend	send the buffer
mpi→recv	pvmfrecv	receive a buffer
mpi→unpack	pvmfunpack	get content out of the received buffer

Table D.2: Short review of the PVM commands used in the present application, both in the language of the ZeBuLoN wrapper and as used in Fortran code.

A log-file/protocol of the PVM session is maintained in `/tmp/pvml.<uid>`. This is also where the standard output of child processes is directed to. The command `tail -f /tmp/pvml.<uid>` allows for tracking the content of this file. It works like `less` but remains uptodate as the file is changing.

Acquisition and useful links

PVM at netlib.org : http://www.netlib.org/pvm3/
official website of PVM: http://www.epm.ornl.gov/pvm/
online book: http://www.netlib.org/pvm3/book/
PVM toolbox for MATLAB and Octave: http://atc.ugr.es/javier-bin/pvmtb_eng

D.3 Fortran

The name ForTran is derived from 'Formula Translator', which points out to the original intention that led to its development: the input of scientific formulas to a machine was supposed to be crucially simplified. This goal was perfectly reached. Fortran is the mother of all algorithmically based scientific programming languages. In the last decades, Fortran has been continuously improved and standardised. The elements of the language were continuously advanced, where backward compatibility was guaranteed all over the years. Thus Fortran90/95 is nowadays a very modern and structured language, which however still enables one to (re)use the code implemented in the old-fashioned Fortran77 style.
Thus, a lot of veritable code exists, especially for elaborate numerical procedures, see for example netlib.org. Another advantage for numerical issues is Fortran's mathematical structure, enabling for example a quite intuitive handling of (multidimensional) arrays. In this sense, it is somewhat close to the thinking in MATLAB. This was a crucial point militating in favour of Fortran90 as programming language for the implementation of the continuum dislocation-based model.
A collection of free books and tutorials on Fortran is given below.

Precompilation of fixed subroutines

Most Fortran utils come as source code in either F77 (ending on .f or .for) or F90 (ending on .f90). Usually a modern compiler can deal with both kinds of code. To use the subroutines defined in such utils, like for example the integrators implied in odepack or the gnufor-util, one possibility is to compile all the files which include subroutines that are used at once, e.g. for the ode-solvers

```
gfortran -o main.o main.f90 opkdmain.f opkda1.f opkda2.f
```

But in the case of very extended utils, or such which cause the compiler to print out a lot of warnings due to their old-fashioned style, compilation takes quite long - every time changes are made in the main code.
Therefore it is favourable to 'pre-compile' the object code of the utils, the source of which usually is not going to be changed anyway, and just use the resulting object-file when compiling the main code. As a subroutine in general cannot be compiled stand-alone, the compiler has to be called with the option `-shared`.

```
gfortran -shared -o opkd.o opkdmain.f opkda1.f opkda2.f
```

The object file `opkd.o` in the example now contains the binaries for all three source files that have been compiled. With the object file situated in the working directory, that is where the main file is situated, and in the standard library directory `/lib`, it can be used from now on using the compilation command

```
gfortran -o main.o main.f90 opkd.o
```

Remark D.4: The user may find a different, maybe more elegant way, to use shared library objects.

Another point were shared compilation is necessary is for modules defined in separate files. A file `parameters.f90` containing the `module parameters` is compiled first by

```
gfortran -shared -o parameters.o parameters.f90
```

Henceforth it can be used in the compilation of the main program

```
gfortran -o main.o main.f90 parameters.f90,
```

where `main.f90` contains the line `use parameters`.

Acquisition and useful links

A Fortran compiler comes along with the Linux installation automatically. Here `gfortran` was used, which is part of the gcc-package. It is also possible to get the intel fortran compiler for free - probably also for Windows.

online book on Fotran90/95:	http://www.rz.uni-bayreuth.de/lehre/fortran90/vorlesung/
odepack at netlib.org:	http://www.netlib.org/ode/
bivariate interpol. at netlib.org:	http://www.netlib.org/toms/526
a short tutorial:	http://www.cisl.ucar.edu/tcg/consweb/Fortran90/F90Tutorial/

Bibliography

[1] H. Lippmann. *Mechanik des plastischen Fließens*. Springer, 1981.

[2] F. Dunne and N. Petrinic. *Introduction to Computational Plasticity*. Oxford University Press, 1st edition, 2005.

[3] D. Helm. *Formgedächtnislegierungen*. PhD thesis, Universität Gesamthochschule Kassel, 2001.

[4] J.C. Simo and T.J.R. Hughes. *Computational Inelasticity*. Springer Verlag, New York, 1998.

[5] G. Cailletaud. A micromechanical approach to inelastic behaviour of metals. *International Journal of Plasticity*, 8:55–73, 1992.

[6] R.J. Asaro. Geometrical effects in the inhomogeneous deformation of ductile single crystals. *Acta Metallurgica*, 27:445–453, 1979.

[7] R.J. Asaro. Crystal plasticity. *Journal of Applied Mechanics*, 50:921–934, 1983.

[8] R. Sedláček. *Curved dislocations in continuum crystal plasticity*. Professorial dissertation. TU München, October 2004.

[9] E. Arzt. Size effects in materials due to microstructural and dimensional constraints: a comparative review. *Acta Materialia*, 46:5611–5626, 1998.

[10] Y. Huang, X. Feng, G.M. Pharr, and K.C. Hwang. A nano-indentation model for spherical indenters. *Modelling Simul. Mater. Sci. Eng.*, 15:S255 – S262, 2007. doi:10.1088/0965-0393/15/1/S19.

[11] A. Needleman and J.G. Sevillano. Preface to the viewpoint set on: geometrically necessary deslocations and size dependent plasticity. *Scripta Materialia*, 48:109–111, 2003.

[12] H. Gao and Y. Huang. Geometrically necessary dislocation and size-dependent plasticity. *Scripta Materialia*, 48:113–118, 2003.

[13] W. D. Nix and H. Gao. Indentation size effects in crystalline materials: A law for strain gradient plasticity. *J. Mech. Phys. Solids*, 46:411–425, 1998.

[14] J.R. Greer and W.D. Nix. Size dependence of mechanical properties of gold at the submicron scale. *Applied Physics A*, 80:1625–1629, 2005.

[15] D. Weygand. Size effect in the plastic response of sub-micrometer sized pillars: a three dimensional discrete dislocation dynamics study. In P. Gumbsch, editor, *Proc. 3rd Int. Conf. Multiscale Materials Modeling*, pages 244–247, Freiburg, September 2006.

[16] M.D. Uchic, D.M. Dimiduk, J.N. Florando, and W.D. Nix. Sample dimensions influence strength and crystal plasticity. *Science*, 305:986–989, 2004.

[17] E. van der Giessen and A. Needleman. Discrete dislocation plasticity: a simple planar model. *Modelling and Simulation in Materials Science and Engineering*, 3:689–735, 1995.

[18] J.L. Bassani, A. Needleman, and E. van der Giessen. Plastic flow in a composite: a comparison of nonlocal continuum and discrete dislocation predictions. *International Journal of Solids and Structures*, 38:833–853, 2001.

[19] S. Yefimov, I. Groma, and E. van der Giessen. A comparison of a statistical-mechanics based plasticity model with discrete dislocation plasticity calculations. *Journal of the Mechanics and Physics of Solids*, 52:279–300, 2004.

[20] V. S. Deshpande, A. Needleman, and E. van der Giessen. Discrete dislocation plasticity modeling of short cracks in single crystals. *Acta Materialia*, 51:1–15.

[21] B. v. Blanckenhagen, E. Arzt, and P. Gumbsch. Discrete dislocation simulation of plastic deformation in metal thin films. *Acta Materialia*, 52:773–784, 2004.

[22] L. Nicola, E. van der Giessen, and A. Needleman. Discrete dislocation analysis of size effects in thin films. *Journal of Applied Physics,* 93:5920–5928, 2003.

[23] J.Y. Shu, N.A. Fleck, E. van der Giessen, and A. Needleman. Boundary layers in constrained plastic flow: comparison of nonlocal and discrete dislocation plasticity. *Journal of the Mechanics and Physics of Solids,* 49:1361–1395, 2001.

[24] S. Yefimov, E. van der Giessen, and I. Groma. Bending of a single crystal: discrete dslocation and nonlocal crystal plasticity simulations. *Modelling and Simulation in Materials Science and Engineering*, 12:1069–1086, 2004.

[25] A. Widjaja, E. van der Giessen, and A. Needleman. Discrete dislocation modelling of submicron indentation. *Materials Science and Engineering A*, 400-401:456–459, 2005.

[26] L.P. Kubin, Y. Estrin, and G. Canova. In D. Walgraef and N.M. Ghoniem, editors, *Defects and materials instabilities*, NATO ASI series, page 277. Kluwer, Dordrecht, Netherlands, 1990.

[27] B. Devincre. Meso-scale simulation of the dislocation dynamics. In H.O. Kirchner, L.P. Kubin, and V. Pontikis, editors, *Computer Simulation in Materials Science: Nano/Meso/Macroscopic Space & Time Scales*. NATO ASI Series, North Holland, 1996.

[28] S. Groh, B. Devincre, L.P. Kubin, A. Roos, F. Feyel, and J.L. Chaboche. Size effects in metal matrix composites. *Materials Science and Engineering A*, 400-401:279–282, 2005.

[29] S. Groh, B. Devincre, L. Kubin, A. Roos, F. Feyel, and J.L. Chaboche. Dislocations and elastic anisotropy in heteroepitaxial metallic thin films. *Philosophical Magazine Letters*, 83(5):303–313, 2003.

[30] S. Groh, B. Devincre, F. Feyel, L.P. Kubin, A. Roos, and J.L. Chaboche. Discrete-continuum modelling of metal matrix composites plasticity. In Y. Shibutani and H. Kitagawa, editors, *IUTAM Symposium on Mesoscopic Dynamics in Fracture Process and Strength of Materials (Osaka)*, pages 235–244. Kluwer Academic Publishers, 2004.

[31] C. Lemarchand, B. Devincre, and L.P. Kubin. Homogenization method for a discrete-continuum simulation of dislocation dynamics. *Journal of the Mechanics and Physics of Solids*, 49:1969–1982, 2001.

[32] V. Bulatov, W. Cai, J. Fier, M. Hiratani, G. Hommes, T. Pierce, M. Tang, M. Rhee, K. Yates, and T. Arsenlis. Scalable line dynamics in ParaDiS. In *SC '04: Proceedings of the 2004 ACM/IEEE conference on Supercomputing*, page 19, Washington, DC, USA, 2004. IEEE Computer Society.

[33] L.E. Shilkrot, W.A. Curtin, and R.E. Miller. A coupled atomistic/continuum model of defects in solids. *Journal of the Mechanics and Physics of Solids*, 50:2085–2106, 2002.

[34] L.E. Shilkrot, R.E. Miller, and W.A. Curtin. Multiscale plasticity modeling: coupled atomistics and discrete dislocation mechanics. *Journal of the Mechanics and Physics of Solids*, 52:755–787, 2004.

[35] E. Kröner, editor. *Mechanics of generalized continua*. Springer Verlag, Berlin/Heidelberg/New York, 1968.

[36] C. Sansour. *Ein einheitliches Konzept verallgemeinerter Kontinua mit Mikrostruktur unter besonderer Berücksichtigung der finiten Viskoplastizität*. Number 2/99 in Publikationsreihe des Fachgebiets Maschinenelemente und Maschinenakustik der TU Darmstadt. Shaker Verlag, Aachen, 1999.

[37] A.C. Eringen and E.S. Suhubi. Nonlinear theory of simple micro-elastic solids - I. *International Journal of Engineering Science*, 2:189–203, 1964.

[38] R.D. Mindlin. Microstructure in linear elasticity. *Archive for Rational Mechanics and Analysis*, 16:51–78, 1964.

[39] E. Cosserat and F. Cosserat. *Théorie des corps déformables*. Libraire scientifique A. Hermann et fils, Paris, 1909.

[40] S. Forest. Cosserat media. In K.H.J. Buschow, R.W. Cahn, M.C. Flemings, B. Ilschner, E.J. Kramer, and S. Mahajan, editors, *Encyclopedia of Materials : Science and Technology*. Elsevier, 2001.

[41] S. Forest and R. Sedláček. Plastic slip distribution in two–phase laminate microstructures: Dislocation–based vs. generalized–continuum approaches. *Philosophical Magazine*, 83:245–276, 2003.

[42] R. Sedláček and S. Forest. Non-local plasticity at microscale: A dislocation-based and a cosserat model. *physica status solidi (b)*, 221:583–596, 2000.

[43] S. Forest, F. Barbe, and G. Cailletaud. Cosserat modelling of size effects in the mechanical behaviour of polycrystals and multi-phase materials. *International Journal of Solids and Structures*, 37:7105–7126, 2000.

[44] N. Smajlovič. *Das Cosserat-Kontinuum als Werkstoffmodell bei der Torsion anisotroper dünnwandiger Rohre*. Number 480 in Fortschrittberichte VDI 5: Grund- und Werkstoffe. VDI Verlag GmbH, Düsseldorf, 1997.

[45] S. Forest. Generalized continuum modelling of single and polycrystal plasticity. In D. Raabe, F. Roters, F. Barlat, and L.Q. Chen, editors, *Continuum Scale Simulation of Engineering Materials*, chapter 25, pages 513–526. Wiley-VCH, 2004.

[46] J.F. Nye. Some geometrical relations in dislocated crystals. *Acta Metallurgica*, 1:153–162, 1953.

[47] E.C. Aifantis. On the microstructural origin of certain inelastic models. *Trans. of ASME, Journal of Engineering Materials and Technology*, 106:326, 1984.

[48] E.C. Aifantis. The pyhsics of plastic deformation. *International Journal of Plasticity*, 3:211–247, 1987.

[49] E.C. Aifantis. Gradient deformation models at nano, micro, and macro scales. *Journal of Engineering Materials and Technology*, 121:189–202, 1999.

[50] N.A. Fleck, G.M. Muller, M.F. Ashby, and J.W. Hutchinson. Strain gradient plasticity: theory and experiment. *Acta Metallurgica et Materialia*, 42:475–487, 1994.

[51] W.T. Koiter. Couple-stresses in the theory of elasticity. *Proc. Koninkl. Ned. Akad. von Wetenschappen*, 67:17–44, 1964.

[52] B.N. Legarth. Strain-gradient effects in anisotropic materials. *Modelling Simul. Mater. Sci. Eng.*, 15:S71 – S81, 2007. doi:10.1088/0965-0393/15/1/S07.

[53] P. Fredriksson and P. Gudmundson. Competition between interface and bulk dominated plastic deformation in strain gradient plasticity. *Modelling Simul. Mater. Sci. Eng.*, 15:S61 – S69, 2007. doi:10.1088/0965-0393/15/1/S06.

[54] R.H.J. Peerlings. On the role of moving elastic - plastic boundaries in strain gradient plasticity. *Modelling Simul. Mater. Sci. Eng.*, 15:S109 – S120, 2007. doi:10.1088/0965-0393/15/1/S10.

[55] A. Acharya. A model of crystal plasticity based on the theory of continuously distributed dislocations. *Journal of the Mechanics and Physics of Solids*, 49:761–784, 2001.

[56] A. Acharya. Driving forces and boundary conditions in continuum dislocation mechanics. *Proc. R. Soc. Lond. A*, 459:1343–1363, 2003.

[57] A. Acharya. Constitutive analysis of finite deformation field dislocation mechanics. *Journal of the Mechanics and Physics of Solids*, 52:301–316, 2004.

[58] A. Roy and A. Acharya. Finite element approximations of field dislocation mechanics. *Journal of the Mechanics and Physics of Solids*, 53:143–170, 2005.

[59] E. Kröner. Initial studies of a plasticity theory based upon statistical mechanics. In R. Balian, M. Kléman, and J.P. Poirier, editors, *Inelastic behavior of solids*, pages 137–148. McGraw-Hill, 1969.

[60] F.F. Csikor and I. Groma. Probability distribution of internal stress in relaxed dislocations systems. *Physical Review B*, 70:064106, 2004.

[61] I. Groma. Link between the microscopic and mesoscopic length-scale description of the collective behavior of dislocations. *Physical Review B*, 56:5807–5813, 1997.

[62] I. Groma, F.F. Csikor, and M. Zaiser. Spatial correlations and higher-order gradient terms in a continuum description of dislocation dynamics. *Acta Materialia*, 51:1271–1281, 2003.

[63] I. Groma and G. Vörös. Origin of gradient terms in plasticity at different length scales. *Scripta Materialia*, 48:161–165, 2003.

[64] J. Kratochvíl, M. Kružík, and R. Sedláček. Statistically based continuum model of misoriented dislocation cell structure formation. *Physical Review B*, 75:064104, 2007.

[65] T. Hochrainer, M. Zaiser, and P. Gumbsch. A three-dimensional continuum theory of dislocation systems: Kinematics and mean-field formulation. *Philosophical Magazine*, 87(8-9):1261–1282, 2006.

[66] A. El-Azab. Statistical mechanics treatment of the evolution of dislocation distributions in single crystals. *Physical Review B*, 61:11956–11966, 2000.

[67] A.M. Kosevich. Crystal dislocations and the theory of elasticity. In F.R.N. Nabarro, editor, *Dislocations in Solids vol. 1. The Elastic Theory*, pages 33–141. North-Holland, Amsterdam, 1979.

[68] T. Hochrainer. *Evolving systems of curved dislocations: Mathematical foundations of a statistical theory*. PhD thesis, Universität Karlsruhe, 2007.

[69] M. Zaiser and T. Hochrainer. Some steps towards a continuum representation of 3D dislocation systems. *Scripta Materialia*, 54:717–721, 2006.

[70] R. Sedláček, J. Kratochvíl, and E. Werner. The importance of being curved: Bowing dislocations in continuum description. *Philosophical Magazine*, 83:3735–3752, 2003.

[71] J. Kratochvíl and M. Saxlová. Sweeping mechanism of dislocation pattern formation. *Scripta Metallurgica et Materialia*, 26:113, 1992.

[72] T. Hochrainer. *Journal of Geometry and Physics*. submitted.

[73] M. Zaiser, N. Nikitas, T. Hochrainer, and E. Aifantis. Modeling size effects using 3D density-based dislocation dynamics. *Philosophical Magazine*, 87(8-9):1283–1306, 2006.

[74] T. Hochrainer and M. Zaiser. Fundamentals of a continuum theory of dislocations. PoS(SMPRI2005), Int. conf. on statistical mechanics of plasticity and related instabilities, Bangalore, India, 2005.

[75] M.P. do Carmo. *Differential Geometry of Curves and Surfaces*. Prentice Hall, 1976.

[76] R. Sedláček and E. Werner. Constrained shearing of a thin crystalline strip. *Physical Review B*, 69:134114, 2004.

[77] D. Hull and D.J. Bacon. *Introduction to Dislocations*. Pergamon, 3rd edition, 1984.

[78] M. Peach and J.S. Koehler. The forces exerted on dislocations and the stress fields produced by them. *Physical Review*, 80:436–437, 1950.

[79] A. Granato and K. Lücke. *Journal of Applied Physics*, 27:789, 1956.

[80] N.M. Ghoniem, S.-H. Tong, and L.Z. Sun. Parametric dislocation dynamics: A thermodynamics-based approach to investigations of mesoscopic plastic deformation. *Physical Review B*, 61:913–927, 2000.

[81] R. Sedláček. Orowan-type size effect in plastic bending of free-standing thin crystalline strip. *Materials Science and Engineering A*, 393:387–395, 2005.

[82] R. Sedláček. Bending of thin crystalline strips: Comparison of continuum dislocation-based models. *Materials Science and Engineering A*, 400-401:439–442, 2005.

[83] E. Kröner. *Kontinuumstheorie der Versetzungen und Eigenspannungen*. Springer, Berlin, 1958.

[84] E. Kröner. Continuum theory of defects. In R. Balian, M. Kléman, and J.P. Poirier, editors, *Physics of defects*, pages 219–312. North-Holland publishing company, Amsterdam - New York - Oxford, august 1980.

[85] K. Königsberger. *Analysis 2*. Springer, 2 edition, 1997.

[86] J.P. Hirth and J. Lothe. *Theory of Dislocations*. Krieger Publishing Company, Malabar, Florida, 2nd edition, 1992.

[87] A. Cottrell. *The mechanical properties of matter*. Wiley, New York, 1964.

[88] M.F. Ashby. The deformation of plastically non-homogeneous materials. *Philosophical Magazine*, 21:399–424, 1970.

[89] T. Mura. Continuous distribution of moving dislocations. *Philosophical Magazine*, 8:843–857, 1963.

[90] T. Mura. On dynamic problems of continuous distribution of moving dislocations. *International Journal of Engineering Science*, 1:371–381, 1963.

[91] T. Mura. Periodic distribution of dislocations. In *Proceedings of the Royal Society of London A*, pages 528–544, 1964.

[92] T. Mura. *Micromechanics of defects in solids*. Martinus Nijho. Dordrecht, 1982.

[93] L.P. Kubin and A. Mortensen. Geometrically necessary dislocation and strain-gradient plasticity: a few critical issues. *Scripta Materialia*, 48:119–125, 2003.

[94] C. Schwarz, R. Sedláček, and E. Werner. Application of a continuum dislocation-based model to a tensile test on a thin film. *Materials Science and Engineering A*, 400-401:443–447, 2005.

[95] A. El-Azab. The boundary value problem of dislocation dynamics. *Modelling and Simulation in Materials Science and Engineering*, 8:37–54, 2000.

[96] R. Sedláček, C. Schwarz, J. Kratochvíl, and E. Werner. Continuum theory of evolving dislocation fields. *Philosophical Magazine*, 87:1225–1260, 2007.

[97] C. Schwarz, R. Sedláček, and E. Werner. Towards a 2D Finite Element implementation of a continuum-dislocation based model. *Computational Materials Science*, 39:85–90, 2007.

[98] O.C. Zienkiewicz. *Methode der Finiten Elemente*. Carl Hanser Verlag, 2 edition, 1984. Studienausgabe.

[99] P. Knabner and L. Angermann. *Numerik partieller Differentialgleichungen*. Springer, 2000.

[100] T. Rung, L. Xue, J. Yan, M. Schatz, and F. Thiele. *Numerische Methoden der Thermo- und Fluiddynamik*. Hermann-Föttinger-Institut für Strömungsmechanik, TU Berlin, 2002.

[101] H.C. Kuhlmann. *Numerische Methoden der Strömungsmechanik*. Lecture notes. TU Wien, 2004.

[102] A. Arsenlis, D.M. Parks, R. Becker, and V.V. Bulatov. On the evolution of crystallographic dislocation density in non-homogeneously deforming crystals. *Journal of the Mechanics and Physics of Solids*, 52:1213–1246, 2004.

[103] T.J.R. Hughes and A.N. Brooks. A multidimensional upwind scheme with no crosswind diffusion. *Finite element methods for convection dominated flows*, 34:19–35, 1979.

[104] A.N. Brooks and T.J.R. Hughes. Stream-line Upwind/Petrov-Galerkin formulation for convection dominated flows with particular emphasis on the incompresible Navier-Stokes equations. *Comp. Meth. Appl. Mech. Engrg.*, 32:199–259, 1982.

[105] T.J.R. Hughes, L.P. Franca, and G.M. Hulbert. A new finite element formulation for computational fluid dynamcs: VIII. the Galerkin/Least-Squares method for advective-diffusive equations. *Comp. Meth. Appl. Mech. Engrg.*, 73(2):173–189, 1989.

[106] A. Roy and A. Acharya. Finite element approximations of field dislocation mechanics. *Journal of the Mechanics and Physics of Solids*, 53:143–170, 2005.

[107] R.J. LeVeque. *Finite Volume Methods for hyperbolic Problems*. Cambridge University Press, 2003.

[108] S. Limkumnerd and J.P. Sethna. Mesoscale theory of grains and cells: crystal plasticity and coarsening. *Physical Review Letters*, 96:095503, 2006.

[109] Y. Xiang, L.T. Cheng, D.J. Srolovitz, and E. Weinan. A level set method for dislocation dynamics. *Acta Materialia*, 51:5499 – 5518, 2003.

[110] J.A. Sethian. *Level Set Methods and Fast Marching Methods: Evolving interfaces in computational geometry, fluid mechanics, computer vision and materials science*. Cambridge Monographs on Applied and Computational Mathematics. Cambridge University Press, 1999.

[111] D. van Tran, D.T.S. Nguyen, and M. Tsuji. *The Characteristic Method and Its Generalizations for First-Order Nonlinear Partial Differential Equations*. CRC Monographs and Surveys in Pure and Applied Mathematics. CRC Press, 1999.

[112] M. Seaïd. Time integration schemes in Eulerian-Lagrangian computations for advection-diffusion reaction problems. Technical Report 3122, TU Darmstadt, 2004.

[113] A. Smolianski, O. Shipilova, and H. Haario. A fast high-resolution algorithm for linear convection problems: Particle transport method. Technical Report 98, Laboratory of Applied Mathematics, Lappeenranta University of Technology, 2005.

[114] M.R. Kaazempur-Mofrad and C.R. Ethier. An efficient characteristic Galerkin scheme for the advection equation in 3-D. *Comp. Meth. Appl. Mech. Engrg.*, 191:5345–5363, 2002.

[115] A. Iske and M. Käser. Conservative Semi-Lagrangian advection on adaptive unstructured meshes. *Numerical Methods for Partial Differential Equations*, 20:388–411, 2004.

[116] J. Behrens and A. Iske. Grid-free adaptive Semi-Lagrangian advection using radial basis functions. *Computers and Mathematics with Applications*, 43:319–327, 2002.

[117] P. Hansbo. A Free-Lagrange Finite Element method using space-time elements. *Comp. Meth. Appl. Mech. Engrg.*, 188:347–361, 2000.

[118] C. Schwarz, R. Sedláček, and E. Werner. Plastic deformation of a composite and the source-shortening effect simulated by the continuum dislocation-based model. *Modelling Simul. Mater. Sci. Eng.*, 15:S37 – S49, 2007. doi:10.1088/0965-0393/15/1/S04.

[119] W.D. Nix. Mechanical properties of thin films. *Metallurgical Transactions A*, 20A:2217–2245, 1989.

[120] H. J. Böhm. A short introduction to basic aspects of continuum micromechanics. In *Frontiers for computational micromechanics in industrial and engineering materials: ambient and high temperature deformation and fracture*, European advanced summer school, Galway, Ireland, 1998. National University of Ireland. Lecture notes.

[121] M. Nygårds and P. Gudmunson. Three-dimensional periodic Voronoi grain models and micromechanical FE-simulations of a two-phase steel. *Computational Materials Science*, 24:513–519, 2002.

[122] K.-J. Bathe. *Finite Elemente Methoden*. Springer-Verlag, 1990.

[123] C. Lemarchand. *De la dynamique des dislocations à la mécanique des milieux continus: developpement et application d'und simulation micro-macro*. PhD thesis, L'Université Paris VI, 1999.

[124] S. Groh. *Simulation de la plasticité des matériaux cristallins par le modèle discret-continu*. PhD thesis, L'Université Paris 11, Orsay, 2003.

[125] J. Kratochvíl and R. Sedláček. Mechanisms controlling the size of misoriented dislocation cells. In N. M. Ghoniem, editor, *Proceedings of Second International Conference on Multiscale Materials Modeling*, pages 221–223. University of California Los Angeles, October 2004.

[126] J. Křišt'an and J. Kratochvíl. Interactions of glide dislocations in a channel of a persistent slip-band. *Philosophical Magazine*. submitted.

[127] R. Sedláček, C. Schwarz, and E. Werner. Modeling of size-dependent internal stresses in dislocation cell structures. *Materials Science and Engineering A*, 2007. Accepted for publication, available online.

[128] H.H.M. Cleveringa, E. van der Giessen, and A. Needleman. Comparison of discrete dislocation and continuum plasticity predictions for a composite material. *Acta Materialia*, 45:3163–3179, 1997.

[129] L.M. Brown and D.R. Clarke. The work hardening of fibrous composites with particular reference to the copper-tungsten system. *Acta Metallurgica*, 25:563–570, 1977.

[130] W. Prantl, T. Stadlober, and E. Werner. Elektronenmikroskopische Gefügeuntersuchung an einem faserverstärkten Aluminiumverbundwerkstoff. *Zeitschrift für Metallkunde*, 86:839–844, 1995.

[131] E. Werner, H.J. Böhm, W. Prantl, and F.G. Rammerstorfer. Plasticity and damage of a fiber reinforced aluminum alloy: experiments and macromechanical modeling. *ZAMM*, 78:S77–S80, 1998.

[132] H. Mughrabi. Dislocation wall and cell structures and long-range internal stresses in deformed metal crystals. *Acta Metallurgica*, 31:1367–1379, 1983.

[133] gnu.org. http://www.gnu.org/software/bash/manual/bashref.html, 2003.

Disclaimer

As the author considered it helpful for the reader, several hyperlinks have been included in this thesis.
The author is not responsible for any contents linked or referred to in this work - unless he has full knowledge of illegal contents and would be able to prevent the visitors of his site from viewing those pages. If any damage occurs by the use of information presented there, only the author of the respective pages might be liable, not the one who has linked to these pages.

Index